Project No. 14-6557

Extraction of Uranium from Seawater: Design and Testing of a Symbiotic System

Fuel Cycle Research and Development

Alex Slocum
Massachusetts Institute of Technology

Stephen Kung, Federal POC
Phil Britt, Technical POC

NEUP Nuclear Energy University Programs
U.S. Department of Energy

AWARD NUMBER: DE-NE0008268

Extraction of Uranium from Seawater: Design and Testing of a Symbiotic System

Project Final Report

Principal Investigator: Prof. Alexander H. Slocum
slocum@mit.edu | 617.253.0012

Submitted by: Dr. Maha N. Haji, Postdoctoral Associate
mhaji@mit.edu | 617.253.2052

Recipient Organization: Massachusetts Institute of Technology
77 Massachusetts Avenue,
Cambridge, MA 02139

Grant Period: 10/01/2014 - 11/30/2017

Prepared for the
U.S. Department of Energy
Fuel Cycle Research & Development

Report Date: 11/30/2017

Signature of Submitting Official: _____

Contents

1 Summary **6**

2 Publications and Presentations To Date **8**
2.1 Journal Publications 8
2.2 Conference Publications 9
2.3 Patents 10
2.4 Presentations 10

3 Introduction **13**

4 Background Research **14**

5 Mechanical Investigation of Sorption Optimization (MISO) **19**
5.1 Recovery Rate 19
5.2 Adsorbent Degradation 20
5.3 Mechanical Parameters 21
5.4 Sorption Optimization 22

6 Seawater Uranium Suitability of Harvesting Index (SUSHI) **24**
6.1 Motivation 24
6.2 Incorporated factors 24
6.2.1 Wind Power 24
6.2.2 Adsorbent capacity 26
6.3 Suitability Index 28
6.4 Datasets 29
6.4.1 Ocean surface winds 29
6.4.2 Sea surface temperature 29
6.5 GUI Presentation 30
6.5.1 Data output 34
6.5.2 Reminders: DOs and DONTs 35
6.5.3 An example 36
6.6 Future Work 37

7 Adsorbent Shell Enclosures **39**
7.1 Motivation . . . 39
7.2 Theory . . . 39
7.3 Adsorbent Interior . . . 40
7.4 Shell Enclosure . . . 43

8 1/50th Scale Prototype **47**
8.1 Functional Requirements . . . 47
8.2 System Design Analysis . . . 47
8.2.1 Circumference Looping System . . . 48
8.2.2 Under-Platform Looping System . . . 49
8.3 Prototype Development . . . 50
8.3.1 Design Process . . . 50
8.3.2 Testing . . . 53
8.4 Cost analysis . . . 53
8.4.1 Reference Deployment Case . . . 53
8.4.2 WUSABI-Koosh Deployment . . . 56
8.4.3 Comparison of Deployment Schemes . . . 58
8.5 Design Iteration . . . 59
8.6 Conclusions . . . 61

9 Flume Testing of Shell Enclosures **63**
9.1 Method . . . 63
9.1.1 Shell Enclosure Design and Fabrication . . . 63
9.1.2 Design Analysis . . . 66
9.1.3 Adsorbent preparation, sampling, and analysis . . . 68
9.2 Results . . . 69
9.3 Discussion . . . 72

10 Symbiotic Machine for Ocean uRanium Extraction (SMORE) Design **74**
10.1 Functional Requirements . . . 74
10.2 Elution and Regeneration . . . 75
10.3 Mooring and Recovery . . . 75
10.4 Mechanical Design . . . 75
10.4.1 Ball-Chain Net . . . 76
10.4.2 Roller Design . . . 78
10.4.3 Platform Length . . . 79
10.5 Elution and Regeneration . . . 79
10.6 Roller and Wheel Subassembly . . . 80
10.7 Power Requirement . . . 81
10.7.1 Friction Between Wheels and Rail . . . 81
10.7.2 Ball-Chain Tension . . . 82
10.7.3 Elution and Regeneration Processes . . . 84
10.7.4 Chemical Pumping Power . . . 84

10.8 Design Analysis 85

11 SMORE 1/10th Physical Scale Prototype Ocean Test 87
11.1 1/10th Physical Scale Prototypes 87
11.1.1 System 1: Stationary net system 87
11.1.2 System 2: Continuous net system 90
11.2 Ocean Test Site 90
11.3 Shell Enclosure Net 91
11.4 Adsorbent Deployment and Sampling 93
11.5 Ocean Test Measurements 94
11.6 Results 97
11.6.1 Continuous System Modifications 97
11.6.2 Sensor Data 98
11.6.3 Biofouling 100
11.6.4 Water Flow Rate 101
11.6.5 Uranium Uptake 104
11.7 Discussion 107

12 SMORE Hydrodynamic Response 110
12.1 Theory 110
12.2 Experimental Setup 112
12.2.1 Model scaling 112
12.2.2 Models for testing 113
12.2.3 Experimental facilities 115
12.2.4 Excitation Forces 115
12.2.5 Response Amplitude Operators 116
12.3 Results 119
12.3.1 Excitation Forces 119
12.3.2 Response Amplitude Operators 121
12.4 Discussion 123

13 SMORE Cost-Analysis 125
13.1 Discounted Cash Flow Methodology 125
13.2 Cost Components 127
13.2.1 Adsorbent Production Cost 127
13.2.2 Mooring and Deployment Cost 128
13.2.3 Elution and Regeneration Cost 129
13.3 Parameter Space 130
13.3.1 Length of campaign 130
13.3.2 Temperature 130
13.3.3 Degree of grafting 130
13.3.4 Number of reuses 131
13.3.5 Degradation 131
13.3.6 Biofouling 132
13.4 Reference Deployment Strategy 132

13.5 SMORE Deployment Strategy 133
13.6 Results 135
13.7 Conclusion 137

14 Acknowledgements **140**

10 Bibliography **141**

Summary

The U.S. Department of Energy in October 2014 awarded the Massachusetts Institute of Technology (MIT) a Nuclear Energy University Program grant (DE-NE0008268) to investigate the design and testing of a symbiotic system to harvest uranium from seawater. As defined in the proposal, the goals for the project are:

1. Address the design of machines for seawater uranium mining.
2. Develop design rules for a uranium harvesting system that would be integrated into an offshore wind power tower.
3. Fabricate a 1/50th size scale prototype for bench and pool-testing to verify initial analysis and theory.
4. Design, build, and test a second 1/10th size scale prototype in the ocean for more comprehensive testing and validation.

This report describes work done as part of DE-NE0008268 from 10/01/2014 to 11/30/2017 entitled, "Extraction of Uranium from Seawater: Design and Testing of a Symbiotic System." This effort is part of the Seawater Uranium Recovery Program.

This report details the publications and presentations to date on the project, an introduction to the project's goals and background research into previous work done to achieve these goals thusfar. From there, the report describes an algorithm developed during the project used to optimize the adsorption of uranium by changing mechanical parameters such as immersion time and adsorbent reuses is described. Next, a design tool developed as part of the project to determine the global feasibility of symbiotic uranium harvesting systems. Additionally, the report details work done on shell enclosures for uranium adsorption. Moving on, the results from the design, building, and testing of a 1/50th physical scale prototype of a highly feasible symbiotic uranium harvester is described. Then, the report describes the results from flume experiment used to determine the affect of enclosure shells on the uptake of uranium by the adsorbent they enclose. From there the report details the design of a Symbiotic Machine for Ocean uRanium Extraction (SMORE). Next, the results of the 1/10th scale physical scale prototype of a highly feasible symbiotic uranium harvester are presented. The report then details the design and results of an experiment to examine the hydrodynamic effects of a uranium harvester on the offshore wind turbine it is attached to using a 1/150th Froude scale tow tank test. Finally, the report details the

results of an initial cost-analysis for the production of uranium from seawater from such a symbiotic device.

Publications and Presentations To Date

2.1 Journal Publications

1. M. E. Flicker Byers, M. N. Haji, A. H. Slocum, and E. Schneider, "Cost Analysis and Optimization of the Symbiotic Machine for Ocean Uranium Extraction using Shell Enclosures" (in prep. for *Ocean Engineering*).

2. M. N. Haji, J. Drysdale, K. Buesseler, and A. H. Slocum, "Results of Ocean Trial of a Symbiotic Device to Harvest Uranium from Seawater through the Use of Shell Enclosures," (in prep. for *Ocean Engineering*).

3. M. N. Haji, J. Gonzalez, J. Drysdale, K. Buesseler, and A. H. Slocum, "The effects of protective shell enclosures on uranium adsorbing polymers" (in prep. for *Industrial & Engineering Chemistry Research*).

4. M. N. Haji, J. M. Kluger, T. P. Sapsis, and A. H. Slocum, "A Symbiotic Approach to the Design of Offshore Wind Turbines with Other Energy Harvesting Systems" (submitted to *Ocean Engineering*).

5. M. N. Haji, J. M. Kluger, J. W. Carrus, T. P. Sapsis, and A. H. Slocum, "Experimental Investigation of Hydrodynamic Response of an Ocean Uranium Extraction Machine attached to a Floating Wind Turbine" (accepted to *International Journal of Offshore and Polar Engineering*).

6. M. E. Flicker Byers, M. N. Haji, A. H. Slocum, and E. Schneider, "Cost Optimization of a Symbiotic System to Harvest Uranium from Seawater via an Offshore Wind Turbine" (in revision for *Ocean Engineering*).

7. A. H. Slocum, M. N. Haji, A. Z. Trimble, M. Ferrera, and S. J. Ghaemsaidi, "Integrated Pumped Hydro Reverse Osmosis Systems," *Sustainable Energy Technologies and Assessments*, 18, 80-99, 2016.

2.2 Conference Publications

1. M. N. Haji, J. Kluger, T. Sapsis, and A. H. Slocum, "A Symbiotic Approach to the Design of Offshore Wind Turbines with Other Energy Harvesting Systems," In *Proceedings of the Offshore Energy and Storage 2017 Conference*, Cape Cod, MA, July 11-14, 2017. Oral presentation.

2. M. N. Haji, J. Drysdale, K. Buesseler, and A. H. Slocum, "Ocean Testing of a Symbiotic Device to Harvest Uranium from Seawater through the Use of Shell Enclosures", In *Proceedings of theTwenty-seventh (2017) International Ocean and Polar Engineering Conference*,San Francisco, CA, June 25-30, 2017.

3. A. H. Slocum, M. N. Haji, J. Kluger, and T. Sapsis, "Mechanics and materials in the design of symbiotic offshore energy harvesting systems," In *Proceedings of the 7th International Conference on Mechanics and Materials in Design*, Albufeira, Portugal, June 11-15, 2017.

4. M. N. Haji, M. E. Flicker Byers, E. A. Schneider, and A. H. Slocum, "Cost Analysis of Wind and Uranium from Seawater Acquisition symBiotic Infrastructure using Shell Enclosures", In *Proceedings of the 2017 ANS Meeting*, San Francisco, CA, June 11-15, 2017.

5. M. E. Flicker Byers, M. N. Haji, E. A. Schneider, and A. H.Slocum, "A Higher Fidelity Cost Analysis of Wind and Uranium from Seawater Acquisition SymBiotic Infrastructure",In *Proceedings of the 2016 ANS Winter Meeting and Nuclear Technology Expo*, Las Vegas, NV, November 6-10, 2016.

6. M. N. Haji and A. H. Slocum, "Design of a Symbiotic Device to Harvest Uranium from Seawater through the use of Shell Enclosures",In *Proceedings of the 2016 ANS Winter Meeting and Nuclear Technology Expo*, Las Vegas, NV, November 6-10, 2016.

7. M. N. Haji, C. Delmy, J. Gonzalez, and A. H. Slocum, "Uranium extraction from seawater using adsorbent shell enclosures via a symbiotic offshore wind turbine device", In *Proceedings of theTwenty-sixth (2016) International Ocean*

and Polar Engineering Conference,Rhodes, Greece, June 26-July 1, 2016.

8. M. N. Haji, C. Vitry, and A. H. Slocum, "Decoupling the functional requirements of an adsorbent for harvesting uranium from seawater through the use of shell enclosures," In *Proceedings of the 2015 ANS Winter Meeting and Nuclear Technology Expo*, Washington, DC, November 8-12, 2015.

2.3 Patents

1. M. N. Haji, A. H. Slocum, C. Vitry, Hard Permeable Outer Shell with Inner Uranium Adsorbing Material, provisional patent filed January 12, 2015.

2.4 Presentations

1. M. N. Haji "Symbiotic Systems for the Extraction of Minerals from Seawater," *National Wind Technology Center*, Boulder, CO, January 26, 2018. Invited presentation.

2. M. N. Haji "Addressing Seawater Mineral Extraction," *U.S. Department of Energy Water Power Technologies Office Marine Energy Technologies Forum: Distributed and Alternate Applications*, Washington, DC, December 5-7, 2017. Invited presentation.

3. M. N. Haji, J. Kluger, T. Sapsis, and A. H. Slocum, "A Symbiotic Approach to the Design of Offshore Wind Turbines with Other Energy Harvesting Systems," *Offshore Energy and Storage 2017 Conference*, Cape Cod, MA, July 11-14, 2017. Oral presentation.

4. M. N. Haji, J. Drysdale, K. Buesseler, and A. H. Slocum, "Ocean Testing of a Symbiotic Device to Harvest Uranium from Seawater through the Use of Shell Enclosures", *Twenty-seventh (2017) International Ocean and Polar Engineering Conference*,San Francisco, CA, June 25-30, 2017. Oral presentation.

5. A. H. Slocum, M. N. Haji, J. Kluger, and T. Sapsis, "Mechanics and materials in the design of symbiotic offshore energy harvesting systems," *7th International Conference on Mechanics and Materials in Design*, Albufeira, Portugal, June 11-15, 2017. Invited keynote presentation.

6. M. N. Haji, M. E. Flicker Byers, E. A. Schneider, and A. H. Slocum, "Cost Analysis of Wind and Uranium from Seawater Acquisition symBiotic Infrastructure using Shell Enclosures", *2017 ANS Meeting*, San Francisco, CA, June 11-15, 2017. Oral presentation.

7. M. E. Flicker Byers, M. N. Haji, E. A. Schneider, and A. H.Slocum, "A Higher Fidelity Cost Analysis of Wind and Uranium from Seawater Acquisition SymBiotic Infrastructure",*2016 ANS Winter Meeting and Nuclear Technology Expo*, Las Vegas, NV, November 6-10, 2016. Oral presentation.

8. M. N. Haji, and A. H. Slocum, "Design of a Symbiotic Device to Harvest Uranium from Seawater through the use of Shell Enclosures", *2016 ANS Winter Meeting and Nuclear Technology Expo*, Las Vegas, NV, November 6-10, 2016. Oral presentation.

9. J. Gonzalez, M. N. Haji, J. Drysdale, K. Buesseler, and A. H. Slocum, "The Effects of Protective Shell Enclosures on Uranium Adsorbing Polymers," *International Conference on Seawater Uranium Recovery*, College Park, MD, July 19-22, 2016. Poster presentation.

10. M. N. Haji and A. H. Slocum, "Design of a Symbiotic System to Extract Uranium from Seawater," *International Conference on Seawater Uranium Recovery*, College Park, MD, July 19-22, 2016. Oral presentation.

11. M. N. Haji, C. Delmy, J. Gonzalez, A. H. Slocum, "Uranium extraction from seawater using adsorbent shell enclosures via a symbiotic offshore wind turbine device", *Twenty-sixth (2016) International Ocean and Polar Engineering Conference*,Rhodes, Greece, June 26-July 1, 2016. Oral presentation.

12. M. N. Haji, C. Vitry, and A. H. Slocum, "Decoupling the functional requirements of an adsorbent for harvesting uranium from seawater through the use of shell enclosures," *2015 ANS Winter Meeting and Nuclear Technology Expo*, Washington, DC, November 8-12, 2015. Oral presentation.

13. M. N. Haji, A. H. Slocum, "Extraction of Uranium from Seawater: Design and Testing of a Symbiotic System," *2015 C3E Women in Clean Energy Symposium*, Cambridge, MA, November 4-5, 2015. Poster presentation.

14. M. N. Haji, C. Delmy, J. Gonzalez, A. H. Slocum, "Design of a Symbiotic System to Extract Uranium from Seawater," *Seawater Uranium Recovery Program*

Meeting, College Park, MD, August 6-7, 2015. Oral presentation.

15. M. N. Haji, C. Delmy, J. Gonzalez, A. H. Slocum, "Extraction of Uranium from Seawater: Design and Testing of a Symbiotic System," *NAKFI Advancing Nuclear Technologies Mid-Cycle Grant Meeting*, Chicago, IL, July 9, 2015. Oral and poster presentation.

16. M. N. Haji, C. Vitry, A. H. Slocum, "Design of a Symbiotic System to Extract Uranium from Seawater", *Seawater Uranium Recovery Program Meeting*, Oak Ridge, TN, January 12-13, 2015. Oral Presentation.

Introduction

The U.S. Energy Information Administration's recently released "International Energy Outlook 2013" projects that world energy consumption will grow by 56% between 2010 and 2040 (Energy Information Administration, 2013). With the global population forecasted to increase 33% by 2050 and over 50% by 2100 (Gerland et al., 2014), the rate of world energy consumption is expected to continue to rise over the century. At present, electricity production relies primarily on fossil fuels and is responsible for a large share of the carbon dioxide released to the atmosphere by human activities. The Intergovernmental Panel on Climate Change fourth assessment report stresses the importance of the reduction of anthropogenic greenhouse gas emissions in order to limit the extent of global warming (Intergovernmental Panel on Climate Change, 2007). These objectives pose a unique challenge in which alternative power generation methods with low carbon emissions will be required to address global warming in the midst of increased global energy needs.

Given that one gram of uranium-235 can theoretically produce, through nuclear fission, as much energy as burning 1.5 million grams of coal (Emsley, 2001), nuclear fission has the potential to significantly reduce carbon dioxide emissions from power generation. However, terrestrial supplies of uranium are greatly limited. A 2014 study by the Organization for Economic Cooperation and Development estimated that at the current consumption rate the global conventional reserves of uranium (7.6 million tonnes) could be depleted in a little over a century (OECD Nuclear Energy Agency, 2014). Additionally, as reserves decrease, uranium mining will shift to lower quality sites leading to a higher extraction cost and even greater environmental impact. A growing nuclear power sector will need access to significant uranium reserves at a reasonable cost of extraction.

Fortunately, uranium is present in the ocean as uranyl ions at a low concentration of 3-3.3μg/L (Oguma et al., 2011), which over the total volume of the oceans amounts to approximately 4.5 billion tonnes of uranium, nearly a thousand times that of conventional reserves (Tamada, 2009). Finding a sustainable way to harvest uranium from seawater will provide a source of uranium for generations to come. Furthermore, it gives all countries with ocean access a stable supply and eliminates the need to store spent fuel for potential future reprocessing, thereby also helping to address nuclear proliferation issues.

Background Research

Extraction of uranium from seawater has been researched for decades, with one of the first studies conducted by Davies et al. (1964) after World War II in an effort to secure uranium supply for Britain at a time when the production of uranium was uncertain. A recent review of all proposed uranium recovery technologies by Kim et al. (2013) identified uranium adsorption by chelating polymers to be the most promising in terms of cost, adsorption capacity, and environmental footprint (Zhang et al., 2003; Seko et al., 2003; Anirudhan et al., 2011). Other techniques including membrane filtration, coagulation, and precipitation were found to have issues such as high operating costs, durability, or toxicity (Kanno, 1984; van Reis and Zydney, 2007; Tularam and Ilahee, 2007).

Chelating polymers allow for the passive extraction of uranium from seawater by adsorption. The polymers are first deployed in seawater and remain submerged until the amount of captured uranium approaches the adsorbent capacity. At this point, elution is used to strip the uranium from the polymers. During this process, the adsorbent is immersed in acid solutions of increasing concentration to recover uranium and remove other elements that have bonded to the polymer. The adsorbent polymer may undergo a number of elution cycles before being regenerated by an alkali wash so that its functional groups are freed and the adsorbent can be reused. The output from the elution process undergoes purification and precipitation typical for mined uranium to produce yellowcake. Past work has focused on systems in which the adsorbent is brought back to shore for the elution process and redeployed afterward. However, these stand-alone intermittent operation systems have significant practical and economic deployment challenges (Seko et al., 2003) and to date none of these systems have become economically viable.

Several of the polymer adsorbent system concepts have been subject to marine tests to evaluate performance, feasibility and cost-effectiveness. The Japanese Atomic Energy Agency (JAEA) first developed a system of buoy floated stacks of adsorbent fabric (Figure 4.1). However, due to the large weight of the mooring equipment, mooring operations were found to account for more than 70% of the cost of this concept (Sugo et al., 2001; Seko et al., 2003).

To address this problem, a buoyant braid adsorbent made of polyethylene fibers on a polypropylene trunk was proposed by Tamada et al. (2006) (Figure 4.2). This design was found to achieve a reduction of 40% of the cost of uranium recovery compared to the adsorbent stack system, resulting in an estimated uranium production cost of $1000/kg-U (Tamada et al., 2006). An independent cost-analysis by Schneider and

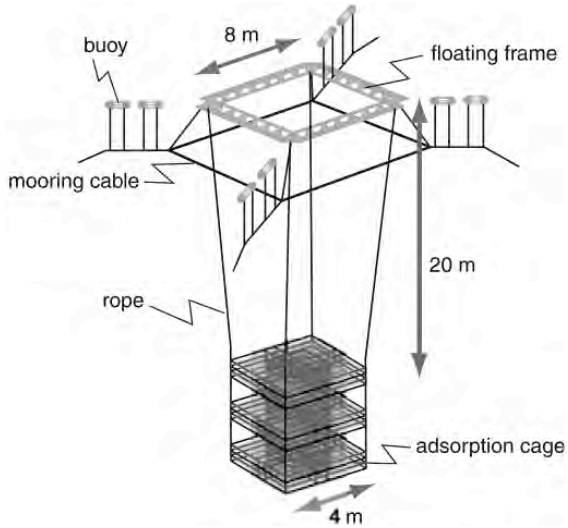

Figure 4.1: Uranium collection system for adsorbent stacks (Seko et al., 2003).

Sachde (2013) of the system yielded a production cost of $1230/kg-U. The difference in cost was mainly attributed to the consideration of a 5% degradation of adsorbent capacity per use cycle. Further sensitivity studies confirmed that the major cost divers of such a system were the adsorbent capacity, number of recycles, and capacity degradation. For instance, if the capacity of the adsorbent was increased from 2 kg-U/t-ads to 6 kg-U/t-ads and the number of recycles was increased from 6 to 20, with no degradation and unchanged adsorbent production costs, the uranium production cost would drop to $299/kg-U (Schneider and Sachde, 2013). In comparison, the market price of uranium has ranged from a current low of $81/kg-U to a peak of $300/kg-U in 2007 when demand for nuclear power was higher.

Previous studies show that a major cost driver of harvesting uranium from seawater is the mooring and recovery of the adsorbent (Schneider and Sachde, 2013). Additionally, work by Picard et al. (2014) demonstrated that, due to the kinetics of the adsorbent, the recovery rate of uranium of the adsorbent can be increased by shortening the harvest period. For instance, as shown in Figure 4.3, when the period of uranium recovery from the adsorbent is reduced from 60 to 30 days, the amount of

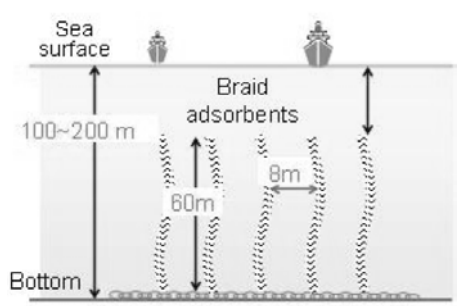

Figure 4.2: Uranium collection system for braid adsorbent (Tamada et al., 2006).

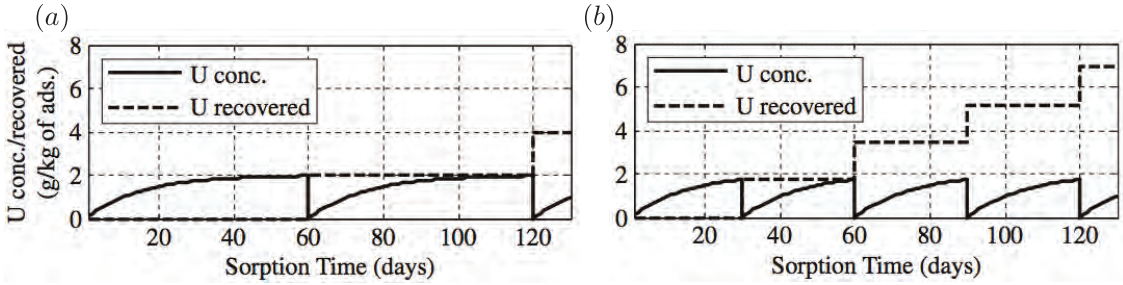

Figure 4.3: Adsorption kinetics. Resulting uranium concentration and uranium recovering (g/kg-ads) for a harvest period of (*a*) 60 days and (*b*) 30 days. (Picard et al., 2014).

uranium collected over 120 days increases from 4 g-U/kg-ads to 7 g-U/kg-ads. Based on this observation, Picard et al. (2014) pursued the development of a system, which continuously takes the adsorbent from the ocean through an elution process and then returns it to the ocean allowing control over the harvest period. The system is designed to function attached to turbines of an offshore wind farm, thereby eliminating the offshore mooring cost while also increasing the energy output of the wind farm, yielding a production cost of $403/kg-U.

This project seeks to build upon the work of Picard et al. (2014) and focus on integrating the design of a uranium harvesting system into an offshore wind turbine tower. The rational is that the development of offshore wind or uranium harvesting by themselves bears a high capital cost for the structures, but if the mooring function can be shared, the overall cost for each will be lower. Figure 4.4 shows the concept developed by Picard et al. (2014) in which a platform at the base of the wind tower supports a belt of adsorbent that loops in and out of the water. The belt slowly cycles through the seawater beneath the tower and through an elution plant located on the platform. The belt is weighted in the seawater by rollers which also space out the loops and prevent the belt from tangling. The proposed system was sized to collect 1.2 tonnes of uranium per year, a sufficient amount to supply a 5 MW nuclear power. This would require 4 km of adsorbent belt for a total weight of 120 tonnes of adsorbent per wind turbine per year. To harvest enough uranium for a 1 GW nuclear power plant would require 214 wind turbines and a total of over 25000 tonnes of adsorbent per year. Preliminary analysis conducted by Picard et al. (2014) on the adsorbent belt and structural design to determine the first order scaling laws for this concept indicate that such a system is technically feasible.

Picard et al. (2014) designed, built, and pool tested a 1/50th scale prototype to study the feasibility of a symbiotic uranium harvester and wind turbine system, with cables replacing the absorbent net (Figure 4.5). This prototype demonstrated that such a system could mechanically work and that weighted rollers could be configured such that the system would be stable and the loops of adsorbent belt would be roughly the same length as the belt cycles through the system. The test also indicated that the system could withstand moderate currents, by having divers kick at the system, when a bottom roller system was used to maintain tension in the cables and keep

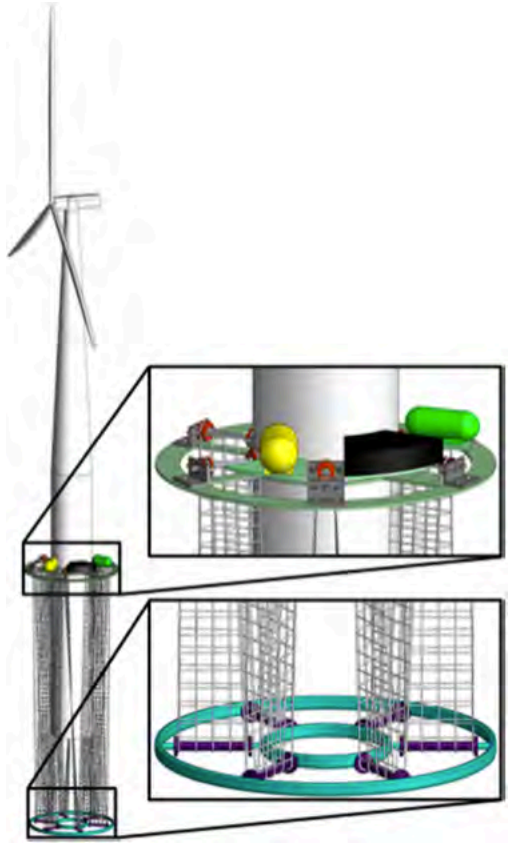

Figure 4.4: Three-dimensional view of continuous uranium recovery system with adsorbent belt looped around the turbine mast proposed by Picard et al. (2014). The elution plant is housed on the upper platform out of the seawater.

them separated.

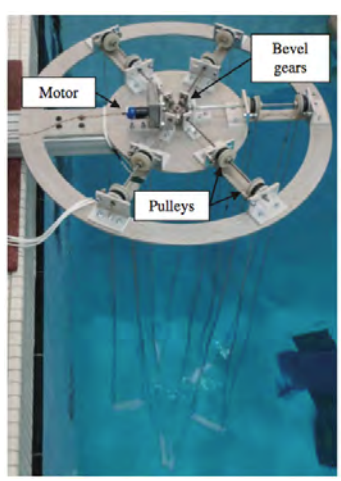

Figure 4.5: 1/50th scale model of Picard et al. (2014) being tested in a pool.

This project seeks to evaluate many possible methods for using an offshore wind turbine structure to serve as a base for uranium harvesting, and thus will not limit itself to belts. In addition, the mechanics of deployment and retrieval systems for refurbishment, of the adsorbent, which has a limited life, will be developed. A fundamental contribution will thus be a cost of ownership (deployment and maintenance) model for different design options.

Why offshore wind turbines? Given the low concentration of uranium in seawater, 3 μg/L, in order to harvest 240 tonnes of uranium required to power a 1 GW power plant requires an onshore plant that can pump 5100 m^3/s of seawater through the plant, or approximately 160 km^3 of seawater per year. If the seawater for the onshore harvesting system was also used to provide cooling water in addition to nuclear fuel for the 1 GW nuclear power pant, 5100 m^3/s of flow represents about 21 GW/C of cooling potential or enough cooling capacity for 315 GW of electric power generation, which is about 150 times what is needed for the power plant (Union of Concerned Scientists, 2011). Given the amount of water that would need to be pumped for an onshore system, far more than is required to cool a nuclear reactor, it is more cost-effective to forgo active pumping and instead locate the uranium harvesting system offshore using the ocean currents to flow water past the device.

Desalination plants routinely pump seawater onshore generating a supply of freshwater and a brine mixture that has a concentration 3 times that of seawater. The feasibility for harvesting uranium from the brine produced from a desalination plant was also investigated. To harvest 240 tonnes of uranium required to power a 1 GW power plant would require 53 km^3 of brine flow per year, which would be produced from a desalination plant that generates 77 billion gallons of freshwater per day. This plant would have to be able to generate 285 times more freshwater than the largest desalination plant in the world, Ras al-Khair in Saudi Arabia which produces 270 million gallons of freshwater per day. The sheer volume of water required for the case of harvesting uranium from brine further emphasizes an offshore uranium harvesting system is more cost-effective.

Mechanical Investigation of Sorption Optimization (MISO)

As part of this project, a tool was developed to optimize the adsorbent length and travel speed to minimize annual system cost/kg-U, adsorbent degradation and replacement cost. The algorithm developed, known as Mechanical Investigation of Sorption Optimization (MISO), is described in this chapter.

5.1 Recovery Rate

According to Saito et al. (2014), the uranium complexation with amidoxime is presumed to follow a one-site ligand saturation model, where the uranium uptake, C_0, after a certain exposure time in days, t, is given by

$$C_0 = \frac{\beta_{max} t}{K_D + t}, \tag{5.1}$$

where β_{max} is the saturation capacity in kg-U/t-ads, and K_D is the half-saturation time in days, both properties of the adsorbent used from Gill et al. (2016). After initial conditioning, the adsorbent capacity is degraded by a marginal amount. The ratio of adsorbent capacity after initial conditioning pre-deployment to theoretical capacity is taken to be $C_{ratio} = 90\%$ for this study. Therefore, the actual adsorbent capacity is

$$C = C_{ratio} C_0 = C_{ratio} \frac{\beta_{max} t}{K_D + t}. \tag{5.2}$$

Due to the kinetics of the adsorbent, the recovery rate of uranium of the adsorbent can be increased by shortening the harvest period. For instance, as shown in figure 5.1, when the period of uranium recovery from the adsorbent is reduced from 60 to 30 days, the amount of uranium collected over 120 days increases from 7 g-U/kg-ads to 11 g-U/kg-ads.

Taking $t = T_h$ be the harvest period, the rate of uranium recovery, R, is defined as follows,

$$R = \frac{C(T_h)}{T_h} = \frac{C_{ratio} \frac{\beta_{max} T_h}{K_D + T_h}}{T_h}. \tag{5.3}$$

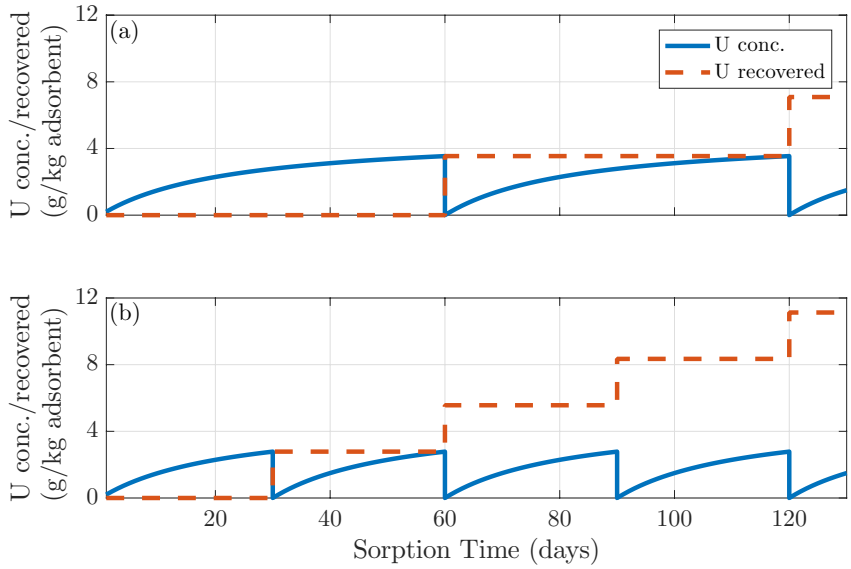

Figure 5.1: Adsorption kinetics. Resulting uranium concentration and uranium recovering (g/kg-ads) for a harvest period of (a) 60 days and (b) 30 days for the AF1 adsorbent.

The recovery rate reaches a maximum as the harvest period approaches zero:

$$\lim_{T_h \to 0} R = \frac{C_{ratio} \frac{\beta_{max} T_h}{K_D + T_h}}{T_h} = \frac{C_{ratio} \beta_{max}}{K_D}. \tag{5.4}$$

The variation of the uranium recovery rate with the harvest period for the AF1 adsorbent is shown in figure 5.2. The final choice of harvest period is a compromise between obtaining the highest recovery rate and minimizing damage to the adsorbent from more frequent elution.

5.2 Adsorbent Degradation

Experimental observation has shown that adsorbents can lose as much as 20% of their initial capacity over five adsorption/elution cycles (Seko et al., 2004). It is believed that exposure to highly concentrated acid causes damage to the functional groups of chelating polymer adsorbent thus reducing their capacity. To model degradation during elution, it can be assumed that the time the adsorbent is exposed to the acid solution and the solution pH remain constant regardless of the recovery period. This is indeed necessary to make sure that all of the uranium is extracted from the adsorbent. Consequently, the relative loss of adsorbent capacity is assumed to be constant at each elution cycle since the damage to the adsorbent is expected to be the same.

As shown in (Picard et al., 2014), the capacity of the adsorbent after n elution cycles can be written as

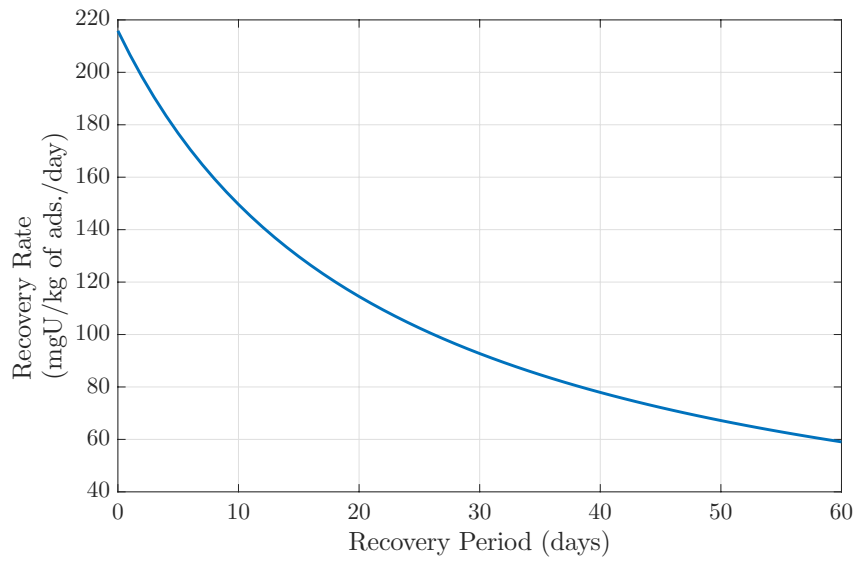

Figure 5.2: Recovery rate of uranium, R, as a function of the harvest time, T_h, for the AF1 adsorbent.

$$C_n = C(1-d)^n. \tag{5.5}$$

Additionally, the average capacity of the adsorbent over n adsorption/elution cycles can be calculated using a geometric progression:

$$\bar{C} = \frac{1}{n}\sum_{k=0}^{n-1} C(1-d)^k = \frac{C}{n}\left[\frac{1-(1-d)^n}{d}\right]. \tag{5.6}$$

5.3 Mechanical Parameters

From (5.2) and (5.5), it is clear that the two mechanical parameters involved in the recovery of uranium are the time of exposure of the adsorbent to seawater, t, and the number of elution cycles of the adsorbent before replacement, n. After one cycle, the amount of uranium adsorbed in g-U/kg-ads, Γ_1, after a harvesting time of t_1, is given by

$$\Gamma_1 = C_{ratio}\frac{\beta_{max}t_1}{K_D + t_1}. \tag{5.7}$$

However, for every cycle thereafter, the degradation of the adsorbent becomes a factor. For instance, the amount of uranium adsorbed in g-U/kg-ads after two cycles, Γ_2, each with a harvest time of t_1 and t_2 respectively is

$$\Gamma_2 = C_{ratio}\frac{\beta_{max}t_1}{K_D + t_1} + C_1\frac{\beta_{max}t_2}{K_D + t_2}, \tag{5.8}$$

where C_1 is the capacity of the adsorbent after one elution cycle. As a result, Γ_2 becomes

$$\Gamma_2 = C_{ratio}\frac{\beta_{max}t_1}{K_D + t_1} + C_{ratio}\frac{\beta_{max}t_2}{K_D + t_2}(1-d). \tag{5.9}$$

Following this procedure, assuming that the harvest time for each cycle is the same, that is $t_1 = t_2 = \cdots = t_n = t$, the amount of uranium adsorbed in g-U/kg-ads after n cycles, Γ_n, is

$$\Gamma_n = C_{ratio}\frac{\beta_{max}t}{K_D + t}\left[1 + (1-d) + (1-d)^2 + \cdots + (1-d)^{n-1}\right]. \tag{5.10}$$

For this geometric progression, the amount of uranium adsorbed in g-U/kg-ads after n cycles, Γ_n, becomes

$$\Gamma_n = C_{ratio}\frac{\beta_{max}t}{K_D + t}\left[\frac{1-(1-d)^n}{d}\right]. \tag{5.11}$$

From (5.11), it is clear that if the chemical properties of the adsorbent are fixed (C_{ratio}, β_{max}, K_D, and d), the harvest time, t, and the number of elution cycles, n, are the mechanical parameters that determine Γ_n, the amount of uranium adsorbed in g-U/kg-ads after n cycles.

5.4 Sorption Optimization

The soprtion process can be mechanically optimized by using (5.11) and the chemical parameters for the AF1 adsorbent from (Gill et al., 2016):

- Saturation capacity: $\beta_{max} = 5.421$ kg-U/t-ads,
- Half-saturation time: $K_D = 22.6$ days,
- Degradation per cycle: $d = 5$ %.

The functional requirements of the symbiotic system require that 1.2 tonnes of uranium are harvested annually, therefore the parameter space can be further analyzed to highlight the combinations of harvest time and elution cycles that are feasible, as shown in figure 5.3. Additionally, the amount of adsorbent required on the system as a function of t and n can also be determined, the results of which are shown in figure 5.4. As can be seen from the Figures 5.3 and 5.4, the parameters chosen by (Picard et al., 2014) would not fit within the one year time limit. The optimal values for the AF1 adsorbent within this timeframe actually occur with $t = 23$ days and $n = 15$ cycles, resulting in Γ_{15} ∼26 kg-U/t-ads and requiring ∼45 t-ads.

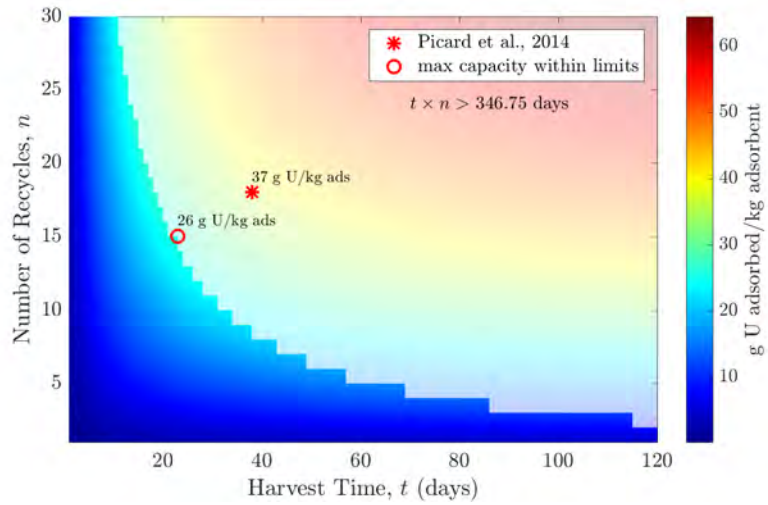

Figure 5.3: Amount of uranium adsorbed in g-U/kg-ads, Γ_n, as a function of harvest time, t, and number of elution cycles, n considering the AF1 adsorbent with $\beta_{max} =$ 5.421 kg-U/t-ads, $K_D = 22.6$ days, and $d = 5$ (Gill et al., 2016). The value resulting from t and n from the study conducted by Picard et al. (2014) is indicated by the red star. Parameter combinations outside of the one year timeframe are shaded. The optimal value within the limited region is shown by the red circle.

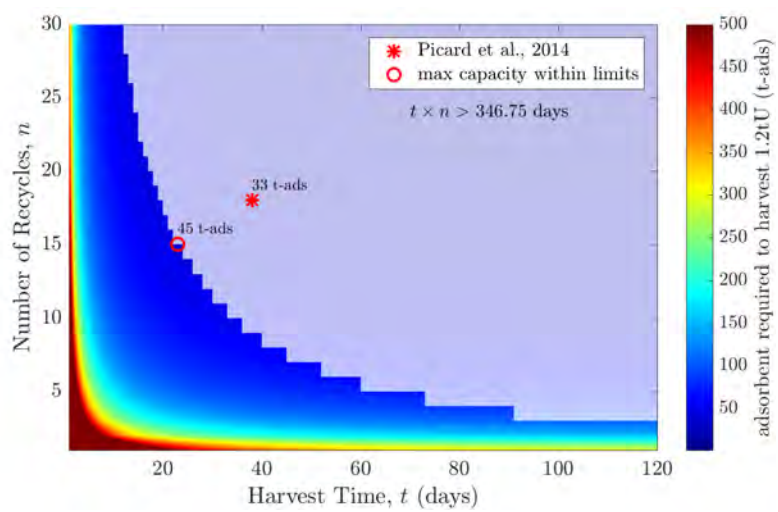

Figure 5.4: As in figure 5.3 but for the amount of adsorbent required in kg to harvest 1.2 t-U annually.

Seawater Uranium Suitability of Harvesting Index (SUSHI)

A modeling tool was developed combining world population density, ocean currents, wind data, and sea surface temperatures to identify areas in which harvesting uranium from seawater in a symbiotic system with an offshore wind turbine is most cost-effective. The adsorbent chemistry and optimum wind speed are variables in the model so that it can be utilized for a wide variety of adsorbents and wind turbines. Known as the Seawater Uranium Suitability of Harvesting Index (SUSHI), the latest version of the tool is described in this section.

6.1 Motivation

The Suitability Index is defined to be how appropriate a location is to the harvesting of uranium from seawater by way of a symbiotic system attached to an offshore wind turbine support structure. The index is comprised of the wind power potential of various sites around the globe as well as the adsorbent capacity, which is dependent on temperature and light, in those regions. This number is then normalized by that of a similar deployment strategy off the coast of southern Japan, a location where many previous studies of seawater uranium harvesting have taken place (Seko et al., 2003; Sugo et al., 2001; Tamada et al., 2006; Tamada, 2009).

6.2 Incorporated factors

6.2.1 Wind Power

Of importance in siting an offshore wind turbine is the power potential at that location. Wind power is proportional to the cube of the wind speed by:

$$P = \frac{1}{2}\eta\rho A v^3, \tag{6.1}$$

where P is the wind power, η is the efficiency of the turbine, ρ is the density of air, A is the rotor area of the wind turbine, and v is the speed of the wind perpendicular to the turbine rotor. In this model, it is assumed that the only variable in the turbine design is its site offshore, therefore in (6.1), only v is changing from location to location.

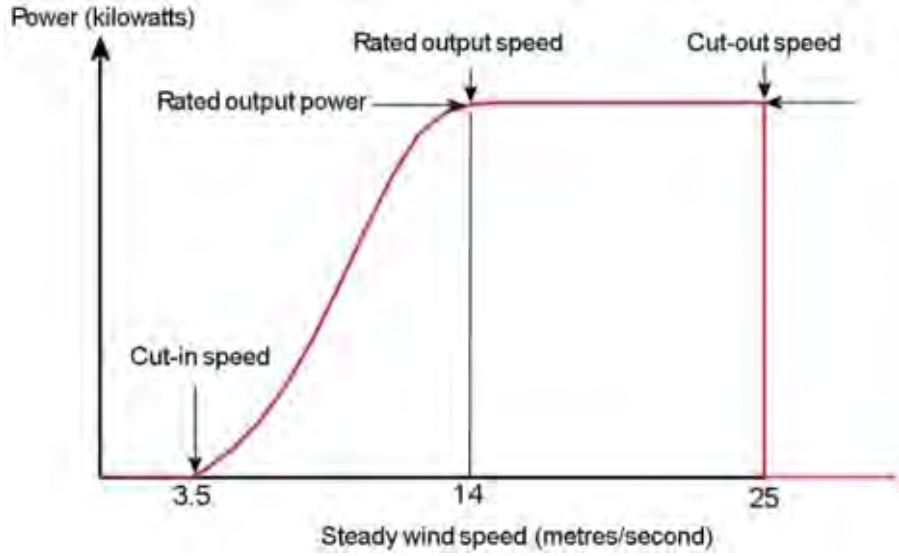

Figure 6.1: Typical wind turbine power output curve (PelaFlow Consulting, 2008).

The ocean surface wind dataset available only provides the wind speeds near the ocean surface, ∼10m high. Offshore wind turbines operate at much higher heights, 80m-100m. Therefore, the wind speed near the surface was related to the wind speed at an arbitrary height by

$$v_r = v_a \left(\frac{z_r}{z_a} \right)^{\nu}, \tag{6.2}$$

where v_r is the unknown wind speed at height z_r, v_a is the measured wind speed at height z_a, and ν is the power law wind speed shear exponent (Elliot et al., 1987). For this calculation, ν was chosen to be 0.11 based on validation with updated offshore wind maps and other analyses of offshore wind resources that indicate that the shear exponent is most often in the range from 0.08 to 0.14 for the offshore regions of the United States (Schwartz et al., 2010).

Given that the typical wind turbine power output curve is not constant, as shown in figure 6.1, the minimum and maximum operation speeds of the wind turbine are left as inputs to SUSHI. These speeds correspond to the cut-in speed and cut-out speed shown in figure 6.1, respectively. To account for this power curve, v_r' is defined to be the resulting dataset after adjusting v_r from (6.2) to remove any speeds below the cut-in speed and above the cut-out speed of the wind turbine. Finally, since the wind power is proportional to the cube of the wind speed by (6.1), a matrix, M_v, of the wind speeds cubed relating to each location on the globe was defined from the adjusted wind speed at the turbine height, v_r':

$$M_v = v_r'^3. \tag{6.3}$$

6.2.2 Adsorbent capacity

Sekiguchi et al. (1994) concluded that there is a noticeable effect of seawater temperature on the adsorbent capacity in harvesting uranium from seawater. They found that in general, the capacity coefficient of the amidoxime adsorbent increased with increased seawater temperature. Tamada (2009) also noted the seawater temperature increased the uranium adsorption (figure 6.2), from two adsorbent experiments. In the first experiment, adsorbent stacks were deployed in the Mutsu area in which the seawater had a temperature of 20°C and in the second experiment, braided adsorbent was tested off the coast of Okinawa, where the seawater temperature was 30°C. This 10°C difference enhanced the uranium adsorbent of the adsorbent stacks by 1.5 times, as shown in figure 6.2.

Through recent experiments by PNNL, the relationship between ocean temperature and the uptake of uranium by adsorbents developed by ORNL was determined (Gill et al., 2014). For this study, time series data for the uptake of the adsorbent was measured at different temperatures. Given the limited data, a linear regression was performed on all the adsorbent types analyzed in the PNNL marine experiments (Byers, 2015). The results of the temperature dependence of the kinetic parameters, β_{max} and K_D, for the three ORNL adsorbents is shown in figure 6.3.

In the case of the AF1 adsorbent, only two temperature experiments were utilized for the linear model fit because the data from the experiment containing the fiber at

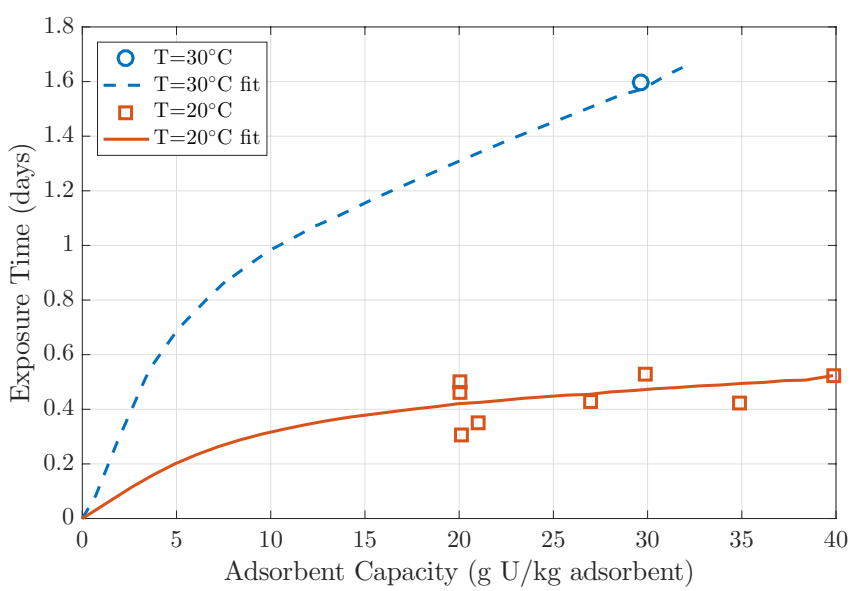

Figure 6.2: Uranium adsorbent capacity (g-U/kg-ads) as a function of soaking time in days and water temperature from Tamada (2009). Data from two adsorbent experiments were used: braided adsorbent that was in T=20°C (red squares) and adsorbent stacks that were in T=30°C blue circles). The dotted blue line and solid red line represent the one-site ligand-saturation model fit to the data for the braided adsorbent and adsorbent stacks, respectively.

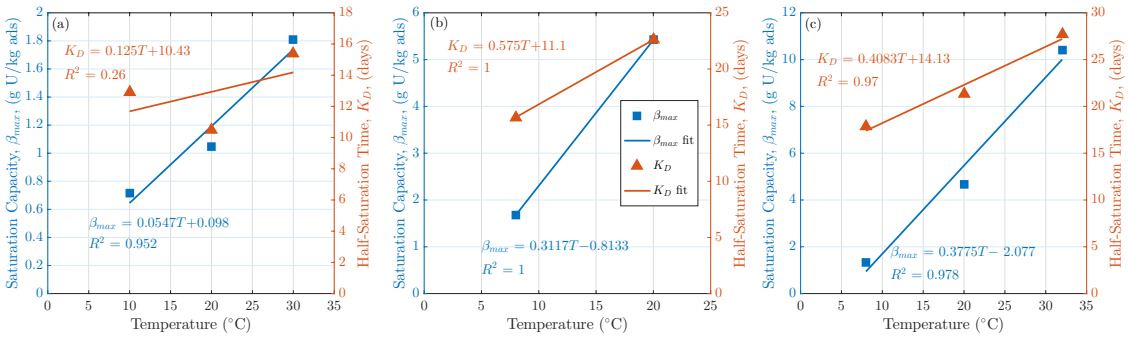

Figure 6.3: Temperature dependance of kinetic parameters β_{max} (blue squares) and K_D (red triangles) for (a) 38H, (b) AF1, and (c) AI8 ORNL adsorbents as determined by experiments by PNNL. The blue and red lines indicate the linear fit of the β_{max} and K_D data sets respectively (Gill et al., 2014)

32° was not usable. The high R^2 values for the same linear regression used on the kinetic parameters for the other two adsorbents suggests that the linear regression model could be used for the case of the AF1 adsorbent as well. Furthermore, there was agreement within 5% of the the linear fit model for the AF1 adsorbent with one recoverable data point from the missing dataset, further suggesting the linear fit was reasonable (Byers, 2015).

The temperature dependent models for the coefficients β_{max} and K_D can then be placed back into the one-site ligand model, (5.1), to yield the following temperature dependent relationships for uranium uptake of the 38H, AF1, and AI8 adsorbent, respectively

$$C_{max,38H} = \frac{(0.0547T + 0.098)t}{(0.125T + 10.43) + t}, \tag{6.4}$$

$$C_{max,AF1} = \frac{(0.3117T - 0.8133)t}{(0.575T + 11.1) + t}, \tag{6.5}$$

$$C_{max,AI8} = \frac{(0.3775T - 2.077)t}{(0.4083T + 14.13) + t}, \tag{6.6}$$

where C_{max} is the uranium uptake of the adsorbent (g-U/kg-adsorbent) and T is the temperature in °C. Figure 6.4 shows the resulting time-dependent uptake for the AI8 adsorbent for T = 10°C, 15°C and 20°C as predicted by (6.6). As can be seen from the figure, just a 5° difference in temperature results in an over 50% increase in the uranium uptake. This is critical because, with the exception of the surface mixed layer, most of the seawater in the ocean is at temperatures ranging from $\approx 5 - 10$°C, suggesting that uptake of uranium in an ocean setting for all these adsorbents will likely be much less than the adsorbent capacities determined in the lab experiments presented here.

Depending on the type of adsorbent chosen for analysis (38H, AF1, or AI8), the adsorbent capacity is determined by equation (6.4), (6.5), or (6.6). As a result of this

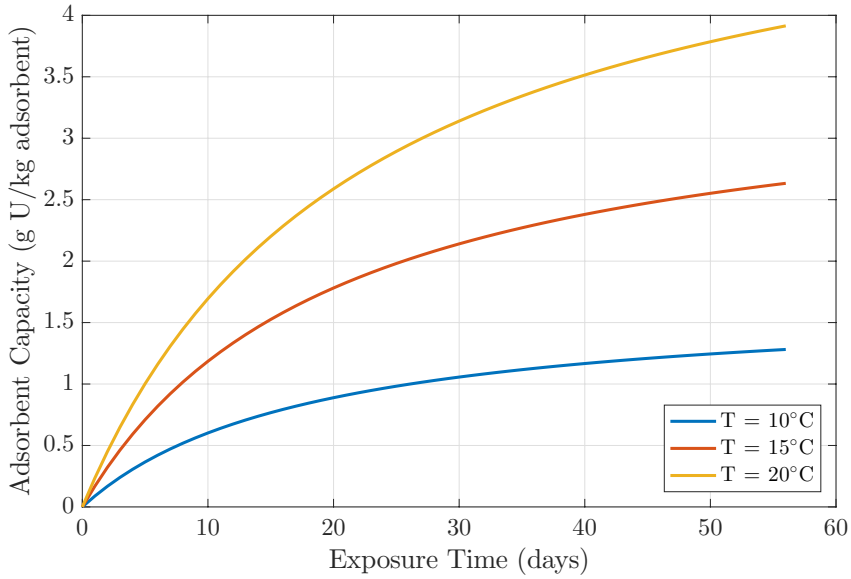

Figure 6.4: Time-dependent uptake of uranium for the AI8 adsorbent fiber as predicted by (6.6) for T = 10°C (blue), 15°C (red) and 20°C (yellow).

dependence of adsorbent capacity on seawater temperature, a matrix of adsorbent capacity at all locations on the globe, M_k, is defined using (6.4), (6.5), or (6.6), and a specific campaign length, t. The total uranium adsorbed per tonne adsorbent after n uses is given by equation (5.11) which is computed for a specific temperature, campaign length, number of uses, and degradation per cycle.

6.3 Suitability Index

At present, the Suitability Index is a function of the potential wind power and adsorbent capacity of various locations across the globe. Additionally, a reference location is chosen to aid in the comparison of various potential seawater uranium sites. Using the resulting matrix of wind speeds at the turbine height cubed, M_v and the adsorbent capacity, M_k at all locations around the globe the suitability index is defined as

$$SI = \left(\frac{M_v}{v_0^3}\right)^{\alpha} \left(\frac{M_k}{k_0}\right)^{\beta} \tag{6.7}$$

where v_0 is the wind speed at the reference location and k_0 is the adsorbent capacity at the reference location. In the SUSHI tool, $\alpha = \beta = 1$, that is the wind power potential and adsorbent capacity of the region are weighted equally. The reference location is taken to be 128.5°E, 26.5°N, a location off the coast of southern Japan, where many previous experiments of uranium harvesting adsorbents have been conducted (Seko et al., 2003; Sugo et al., 2001; Tamada et al., 2006; Tamada, 2009).

Resulting values of the Suitability Index (SI) can range from 0 to any positive

number. Values equal to 1 indicate places where uranium harvesting would be as suitable as offshore of the southern coast of Japan. Sites with SI values less than 1 indicates areas where uranium harvesting is less suitable and locations with SI values greater than 1 are more suitable for uranium harvesting than off the coast of southern Japan.

6.4 Datasets

This section provides details about the datasets utilized by the latest version of the SUSHI tool. All datasets are publicly available and were provided by either NASA or NOAA.

6.4.1 Ocean surface winds

The ocean surface winds dataset was retrieved from the NASA Jet Propulsion Laboratory Physical Oceanography Distributed Active Archive Center (PODAAC). The specific dataset is the "SeaWinds on QuikSCAT Level 3 Surface Wind Speed for Climate Model Comparison" that was produced by the QuickSCAT Project. Launched in June of 1999, QuickSCAT was designed to be a"quick recovery" EOS satellite mission to fill the gap of global ocean surface wind vector observations which resulted from the unexpected failure of NSCAT in June of 1997.

This dataset was then utilized to determine the wind speed at the turbine height, as described in section 6.2.1. The following are the details of the QuickSCAT dataset for the ocean surface winds:

- Spatial Resolution: 1 degrees (Latitude) x 1 degrees (Longitude)
- Longitude Range: 180°W to 180°E
- Latitude Range: 89.6°S to 89.6°N
- Temporal Resolution: 1 month
- Time Span: 1999-Aug-01 to 2009-Oct-31
- Variables: sfcWind - Near-surface wind speed (10m above ocean surface)
- Units: m/s
- Plotted Variable: Long term mean (1999-2009) wind speed for input month or the average over all months

More information about the dataset can be found on the PODAAC website:
`http://podaac.jpl.nasa.gov/dataset/QSCAT_L3_SFC_WIND_SPEED_1DEG_1MO`

6.4.2 Sea surface temperature

The sea surface temperature dataset was derived from the NOAA Earth Systems Research Laboratory. It is titled "NOAA Optimum Interpolation (OI) Sea Surface Temperature (SST) V2" and includes long term mean information from the years 1971 to 2000. The data was produced using both in situ and satellite data (Reynolds et al., 2002).

This dataset was utilized to determine the adsorbent capacity at various sites across the globe. The details of the dataset are as follows:

- Spatial Resolution: 1 degrees (Latitude) x 1 degrees (Longitude)
- Longitude Range: 0°E to 360°E
- Latitude Range: 89.5°S to 89.5°N
- Temporal Resolution: 1 month
- Time Span: 1971 to 2000
- Variables: sst - sea surface temperature
- Units: °C
- Plotted Variable: Long term mean (1971-2000) temperature for input month or the average over all months

More information about the dataset can be found on the NOAA website:
`http://www.esrl.noaa.gov/psd/data/gridded/data.noaa.oisst.v2.html`

6.5 GUI Presentation

This section presents a detailed explanation of the SUSHI graphical user interface (GUI) along with a step-by-step example to demonstrate how to run the code.

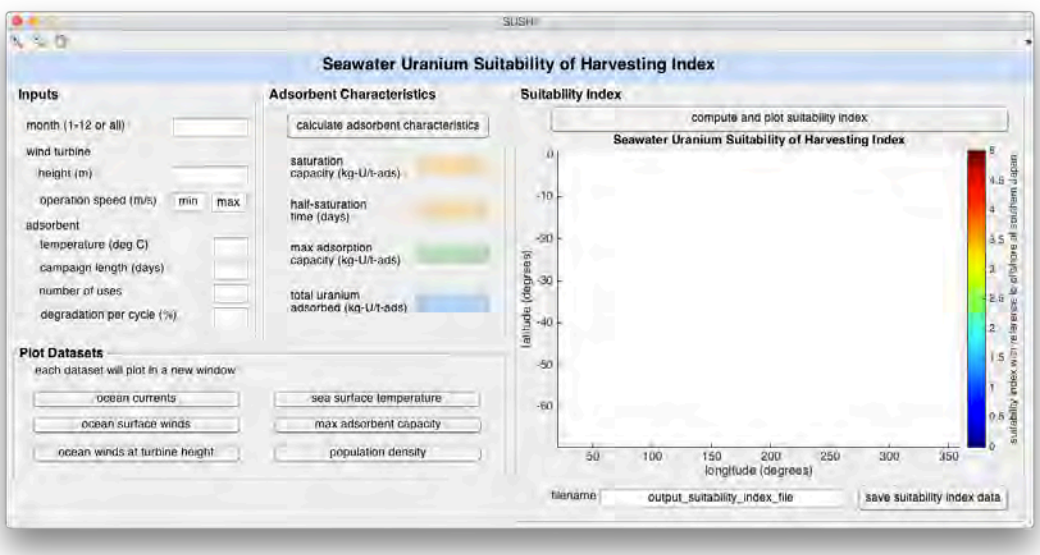

Figure 6.5: SUSHI GUI

The SUSHI package provides a GUI that combines all the datasets necessary for determining the suitable global sites for seawater uranium harvesting. A screenshot of the GUI is provided in figure 6.5. The steps detailed below describe what the user must do in order to get started using the GUI.

Step 1 defines the inputs required by the tool. Step 2 allows the user to plot the datasets utilized by the calculation. Step 3 then utilizes the user input parameters

and dataset variables to determine the suitable sites for the harvesting of uranium from seawater. More details on each specific element to provide to the GUI are listed below.

Step 1: Inputs

- **Month:** The month of interest must be entered into the program using the values 1-12 corresponding to the months of the year, or the term "all" to average the data over all months. This input is required due to the high seasonality of global sea surface temperatures and winds. If no value is entered, the default month value of 6 (corresponding to June) is utilized by the tool.
- **Wind Turbine Height:** The height in meters of the wind turbine is required by the tool. This value is used order to determine the wind speeds at the turbine's height. If no value is entered, a standard height of 90m is used.
- **Wind Turbine Operation Speed:** The minimum and maximum operation speeds of the wind turbine must be entered in m/s. These values are used to determine sites suitable for offshore wind farms. If no values are entered, reference values for the minimum and maximum speeds of 3.5 m/s and 25 m/s are used, respectively.
- **Adsorbent Temperature:** The temperature in °C at which you would like to determine the maximum adsorption capacity. If no value is given, 20°C is utilized.
- **Campaign Length:** The time in days that the adsorbent is submerged in seawater. If no value is given, a default campaign length of 30 days is used.
- **Number of Uses:** The number of times the adsorbent is eluted in order to harvest uranium before the adsorbent is discarded. If no value is given, the number of uses is taken to be 12.
- **Degradation per Cycle:** The adsorbent degradation in percentage after each use due to the acid elution bath. If no value is given, the degradation per cycle is taken to be 5%.

Step 2: Adsorbent Characteristics

It might be of interest to the user to know the characteristics of the adsorbent given the adsorbent inputs in Step 1. The characteristics computed are

- **Saturation Capacity:** The saturation capacity of the adsorbent in kg-U/t-ads. This value is temperature dependent and is computed using the reference temperature inputted in Step 1.
- **Half-Saturation Time:** The half-saturation time of the adsorbent in days. This value is temperature dependent and is computed using the reference temperature inputted in Step 1.

- **Maximum Adsorption Capacity:** The maximum adsorption capacity in kg-U/t-ads of the adsorbent as defined using a one-site ligand model from values inputted in Step 1.
- **Total Uranium Adsorbed:** The total uranium adsorbed in kg-U/t-ads for the lifetime of an adsorbent using the inputs given in Step 1.

Step 2: Plot Datasets

In this step, the user can preview the global datasets utilized by the tool in computing the Suitability Index. Each dataset selected will be shown in a new window. More information about each dataset is described in section 6.4. The global region plotted is between 20.5°E - 359.5°E and 69.5°S - 69.5°N because these are the common locations at which all datasets are defined.

- **Ocean Currents:** The long term mean ocean currents in m/s from 1993-2003 are displayed. Figure 6.6 shows the typical output. Recent work Ladshaw et al. (2017) has shown that linear flow rates as low as 4 cm/s are more than enough to provide enough water flow to make a seawater uranium harvester feasible, therefore the ocean currents are not incorporated into the present Suitability Index. However, should seawater uranium harvesting systems be limited in the currents required, this dataset could easily be incorporated into an updated Suitability Index. It also expands the potential for SUSHI to consider additional symbiotic uses for the offshore structure that supports the turbine such as underwater turbines for power generation or perhaps even aquaculture systems that rely on currents.
- **Ocean Surface Winds:** Selecting this option plots the long term mean of the ocean surface winds in m/s for the month selected or the average for all months (in the case that the user inputs "all") from 1999-2009. Figure 6.7 displays the result for the default month of June. This dataset is used to determine the ocean surface winds at the height of the wind turbine.
- **Ocean Winds at Turbine Height:** This option plots the long term mean of the ocean winds at the entered turbine height in m/s for the month selected or the average for all months (in the case that the user inputs "all") from 1999-2009.
- **Sea Surface Temperature:** The long term mean sea surface temperature in °C from 1971-2000 for the desired month or the average for all months (in the case that the user inputs "all") is plotted. A typical output plot is displayed in figure 6.8. This dataset is utilized to determine the likely adsorbent capacity for sites around the globe.
- **Maximum Adsorbent Capacity:** The adsorbent capacity in g-U/kg-ads is plotted for various locations around the globe. This dataset is derived from the global sea surface temperature dataset as well as the user inputs for reference adsorbent capacity and temperature.

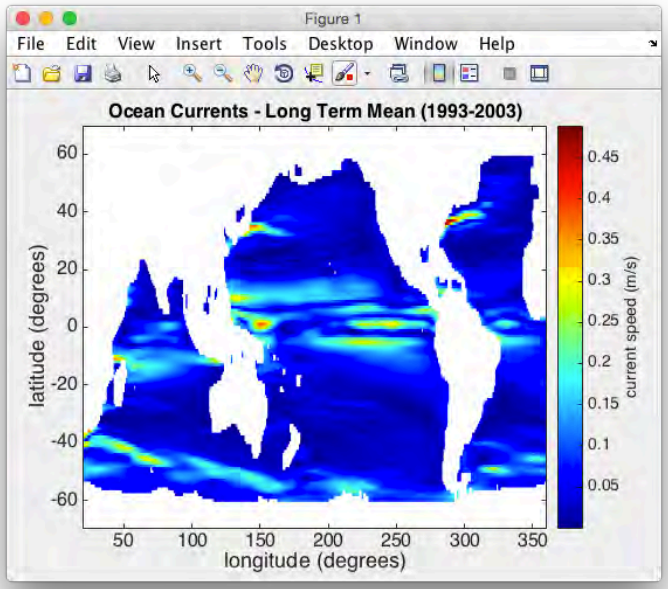

Figure 6.6: Typical ocean currents dataset plot.

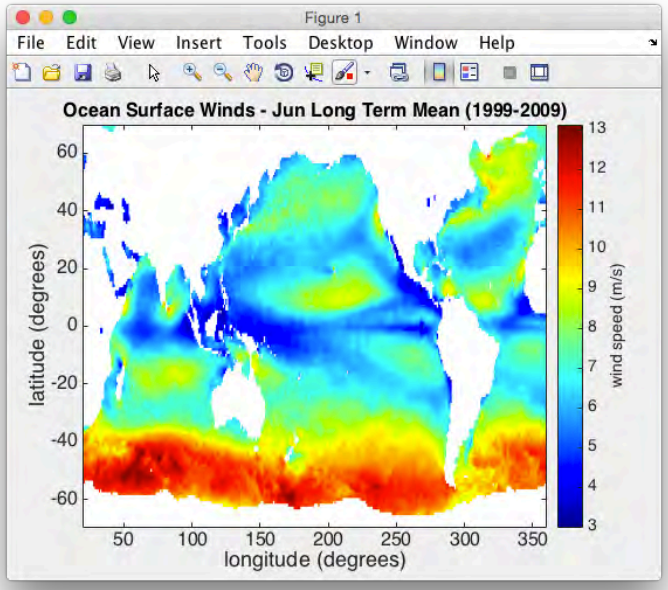

Figure 6.7: Typical ocean surface winds dataset plot.

Step 4: Suitability Index

The values entered in Step 1 are used here in Step 4 to determine the Suitability Index of various locations around the globe for harvesting uranium from seawater.

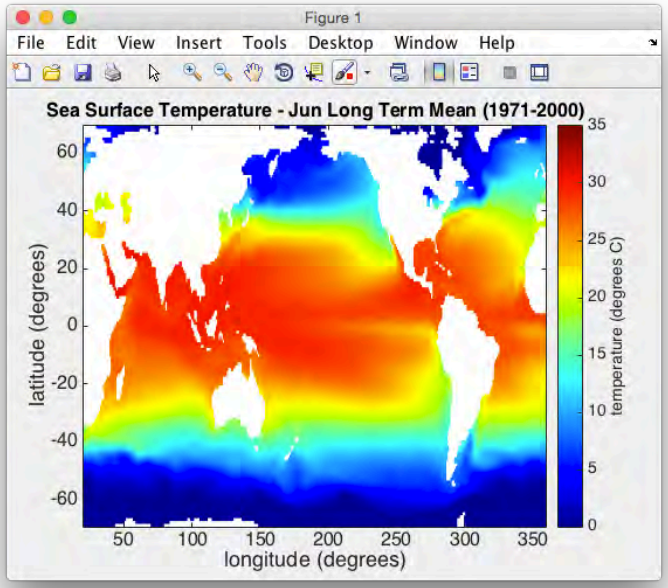

Figure 6.8: Typical ocean sea surface temperature plot.

The details of the calculation are described in section 6.3. The Suitability Index indicates how a potential uranium harvesting site compares to the region off the coast of Southern Japan, a location where many previous studies regarding seawater uranium harvesting were conducted (Seko et al., 2003; Sugo et al., 2001; Tamada et al., 2006; Tamada, 2009).

Pressing the "compute and plot suitability index" button will populate the axes below with the Suitability Index values of sites around the world. An index of 1 indicates that the location is similar to the region offshore of Southern Japan. An index less than 1 corresponds to a location that is not as suitable for seawater uranium harvesting as the region off the coast of Southern Japan, and an index greater than 1 signifies that the area is more suitable. The suitability of a location is determined by the adsorbent capacity as well as the power of the wind turbine due to ocean winds at that location.

Figure 6.9 shows a screenshot of the typical output from the SUSHI tool. The tools in the upper left corner of the SUSHI GUI (see figure 6.5) allow the user to zoom in, out, and pan to move through the resulting image.

6.5.1 Data output

In addition to the Suitability Index plot, the SUSHI tool also provides the option to export the resulting suitability index data for further analysis. To do this, the user must define a filename in the "output_suitability_index_file" box and then click "save suitability index data." If no filename is given, the file will be saved as:

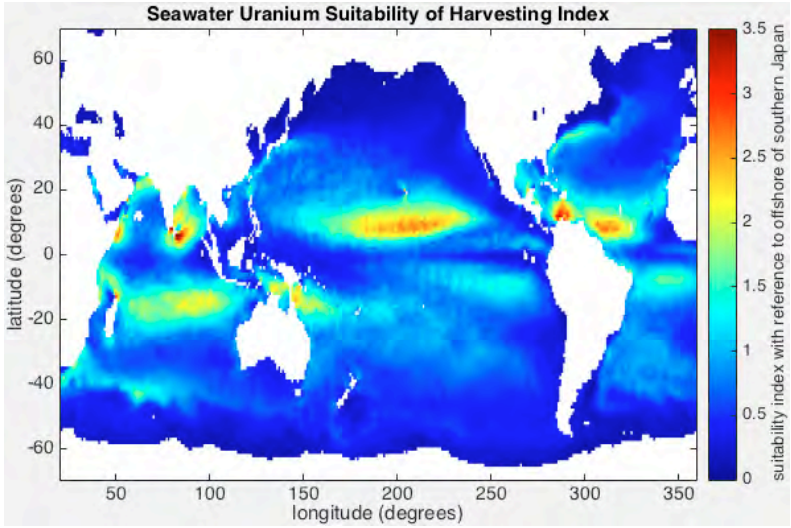

Figure 6.9: Typical suitability index plot.

"SI-month$\#_M$_t$\#_T$_h$\#_H$_v$\#_{V_1}$–$\#_{V_2}$.mat"

where

- $\#_M$ corresponds to the month value
- $\#_T$ is the campaign length (days)
- $\#_H$ is the wind turbine height
- $\#_{V_1}$ is the minimum wind turbine operation speed
- $\#_{V_2}$ is the maximum wind turbine operation speed

The output data file contains the following variables:

- 'lon': an array of the longitude at which the index is defined
- 'lat': an array of the latitude at which the index is defined
- 's_index': a matrix of the Suitability Index at each of the locations defined

6.5.2 Reminders: DOs and DONTs

In order to properly utilize the SUSHI tool, here are some things to consider.

- The month value must be between 1 (corresponding to January) and 12 (corresponding to December), or "all" for an average over all months.
- The wind turbine height must be in meters, m.
- The wind turbine operation speeds must be in m/s.
- The maximum wind turbine operation speed cannot be less than the minimum wind turbine operation speed.
- The reference adsorbent temperature must be in °C.
- The degradation per cycle must be in percent (i.e. 5% degradation must be inputted as "5".

6.5.3 An example

Presented here is an example of how to use the GUI for a test-case study. For this study, the following inputs were utilized:

- Month: 6
- Wind turbine height: 90m
- Wind turbine operation speeds: min = 3.5 m/s, max = 25 m/s
- Reference adsorbent temperature: 20°C
- Campaign length: 30 days
- Number of uses: 12
- Degradation per cycle: 5%

These are also the default values used by the tool in the event that the user does not provide any inputs.

Figure 6.10 shows a screenshot of the GUI after this step.

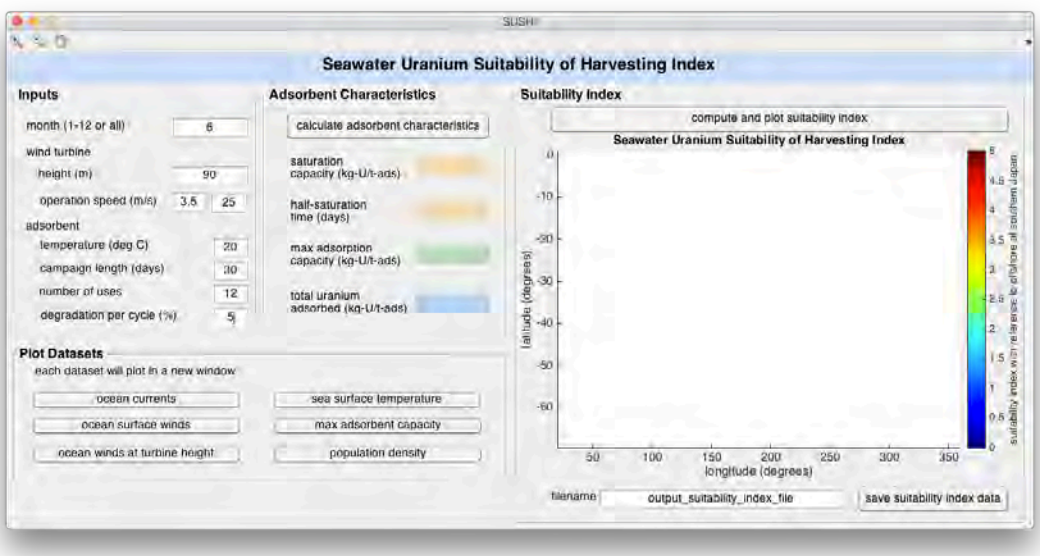

Figure 6.10: Screenshot of the GUI after the example inputs are entered.

Selecting any of the datasets will result in a new window in which they are displayed. For this example, "ocean winds at turbine height" and "maximum adsorbent capacity" are selected. Figure 6.11 shows a screenshot of the output plots for these selections.

Next, click "compute and plot suitability index" to visualize the suitability of various ocean sites for seawater uranium harvesting based on the previous inputs. Additionally, a name for the output file is selected to save the suitability index data. The GUI screen at this step is shown in figure 6.12.

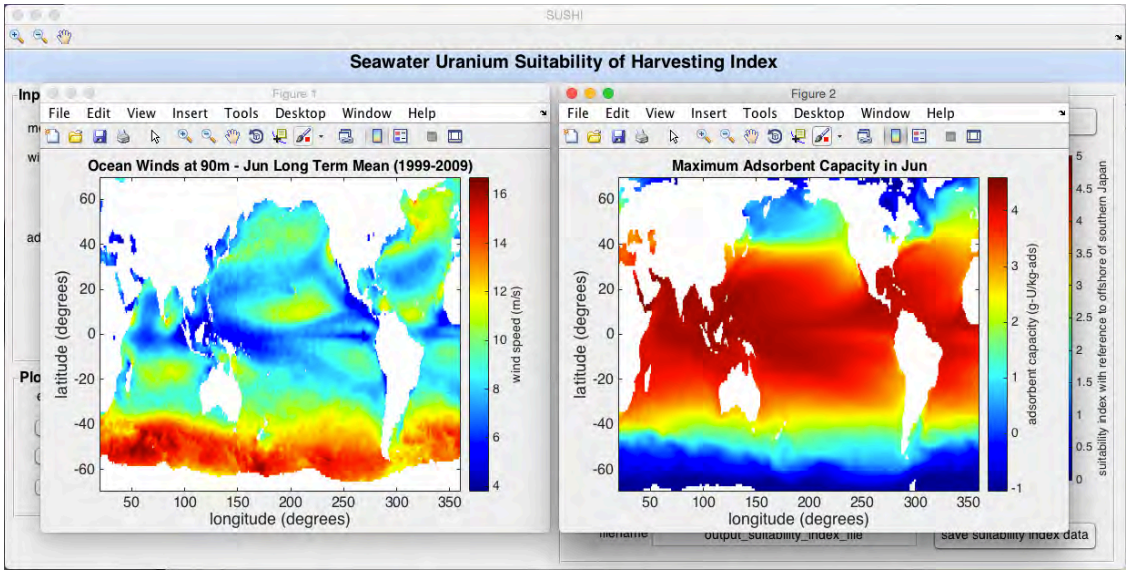

Figure 6.11: Screenshot of the GUI after selected datasets are plotted.

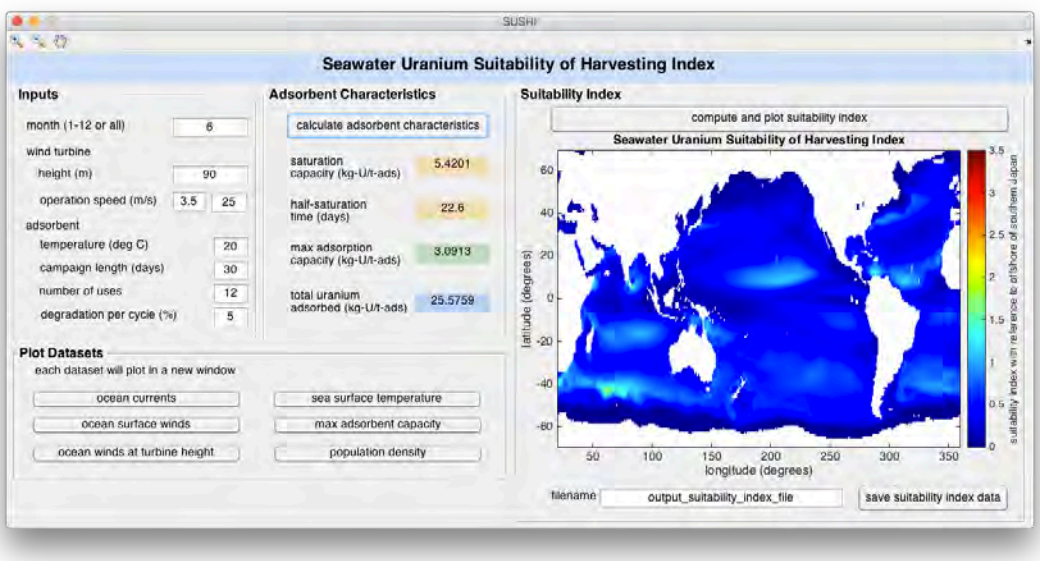

Figure 6.12: Screenshot of the GUI after selected datasets are plotted.

6.6 Future Work

At present, the Suitability Index only incorporates global wind and adsorbent capacity data as it relates to the feasibility of the colocation of uranium harvesters with floating offshore wind turbines. Future modifications to this system will include the competing effect on the adsorbent at increased temperature of biofouling reducing adsorbent uptake while temperature increasing it. The depth of the photic zone at regions

around the world could also be incorporated to determine the likelihood of biofouling at locations across the globe. Or a simple factor of 30% reduction in adsorbent uptake can be incorporated to account for biofouling.

Population density is currently not taken into account in this version of SUSHI, however could prove to be extremely important in the feasibility analysis of a symbiotic system to harvest uranium from seawater. For instance, while there are very strong winds in the middle of the ocean (which is very favorable for offshore wind development) the distance between these locations and any major population centers makes such deployments extremely costly and unreasonable. Hence, a factor to negatively weight regions based on their distance to population centers could remove these locations. This could also be incorporated by including ocean depth into SUSHI as ocean depth has shown to correlate with distance to shore.

Moreover, salinity is not considered in this model, although it has been shown to be a direct indicator of the amount of uranium present in the ocean (Owens et al., 2011). Incorporating global salinity data as well as any other global factors that affect the amount of uranium present in the ocean can greatly enhance the SUSHI tool to highlight regions with higher or exclude regions with lower uranium content.

Finally, the current SUSHI tool only considers the AF1 adsorbent. It should be expanded to include the possibility of all adsorbents developed by ORNL (i.e. AF1, 38H, AI8).

Adsorbent Shell Enclosures

This chapter describes a new shell enclosure strategy developed for use with the adsorbent fiber which allows for the decoupling the of material's functional requirements of strength and adsorption.

7.1 Motivation

In general, the amidoxime-based polymer adsorbents presented in the literature have inherently low tensile strength properties. For these reasons, the ligands are often grafted onto a polyethylene trunk fiber that can provide high tensile strength. Research has shown that while the tensile strength of the trunk ultra-high molecular weight polyethylene (UHMWPE) fiber may be more than 3.0 GPa, after γ-irradiation to induce grafting of the amidoxime ligands, this strength is decreased drastically to 1.3 GPa (Xing et al., 2013).

This decreased strength after irradiation is due to two factors. First, γ-irradiation causes the degradation of the UHMWPE molecular chain, thereby leading to a decrease in the molecular weight of polyethylene. Second, the radiation cross-linking of the UHMWPE fiber restricts the mobility of molecular chains of polyethylene, and causes nonuniformity of stress in the fiber (Yamanaka et al., 2006; Zhao et al., 2010).

Additionally, the decrease in strength after γ-irradiation was found to be dependent on the adsorbed dose. A higher radiation dose, the greater the impairment to the mechanical properties of the fibers which influences the lifetime and recyclability of the adsorbents (Hu et al., 2016). Thus, a method of decoupling the chemical and mechanical properties of the adsorbent polymer would allow for the independent optimization of both and likely lead to adsorbents with much higher adsorbent capacity.

7.2 Theory

A two-part system is developed to decouple the mechanical and chemical needs of an adsorbent for seawater harvesting of uranium. In the system, a hard permeable outer shell with sufficient mechanical strength and durability for use in an offshore environment and chemical resilience against elution treatments serves as the protective element for uranium adsorbent material with high adsorbent capacity in its interior.

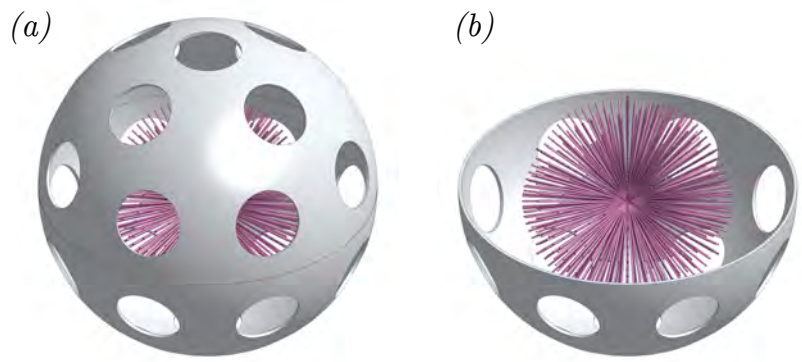

Figure 7.1: Initial adsorbent concept with decoupling of mechanical and chemical requirements. Soft, inner adsorbent sphere is encased in tough, outer protective sphere. Outer sphere features holes to allow adequate seawater to adsorbent interior.

The chemistry of the inner material can thus be optimized for higher adsorbent capacities, while the mechanical properties required of the system are achieved by the hard permeable outer structural shell, resulting in a system that is more cost effective for implementation.

Figure 7.1 depicts one shell design in which a spherical hard permeable outer shell encloses uranium adsorbing material inside. The uranium adsorbing material is wound into a ball with filaments extending radially outward from the center core (referred to as the filament ball). The holes in the outer shell are sized so that seawater may continually pass relatively easily to the interior of the shell where the uranium adsorbing material is housed, while maintaining sufficient mechanical strength to withstand the forces of the offshore system that must move the units through the water and collect and disperse them. The outer shell is preferably made of plastic, such as polyethylene, so that it can have high chemical resilience and therefore can withstand multiple elution cycles as required by the offshore seawater uranium harvesting system. By making the outer shell out of two distinct upper and lower hemispheres, it can be disassembled and reassembled for the easily placement and replacement of the inner uranium adsorbing material and can be reused many times for multiple changes of adsorbents.

7.3 Adsorbent Interior

The adsorbent interior is modeled by two main parts: (1) a filament core of diameter d_{fc}, and (2) a series of fibers of length l_f radiating outward from the spherical surface of the filament core. This is done because it is assumed that there is some critical

region in which the adsorbent fibers will be so tightly wound that the water will not be able to reach them and hence should not be considered when determining the uranium uptake of the filament ball. The overall shell diameter is given by d_s and the distance between the edge of a filament fiber and the edge of the enclosing shell is given by $d_{f,s}$. A schematic of this model is shown in figure 7.2.

The amount of adsorbent required by the system is determined by

$$m_{ads} = \frac{U_{req}}{\Gamma_n}, \tag{7.1}$$

where U_{req} is the amount of uranium to be harvested annually and Γ_n is determined by (5.11) for a specified number of elution cycles, n, and harvest time, t.

The length of the system, l_{sys} is defined to be the total length of all shells if they were placed to end to end such that the total number of shells is defined by

$$N_s = \frac{l_{sys}}{d_s}. \tag{7.2}$$

This is then used to determine the linear distribution of adsorbent as

$$l_{ads} = \frac{m_{ads}}{l_{sys}}. \tag{7.3}$$

The amount of adsorbent required to be in each shell is then determined by

$$m_{ads,s} = \frac{l_{ads}}{d_s}, \tag{7.4}$$

and the total length of fiber required per shell is

$$l_{req,shell} = \frac{m_{ads,s}}{\rho_f \pi \left(\frac{d_f}{2}\right)^2}, \tag{7.5}$$

where ρ_f is the density of the adsorbent fiber and d_f is the diameter of the adsorbent fiber (both properties taken from Gill et al. (2016)).

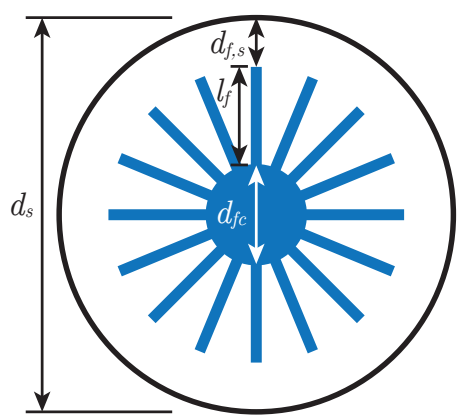

Figure 7.2: Schematic of filament ball of uranium adsorbing fibers and shell enclosure model.

Next, the adsorbent limit per shell is computed and compared to $l_{req,shell}$ to determine if a specific design is feasible. First, the diameter of the filament core, d_{fc} is set to be some fraction, γ, of the full shell diameter,

$$d_{fc} = \gamma d_s. \tag{7.6}$$

Then the surface area of the filament core, (i.e. the total area over which fibers are considered to be attached and emanating outward), is

$$s_{fc} = 4\pi \left(\frac{d_{fc}}{2}\right)^2. \tag{7.7}$$

The distance between the edge of a filament and the shell enclosure, $d_{f,s}$ is also selected to be some fraction, λ, of the full shell diameter,

$$d_{f,s} = \lambda d_s. \tag{7.8}$$

The length of the fiber is then

$$l_f = \frac{d_s}{2} - \frac{d_{fc}}{2} - d_{f,s}. \tag{7.9}$$

The cross-sectional area of the fiber can be determined from its diameter as

$$a_f = \pi \left(\frac{d_f}{2}\right)^2. \tag{7.10}$$

Then the effective area required per fiber for attachment to the filament core is given by

$$a_{f,e} = \frac{a_f}{\eta} \tag{7.11}$$

where η is the packing density of the fibers on the sphere. According to Conway and Sloane (1993), the close-packing of equal spheres has a maximum packing density of

$$\eta_{max} = \frac{\pi}{3\sqrt{2}} \approx 0.74048. \tag{7.12}$$

With this in mind, η is taken to be 0.70. The total number of adsorbent fibers that can be packed on the filament core is then

$$N_{f,c} = \frac{s_{fc}}{a_{e,f}} \tag{7.13}$$

and the total length of fibers in the shell is then

$$l_{shell} = N_{f,c} l_f. \tag{7.14}$$

If $l_{shell} < l_{req,shell}$, the design is considered feasible. Additionally, an efficiency factor, or an e-factor, can be determined for the design by

$$\text{e-factor} = \frac{l_{shell}}{l_{req,shell}}. \tag{7.15}$$

This factor determines how much extra adsorbent is being wound into each shell than is required. The closer to one, the more optimum of a design.

The feasibility of the uranium adsorbent material to be wound into a filament ball is detailed in figure 7.1. Lines 1-4 determine the amount of adsorbent required by the system, lines 5-9 calculate the adsorbent required per ball, lines 10-21 compute the limit of how much adsorbent can be incorporated in each ball, and line 22 indicates the feasibility of the overall design. Yellow boxes indicate adsorbent specific values, and green boxes indicate tunable parameters of the mechanical system. The offshore uranium harvesting system is designed with the requirement of harvesting enough uranium to power a 5-MW nuclear reactor annually, approximately 1.2 metric tons. The rationale behind this design decision is that, if the uranium harvester was paired with a 5-MW offshore wind turbine, the entire system could harvest twice as much energy per square meter of ocean. In this example, the AF1 adsorbent is considered, where properties of β_{max} and K_D were determined from the temperature dependencies described by Byers (2015). This combined with a temperature of T =20°C, a harvest time of t = 23 days, n =15 reuses, determines the amount of adsorbent required by the system in line 1. The density of the fiber and the adsorbent fiber diameter were taken from Gill et al. (2016). The results, with extremely conservative estimates of various mechanical parameters, prove the concept of an adsorbent filament ball to be mechanically feasible.

7.4 Shell Enclosure

Given the feasibility of an adsorbent filament ball, various shell enclosures were investigated for their structural strength and feasibility for use with the inner adsorbent filament ball. A strength comparison was performed of an dodecahedron, octahedron, and cube shell with circular holes in the center of each face. The geometry of the three shell types was adjusted so that they all had a maximum width of 0.5 m. All were submitted to a vertical distributed load of 3 kN as applied to the rim of the top face, with the bottom face full constrained. Each shell was assumed to be made of high density polyethylene (HDPE) which has yield stress of approximately 26 MPa. For each shell, the hole diameters were adjusted for each face so that the ratio of hole to solid area for each model was the same. Finally, the thickness of each structure was adjusted such that the mass of all three shells was the same. Figure 7.3 depicts the von Mises stress distribution for each of the three shells.

In addition to the von Mises stress, the factor of safety for each shell enclosure geometry was analyzed. The shell enclosure will start to fail if a new load is applied equal to the initial 3 kN load multiplied by the resulting factor of safety. The results of this analysis are shown in figure 7.4. As can be seen from the figure, the cube, with the smallest number of faces, has the highest factor of safety, whereas the more spherical-like shells, such as the dodecahedron, have a much lower factor of safety

Table 7.1: Feasibility calculations for adsorbent filament ball.

Line #	Offshore uranium harvesting system adsorbent requirement		
1	amount of adsorbent required (kg)	m_{ads}	45,431
2	length of system (m)	l_{sys}	6000
3	linear distribution of adsorbent (kg/m)	l_{ads}	7.57
4	total number of shells	N_s	12000
	Adsorbent required per shell		
5	density (kg/m^3)	ρ_f	950
6	adsorbent fiber diameter (m)	d_f	0.001
7	diameter of a outer shell (m)	d_s	0.5
8	absorbent per ball (kg)	$m_{ads,s}$	3.79
9	required length of fiber in ball (m)	$l_{req,shell}$	**5074**
	Adsorbent limit per shell		
10	filament ball core diameter to outer shell diameter (%)	γ	25
11	filament ball core diameter (m)	d_{fc}	0.125
12	distance between filament ball core and outer shell (m)		0.1875
13	surface area of filament ball core (m^2)	s_{fc}	0.049087
14	distance between end of fiber length and shell (%)	λ	12.5
15	distance between edge of filaments to outer shell (m)	$d_{f,s}$	0.0625
16	length of fiber (m)	l_f	0.1625
17	cross-sectional area of adsorbent fiber (m^2)	a_f	7.85E-07
18	packing density (%)	η	70
19	effective area required per fiber base for attachment (m^2)	$a_{f,e}$	1.12E-06
20	number of adsorbent fibers	$N_{f,c}$	43750
21	total length of adsorbent fibers (m)	l_{shell}	**5468.75**
	Design feasibility		
22	**feasible design? ($l_{shell} \leq l_{req,shell}$)**		**YES**
23	e-factor ($l_{shell}/l_{req,shell}$)		1.08

and the sphere shell enclosures exhibit the lowest factor of safety. Additionally, the factor of safety decreases nonlinearly as the number of faces increases.

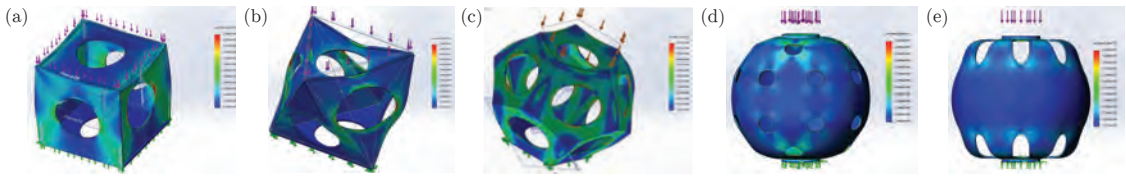

Figure 7.3: von Mises stress results for vertical loading of a (a) cube, (b) octahedron, (c) dodecahedron, (d) sphere with circular holes and (e) sphere with slotted holes shell enclosure.

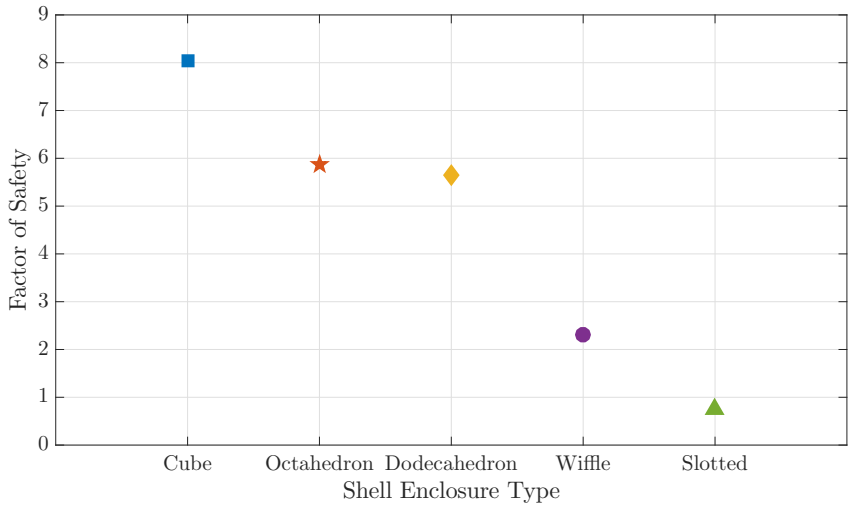

Figure 7.4: Factor of safety as a function of number of faces for the cube, octahedron, dodecahedron, sphere with circular holes and sphere with slotted holes shell enclosures.

In addition to the structure of the shell, the geometry of the holes in the shell may also be varied. The holes must be large enough so as to allow adequate seawater flow to the enclosed adsorbent without greatly affecting the structural strength of the shell. The effect of varying hole geometries on the overall strength of the shell was investigated for the cube shell enclosure, given that it had the highest factor of safety. A varied set of four hole geometries was implemented, depicted in figure 7.5. As in the case of varying shell structures, the factor of safety was determined for each of the four types of hole geometries on the cube shell enclosure, with the total hole area kept constant for each model: the results are shown in figure 7.6. As can be seen from the figure, the factor of safety for the standard rectangular slits (shown in figure 7.5d) was significantly lower than for the other hole geometries. In this model, both horizontal and vertical slits were used and failure was found to occur at the edge of the horizontal slits when under a vertical load. Replacing these horizontal slits by vertical slits resulted in a “Modified rectangular slits” hole geometry, which yielded the highest factor of safety of 29.

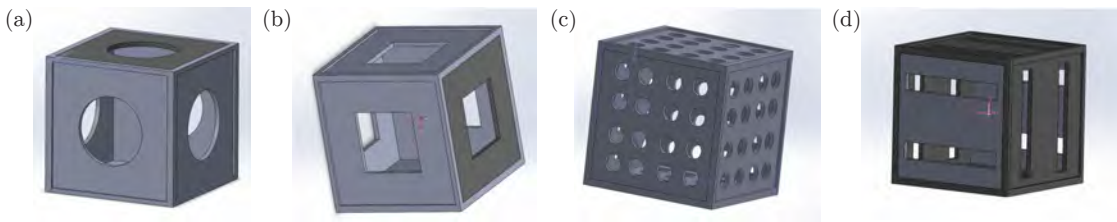

Figure 7.5: Solid models depicting cube shell enclosure with (a) large circular, (b) large square, (c) small circular, (d) rectangular slit hole geometries.

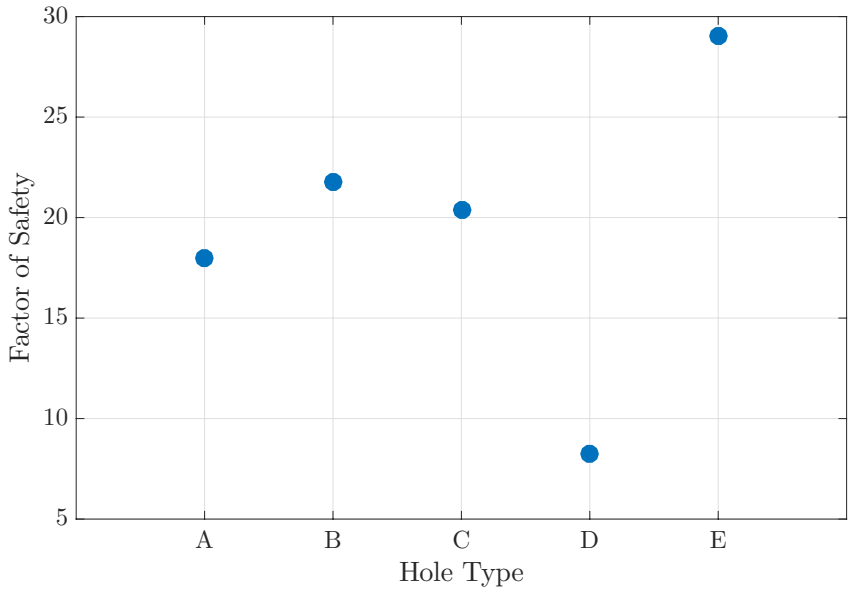

Figure 7.6: Factor of safety as a function of hole geometry for the cube shell enclosure. Hole types A-D are shown in figure 7.5 and hole type E is a rotated version of hole type D.

1/50th Scale Prototype

This chapter describes the design, building, and testing of a 1/50th physical scale prototype of a symbiotic uranium harvester system.

8.1 Functional Requirements

The functional requirements of the continuous seawater uranium harvester are as follows:

1. Use the amidoxime polyethylene braid adsorbent developed by ORNL known as AF1 (Janke et al. (2014b)).
2. The system should be able to recover 1.2 tonnes of uranium from seawater per year, 5-MW nuclear power plant.
3. Bring the cost of uranium extraction from seawater as close as possible to terrestrial uranium mining.

8.2 System Design Analysis

As discussed in the previous section, it is likely that the adsorbent with the best chemical properties for adsorbing uranium will not have enough durability and tensile strength for the designs previously studied by Picard et al. (2014), hence for this project we investigated designs for a symbiotic uranium harvester utilizing shell enclosures for the adsorbent. Many designs were studied and here the analysis for one type of system is presented. This system consists of connecting the adsorbent shells together using mooring rope into single or multiple loops resembling conventional ball-chain belts. These systems connect to a platform that is attached to an offshore wind turbine. In each system, the adsorbent ball-chain is cycled to the top of the platform at some point in time where the adsorbent is run through the required elution and regeneration baths.

Using the MISO algorithm (described previously) for the AF1 adsorbent it was found that the price of uranium would be minimized if the adsorbent was submerged for 23 days. In order to accommodate both this immersion time and the total time for elution and regeneration (a total time of 90 minutes), two designs for looping the ball-chain of adsorbent shell enclosures was investigated. In the first, the ball-chain

is looped circumferentially around the turbine, and in the second the ball-chain is looped under the platform in four separate systems by extending the platform and looping the ball-chain several times beneath it.

8.2.1 Circumference Looping System

The first design, shown in Figure 8.1 also utilizes a continuous chain of incrementally spaced adsorbent spheres connected in a loop. Where the original design consisted of several of these systems spaced around a platform, the circumference looping strategy uses only one system. The chain enters the water as it did in the original ball-chain system but instead of looping around at the bottom and returning to the surface immediately the chain approaches the surface of the water then loops around a gear again to return to the bottom of the system. The chain does this repeatedly, tracing the perimeter of the platform until it has completely circled the platform, at which point it returns to the surface and proceeds to move through the elution and regeneration tanks. By modifying the geometry of the platform and the depth of the system the length of the chain and therefore the chain speed can be modified to accommodate the elution and regeneration times.

Each time the chain loops it will require a gear as well as a shaft protruding from the turbine that would need to be the length of the platform. The number of shaft-gear pairs for the whole system can be calculated by dividing the circumference of the platform by the diameter of the gear and rounding down to the nearest odd integer. The longer the platform, the larger the number of shaft-gear pairs.

Modeling the platform as a square cantilever beam with the force due to the driving gear, elution and regeneration tanks, elution and regeneration chemicals, and

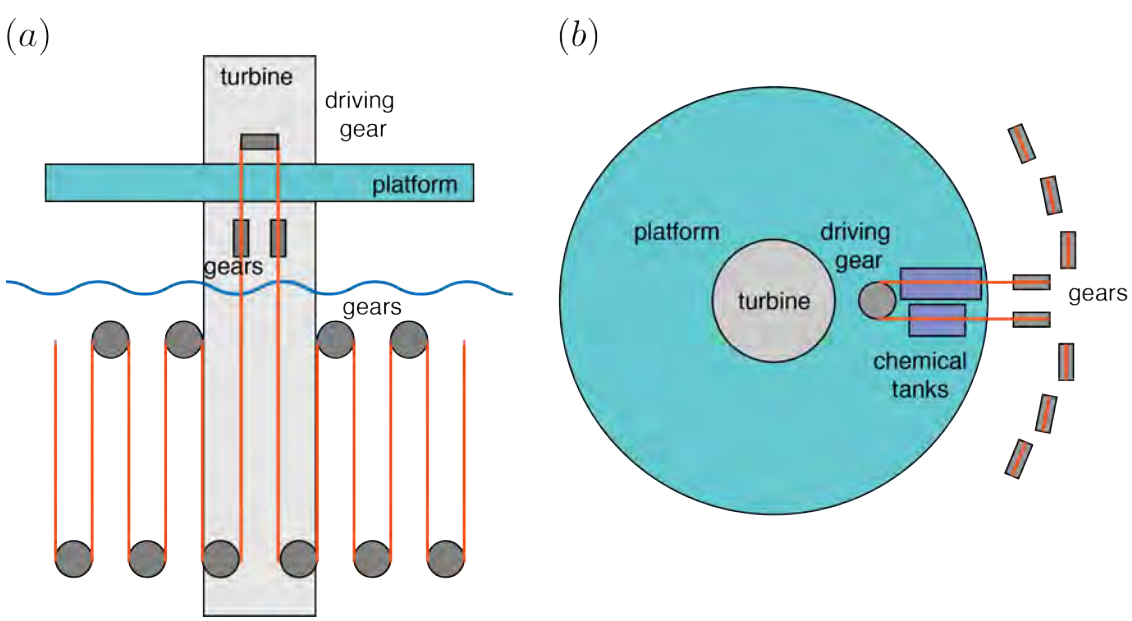

Figure 8.1: The (a) side and (b) top view of the circumference looping system.

storage tanks focused at the end, the thickness of the platform is given by

$$x_{th,pl} = \left(\frac{4F_{pl} l_{pl}^3}{\delta_{pl} E_{pl}} \right)^{1/4} \tag{8.1}$$

where F_{pl} is the net force on the platform due to the driving gear, elution and regeneration tanks, chemicals, and storage tanks,l_{pl} is the length of the platform (from the turbine), δ_{pl} is the maximum allowed deflection of the platform, E_{pl} is the Young's modulus of the platform's material, and $x_{th,pl}$ is the platform thickness.

Assuming the platform is made of steel, has a length of 16m, and a maximum allowed deflection of 1.6m at its end (10% of the length of the platform), the platform will need to be 0.431 m thick.

The large platform size and large number of shaft-gear pairs makes this impractical from a financial standpoint. Deploying such a system would also be problematic since the chain would need to be looped around so many gears. While a single system would require only one elution tank and one regeneration tank, because there is only one system its ability to harvest uranium could be compromised by a single failure.

8.2.2 Under-Platform Looping System

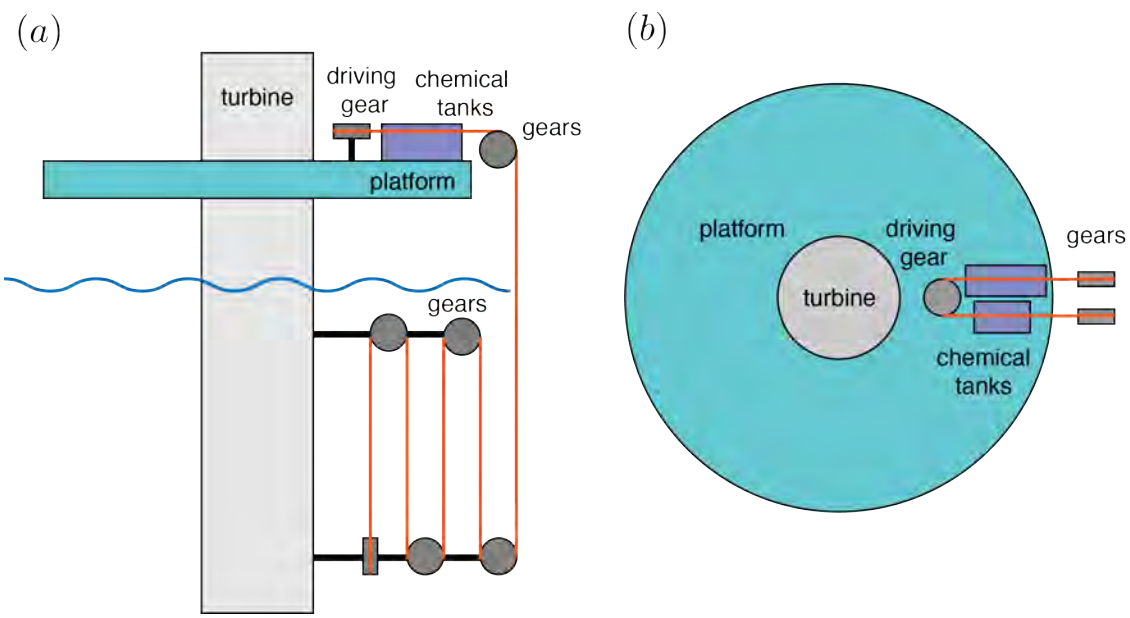

Figure 8.2: The (a) side and (b) top view of the under-platform looping system. Note, only one subsystem shown. In principle, multiple subsystems of driving gears and chemical tanks could be placed around the turbine.

The second strategy also utilizes a continuous chain of incrementally spaced adsorbent spheres connected in a loop, shown in Figure 8.2. Each system includes a chain and elution and regeneration tanks to process the adsorbent. Each turbine would have four such systems attached to it. In a similar manner to the circumference-looping

design, the under-platform looping design extends the length of chain by allowing it to loop several times beneath the surface of the water. Where the circumference-looping design repeatedly looped around the circumference of the platform, the under-platform looping design allows the chain to loop underneath the platform itself.

The number of times the chain can loop beneath the platform is based on the length of the platform. Each gear the chain loops around is parallel to the shaft it is attached to, except for the gear closest to the turbine. This gear is perpendicular and allows the two sets of loops (one on each side of the shaft) to connect, forming one continuous chain.

The number of subsystems on the turbine determines the platform length, by the equation

$$L_p = \frac{d_g + 2d_s}{2}\left(\frac{1}{\sin\left(\frac{\pi}{N}\right)} - 1\right) + d_g + L_t - r_t \tag{8.2}$$

where L_p is the platform length, d_g is the diameter of the driving gear, d_s is the shell diameter, N is the number of subsystems, L_t is the length of the chemical tanks, and r_t is the turbine radius at the platform.

By mounting the storage tanks directly onto the turbine underneath the platform, the shape of the platform can be modified to more closely accommodate the four systems. Equation (8.1) can be used to determine the thickness of each systems rectangular platform segment.

Assuming the platform is made of steel, has a length of 16 m, and a maximum allowed deflection of 1.6m at its end (10% of the length of the platform), each platform spoke (one for each system) will need to be 0.157 m thick. This design reduces the size of the platform as well as significantly reducing the required number of submerged shafts to two per system.

8.3 Prototype Development

8.3.1 Design Process

After multiple stages of analysis, we finally chose to build a prototype of the under-platform looping version of the Ball-Chain System. In order to proceed with the building aspect of the project, we had to first make a 3-D model of the full scale system to get a sense of what it would look like FIGURE. Taking each part of the system separately, an inventory of the materials follows:

1. **Turbine:** The turbine is modeled by two pieces of PVC of 7 inches and 5 inches in diameter respectively, accounting for the shape of the full scale turbine; a reducer coupling to connect the two pieces of PVC together and an end cap to make the system watertight in order for it to be able to float just like the full scale system.

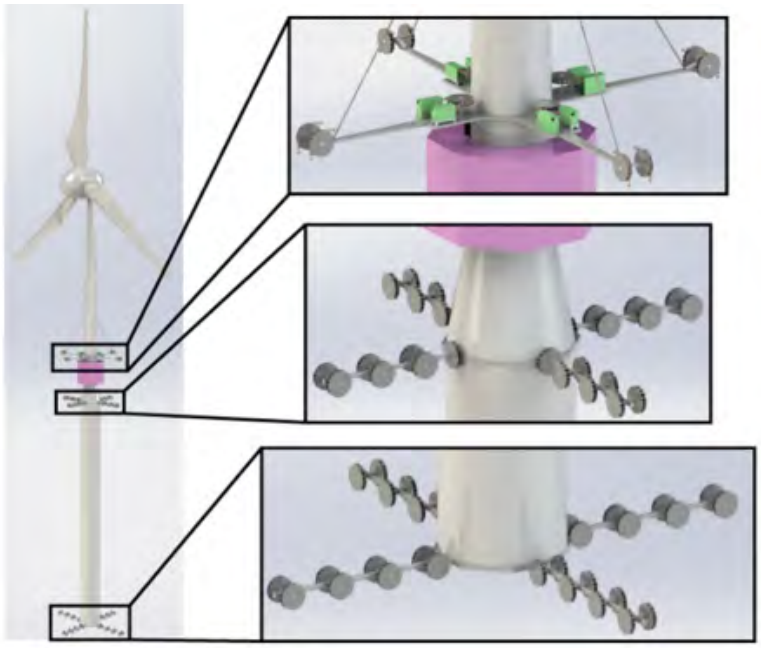

Figure 8.3: Three-dimensional view of under-platform looping system for uranium recovery using adsorbent shell enclosures looped around the turbine mast.

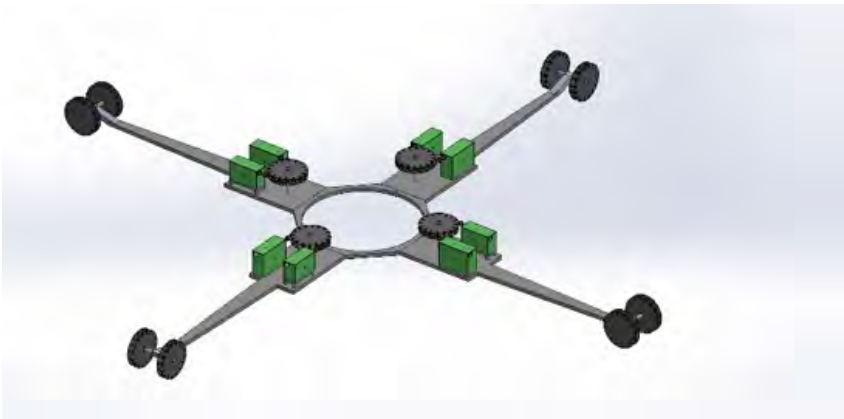

Figure 8.4: Three-dimensional view of platform for under-platform looping system.

2. **Platform:** During the process of making the 3-D model, the shape of the platform underwent many modifications in order to efficiently use the available space and reduce the amount of materials to use, which is aluminum in this case (Figure 8.4). The platform was cut using an OMAX Abrasive Waterjet.

3. **Elution and Regeneration Tanks:** The elution and regeneration tanks were modeled by rectangular boxes of appropriate sizes made out of acrylic.

4. **Gears:** A total of 72 gears of about 1.5 inches in diameter and 1/4 inch thick were needed for the prototype and they were all made out of acrylic (Figure

Figure 8.5: 1/50th physical scale acrylic gear

8.5). The diameter of the gear was determined using:

$$d_g = \frac{2}{\pi}\left(N_s d_s + L_s N_s\right) \tag{8.3}$$

where
d_g = gear diameter
N_s = number of shells per 1/2 gear
L_s = spacing between shells
d_s = shell diameter

5. **Shafts:** All of the shafts of the prototype were modeled by aluminum rods of the appropriate sizes.

6. **Ball-Chain:** With the 1/50th scale prototype, simulating the ball-chain proved to be a challenge because, when reduced to the prototype scale, the diameter of the balls was only about 0.2 inches in diameter. As a result, we ordered plastic bead chain with beads as close as possible to the required size.

7. **Power System:** Due to the big difference between the amount of time that the polymer needs to spend in water and the elution/regeneration time, the required chain speed for the full scale system turned out to be 0.00039 m/s calculated using:

$$s_c = \frac{l_{et}}{t_{et}} \tag{8.4}$$

where

s_c = chain speed in m/s
l_{et} = length of path of submerged shells in elution tank
t_{et} = elution time (60 minutes for AF1 adsorbent)

Therefore, the 1/50th scale prototype needed a motor with small rpm. We picked the motor with the smallest rpm which fit our system perfectly even though it still had a higher rpm than we needed. The final 1/50th physical scale prototype is show in Figure 8.6.

8.3.2 Testing

Once built, the system was tested in the Massachusetts Institute of Technology (MIT) swimming pool in the Alumni Pool and Wang Fitness Center. Figures 8.7 and 8.8 show the upper platform and upper gear shafts of the prototype in the pool, respectively. During the test, we encountered 2 major issues: Once put in water, the PVC was difficult to stabilize even with the 25 lbs sandbags attached to it. In order to get some stability, we had to let water inside the PVC until it becomes stable enough to be maneuvered easily.

Another issue was the tension in the chain. Because of the number of loops in the system and the depth of the system. There was too much of a distance to be covered by the chain for it stay tensioned throughout the process and we had to leave it at that for the moment. However, a new solution was proposed to tackle this problem and it consists of keeping the upper and lower shafts close together, put the chain around the gears and tension it as we pull one shaft away from the other. Proving that this proposition works and that the chain can be tensioned efficiently, will be an important step towards improving this concept.

8.4 Cost analysis

The cost analysis for the full-scale version of the system prototyped was done in collaboration with UT Austin (Dr. Erich Schneider and Maggie Flicker Byers). The production cost of uranium from seawater was calculated using discounted cash flow techniques to follow the life-cycle costs a unit mass of adsorbent accrues throughout its lifetime as was done in previous cost analyses (Schneider and Sachde, 2013; Byers and Schneider, 2016a) . All costs are presented in 2015 dollars.

8.4.1 Reference Deployment Case

The reference deployment scheme refers to the kelp-field like structure described in the initial proposal of the passive recovery system (Tamada et al., 2006) that was later slightly modified for economic improvements (Schneider and Linder, 2014). This system uses a polymer rope interlaced with metal chains to both hold rows of adsorbent together and moor the net buoyant braids to the ocean floor. Upon realization of

Figure 8.6: 1/50th scale prototype.

the soaking campaign work boats equipped with windlasses winch up the adsorbent braids. Rather than traveling all the way back to shore, the braids are transferred to a mothership for elution of uranium. Work boats then carry the adsorbents back to the field for another deployment. The adsorbents can be reused as many times as is economically feasible, dependent upon the degradation they suffer with each deployment and elution cycle.

Given the constantly evolving nature of recovery technology, there exists some

degree of uncertainty in adsorbent performance characteristics when placed in true marine conditions. Therefore, it is most appropriate to consider the uranium production cost as a range rather than a single point. Two particularly important parameters that characterize the best and worst case cost scenarios are: rate of adsorbent

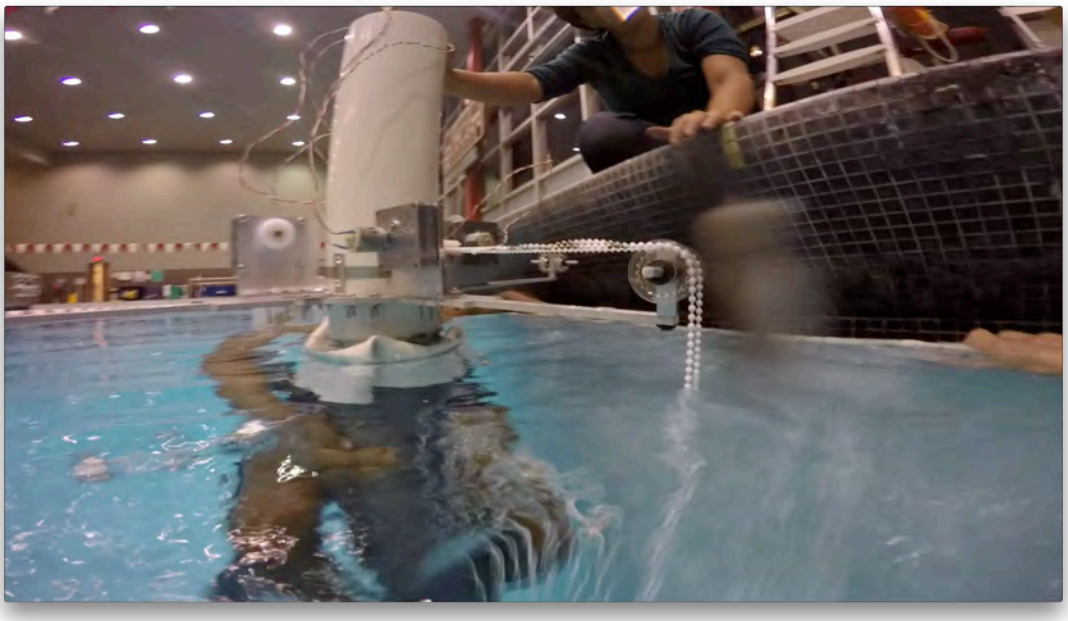

Figure 8.7: 1/50th scale prototype upper platform during pool testing.

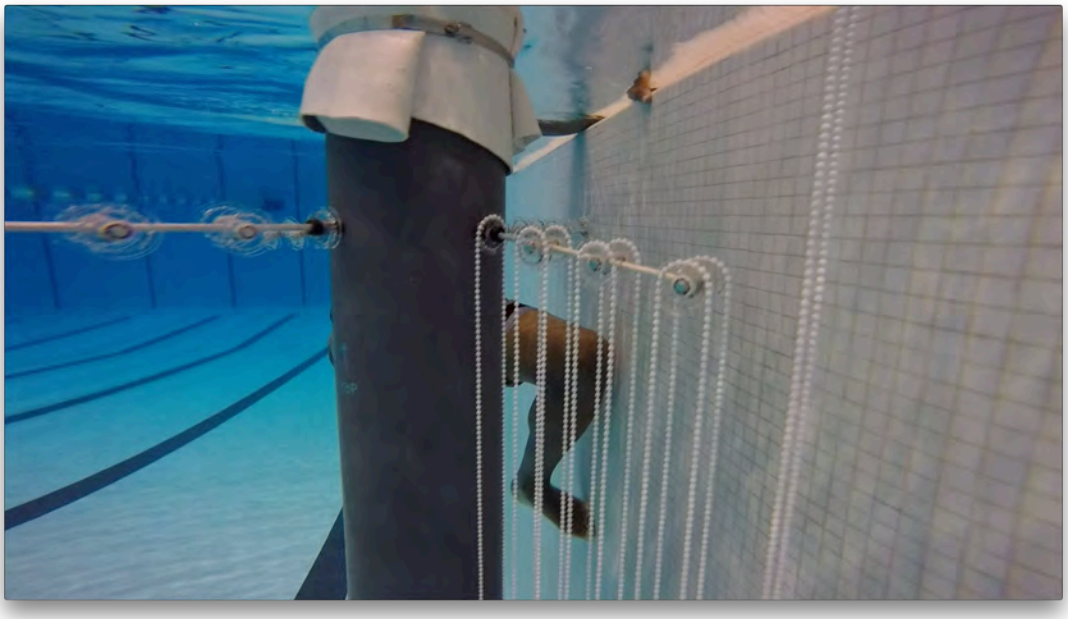

Figure 8.8: 1/50th scale prototype upper gear shafts during pool testing.

degradation and marine biofouling.

Recent experimentation by Pacific Northwest National Lab (PNNL) indicates that exposure to marine microorganisms that colonize the adsorbent surface can lead to a 30% loss in uptake (Park et al., 2016). Given the bright warm laboratory conditions at which these experiments were carried out, this is believed to serve as the maximum decrease in uptake that would be suffered as a result of oceanic biofouling. The lower bound is derived from the notion that it would be possible to completely mitigate biofouling to fully restore adsorbent performance. Therefore, a range of 0-30% loss in uptake is used to enclose the range of possible production costs.

The worst case scenario regarding adsorbent degradation upon reuse similarly comes from recent PNNL experimentation (Kuo et al., 2015). These experiments indicated that degradation is a function of length of campaign and was more severe on the first reuse as compared to all subsequent reuses. This contrasts to previous experiments (Sugo et al., 2001) on similar amidoxime adsorbents that experienced a constant 5% loss in uptake, independent of length of campaign or adsorbent re-use number. Therefore these two empirically derived models will serve as the upper and lower bound of degradation rates respectively.

These uncertainties give rise to the range of uranium production costs believed to represent the best and worst case scenario, for the current technology. Both performance scenarios were subjected to an optimization algorithm Schneider and Sachde (2013) used to find the deployment parameters, specifically length of campaign and number of adsorbent uses, that give rise to the minimum possible recovery cost. The resulting range for this reference kelp-field deployment scheme is $450-890/kg U, achieved with a 45 day campaign length of and 13 adsorbent uses in the best case scenario and 15 days and 10 uses in the best case. This range will served as the baseline to which the current deployment scheme was be compared.

8.4.2 WUSABI-Koosh Deployment

In order to differentiate the under platform looping system that was designed and prototyped from previous symbiotic deployments named Wind and Uranium from Seawater Acquisition symBiotic Infrastructure (WUSABI) (Byers et al., 2016), for the remainder of this text the under platform looping system will be referred to as the WUSABI-Koosh deployment for its of shell enclosures around adsorbent fibers that are woven into koosh-like balls.

The design as depicted by Haji et al. (2016) can be seen in Figure 8.9 with labels indicating the terminology of each part of the device used by this cost-analysis. The structure consists of a top spoke providing support to all of the tanks for adsorbent elution and the drive gears that move adsorbent through the system. The upper and lower shafts house the majority of the gears that provide tension for the ball-chain as well as constitute the under-platform loop paths that the chain follows. All support structures are made of 316 stainless steel. The speed of the ball-chain is calculated such that a unit mass of adsorbent will reach the elution tanks at the end of its soaking campaign so that it may be exposed to the elution chemicals for the necessary period before continuing to travel for another deployment cycle. The driving gear can be

tuned to speed up or slow down the ball-chain speed, resulting in a faster or slower immersion time of the adsorbent.

Here we provide a high fidelity cost analysis following the detailed methodology Schneider and Sachde (2013); Byers and Schneider (2016a); Byers et al. (2016) used on other recovery technology perturbations. Additionally, the evolving nature of the chemical technology requires updates to be made to important factors including adsorbent performance and the elution procedure itself. These changes were implemented by modeling the most recent adsorbent behavior and recalculating the tank number and volume required by the currently referenced elution method as described in Pan et al. (2014); Byers and Schneider (2015).

Mirroring the methodology set forth by Picard et al. (2014) the capital cost of the WSUABI-Koosh structure was calculated primarily by the raw materials required to construct the support systems. Each harvester unit was sized to support and process the mass of adsorbent required to recover 1,200 tonnes of uranium per year from the entire wind farm consisting of 214 turbines.

The adsorbent production cost remained mostly unchanged from previous economic analyses with the kelp-filed deployment scheme. There was however a required cost to wind the adsorbent into koosh balls, fabricate the shells, and to construct the overall int ball-chain lengths suitable for deployment with this system.

The method of calculating elution and purification costs also remains mostly unchanged from previous analyses. While the elution of uranium off the braids takes place at sea on the turbine, the necessary purification process was still assumed to

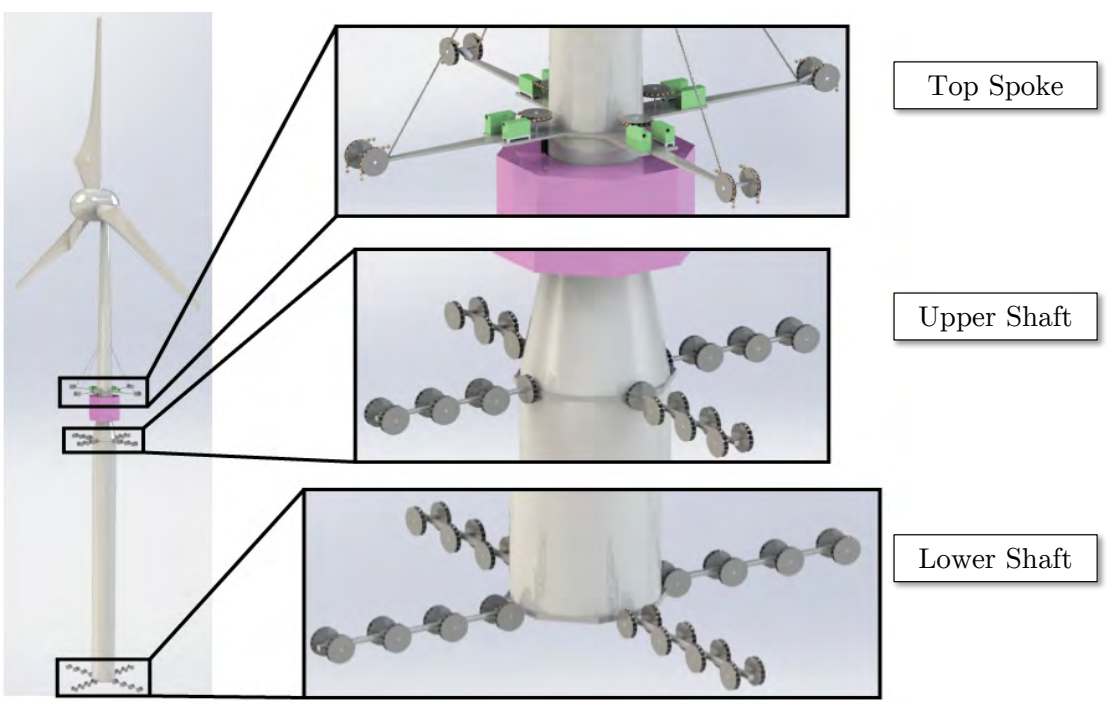

Figure 8.9: Depiction of WUSABI-Koosh design with labels indicating terminology used in the cost-analysis to refer to each part of the device.

take place on land. Therefore, the labor and facility costs for adsorbent elution are reduced. All costs incurred after the bicarbonate elution are calculated in the exact same way as in previous economic estimates Schneider and Sachde (2013); Byers and Schneider (2016a).

The same range of parameters applied to the reference kelp field deployment was used to calculate the resulting uranium production cost for the WUSABI-koosh scheme. Just as in the case of the baseline design, the cost calculation was subjected to an optimization procedure to find the best number of adsorbent uses and length of soaking campaign to minimize the production cost, $400-850/kg U. Savings of up to 11% can be realized by use of this deployment method.

8.4.3 Comparison of Deployment Schemes

The parameters for the ranges of best and worst case for each deployment scheme were define as:

Parameters	Range
Adsorbent Type	AF1
Biofouling (% loss in uptake)	0-30%
Degradation Rate (% loss per reuse)	Constant 5%-time dependent

Table 8.1: Parameters used in cost-analysis.

Figure 8.12 shows the cost range for the best and worst case scenarios of both deployment schemes as a function of number of adsorbent uses.

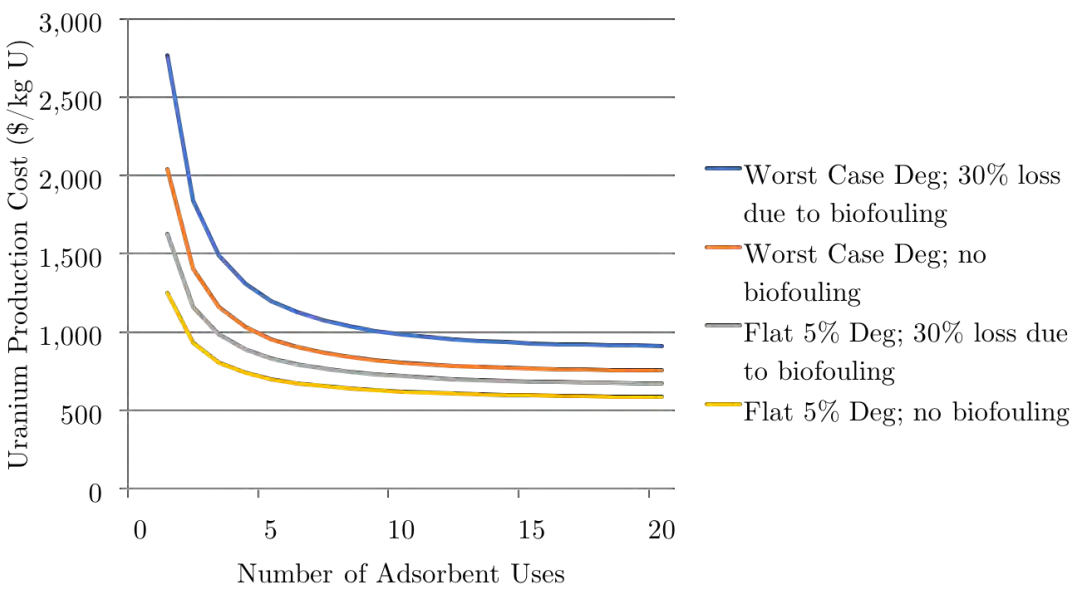

Figure 8.10: The best and worst case uranium production costs for the WUSABI-koosh schemes resulting from changing the parameters in Table 8.1

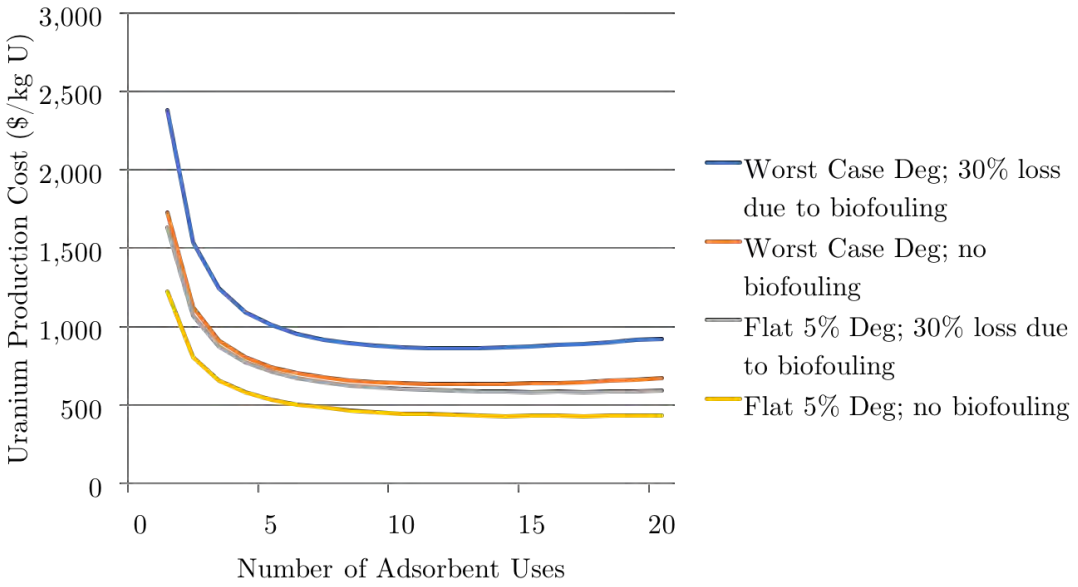

Figure 8.11: The best and worst case uranium production costs for the kelp-field schemes resulting from changing the parameters in Table 8.1

	Kelp-Field			WUSABI-Koosh		
	Cost ($/kg U)	Uses	Campaign	Cost ($/kg U)	Uses	Campaign
Worst Case	$870	10	15 days	$910	20	11 days
Best Case	$430	13	45 days	$590	20	74 days

Table 8.2: Optimized deployment parameters leading to the minimum achievable uranium production cost.

In both the best and worst case scenarios, the WUSABI-Koosh scheme resulted in a higher recovery cost, unlike the previous WUSABI scheme developed by Picard et al. (2014), as shown by a higher fidelity cost-analysis by Byers et al. (2016).

To investigate the cost breakdown further, we break down the costs into various categories, as seen in Figure 8.13. While the autonomous nature of this system results in significantly lower labor costs, which is responsible for the majority of the cost savings in the mooring operations and production operations categories, the mooring capital is significantly increased. Looking into this a bit further, as shown in Figure 8.14, we find that the gears contribute a significant portion of the cost, along with the necessary support shafts on the upper and lower spokes. Installation is taken to be a flat 40% of the delivered equipment cost.

8.5 Design Iteration

From the detailed cost-analysis, done in collaboration with UT Austin, it was found that the gears made up a majority of the system's cost. For this reason, further designs

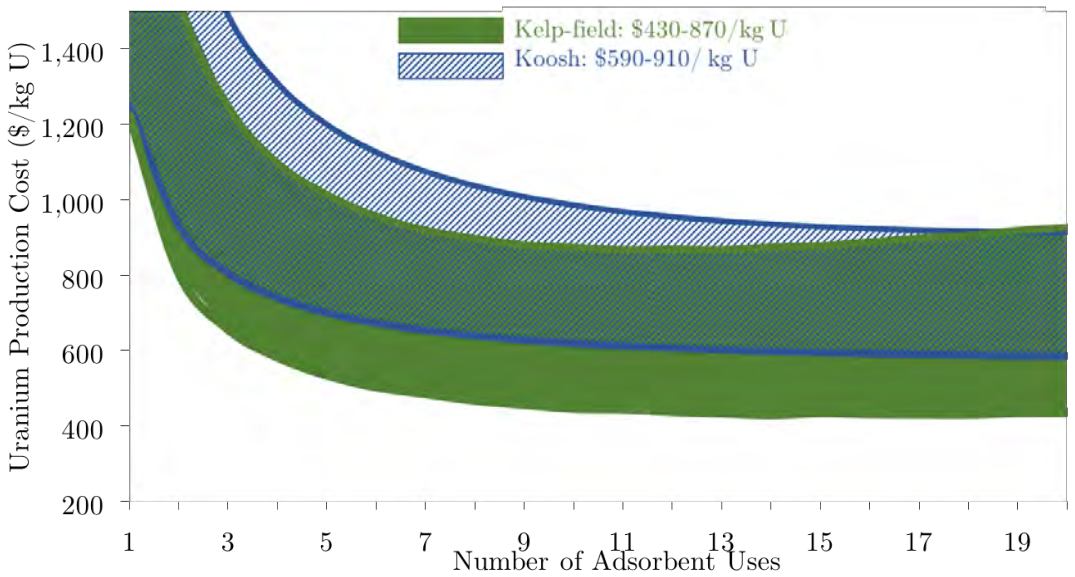

Figure 8.12: The range of costs for both deployment schemes as a function of number of adsorbent uses

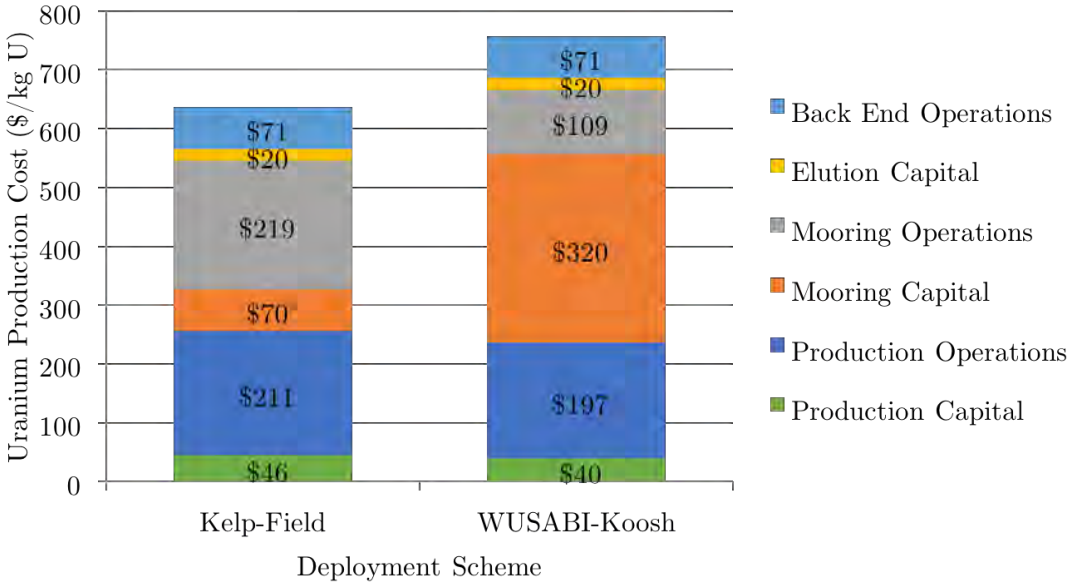

Figure 8.13: Total cost breakdown comparison between WUSABI-Koosh and reference kelp deployment schemes.

were investigated that would either use alternative gear materials, eliminate or reduce the number of gears, or decreased the density of the gear design. Additionally, reliance on tension in the ball-chain length is likely to be extremely difficult to generate or maintain in an open ocean setting and therefore, designs that do not rely on tension

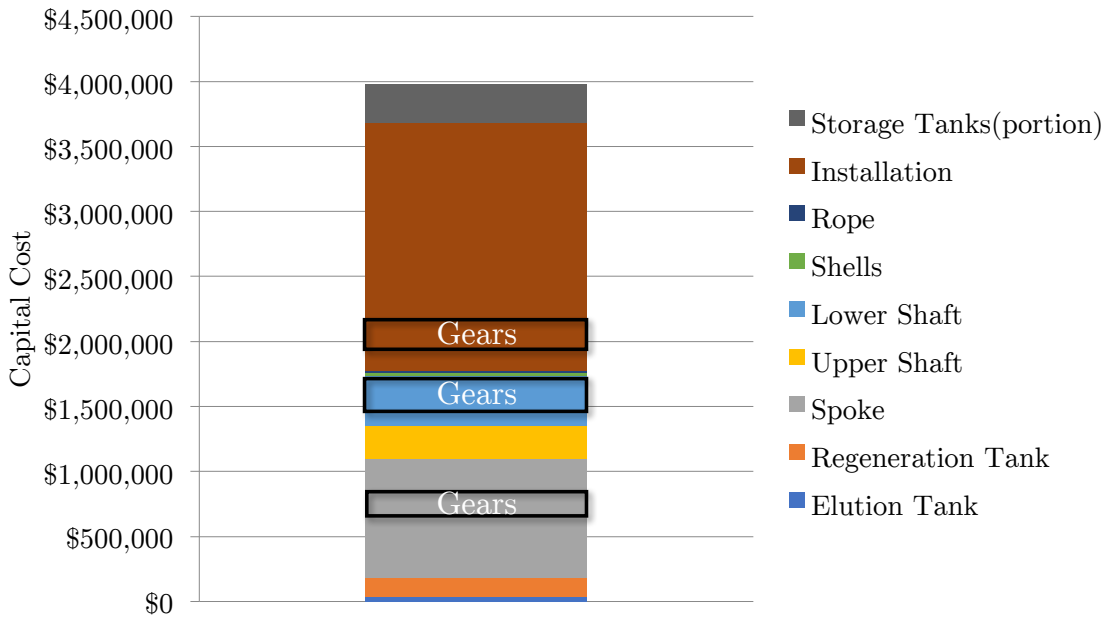

Figure 8.14: Cost components contributing to capital cost for the WUSABI-koosh system.

were investigated.

8.6 Conclusions

In this project, two modified versions to tackle the main issue of the original design were proposed: Circumference Looping version and Under Platform Looping version. The first version is about creating a single system with the chain looped around a platform instead of having multiple systems. The second version keeps the aspect of multiple systems but instead of a single loop in the ocean, the idea is to extend the platform and loop the chain several times underneath it.

A complete design and cost analysis of both versions was executed in order to determine both their physical and economic feasibility. The platform required by the Circumference Looping version was found to be too thick to be considered feasible. The under-platform looping version, on the other hand, was found to greatly reduce Mooring Capital and Operations. The cost of Uranium production with this version of the Ball-Chain System was estimated at $930.35/kg U. At first sight, this price does not compare favorably with existing terrestrial uranium mining systems ($80-335/kg U). However, further economic analysis of the system showed that the components of the system that drive its cost are the gears which were assumed to be made out of steel. This proved us that there is a lot of room for optimization and improvement.

As a result, the under-platform Looping version was selected for the construction of a 1/50th scale prototype which was tested in the Massachusetts Institute of Tech-

nology (MIT) swimming pool in the Alumni Pool and Wang Fitness Center. During the test, we realized that the system was too watertight which impaired the stability of the PVC pipe, but we assume that the turbine itself will be stable. Another issue arose with the tensioning of the chain but a new idea to solve this problem was proposed. Proving that the chain can be tensioned appropriately, and optimizing the choice of material are important steps as we move forward with this promising project.

Flume Testing of Shell Enclosures

This chapter describes the design and fabrication of an experiment to test the effect of the shell enclosures on the uptake of uranium adsorbents. This research was done in collaboration with Dr. Ken Buesseler and Jessica Drysdale at the Woods Hole Oceanographic Institution.

9.1 Method

Previous experiments have examined the effects of differing temperature, current speed, and degrees of biofouling on the adsorbent's ability to uptake uranium. For example, a previous study at the Pacific Northwest National Laboratory examined the effects of linear flow rates ranging from 0.48 cm/s to 5.52 cm/s on the adsorbent's ability to uptake uranium (Gill et al., 2015). No studies have examined the effects of a protective shell enclosure on the adsorbent's ability to uptake uranium.

9.1.1 Shell Enclosure Design and Fabrication

This experiments looks to investigate the affect of six shell enclosure designs on the uptake of uranium adsorbed by the fibers enclosed by the shells. One design was based on a classic wiffle ball with holes, which contained 24 holes positioned in four different tiers around the shell. Another design was based on a classic wiffle ball with slotted holes, containing eight slotted holes arranged in a circular pattern on each side of the shell. Figure 9.1 shows the six shell designs tested in this study in the order they were placed in the flume (with A being the closest to the inlet) as well as the naming convention used in the discussion. As you can see, enclosures A and B are the same design (the slotted wiffle), with the exception that they have different orientations to the flow. The same is true for enclosures C and E.

Shells were fabricated in two halves and included a series of tabs and corresponding slots that allowed the two halves to be aligned each time they are connected. Each half shell was 50 mm (1/10th physical scale of a full scale enclosure for ocean use) in diameter and 3D printed from white acrylic. Acrylic, unlike some other plastics, will not absorb water or deform after being submerged in seawater for extended periods of time. Unlike other colored acrylics, white acrylic does not contain any added dyes that could potentially leach into the seawater and affect the fibers in their uptake of uranium.

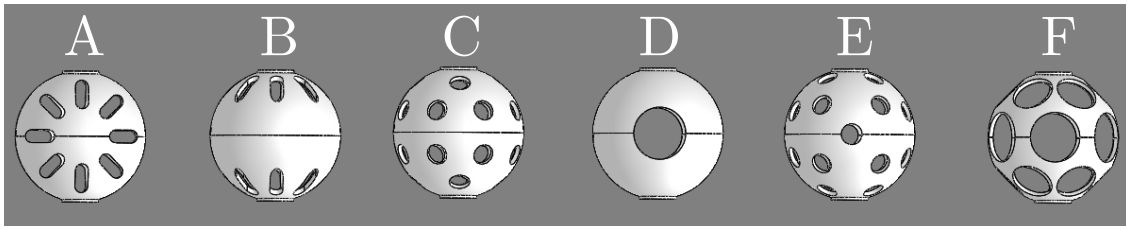

Figure 9.1: Solid models of six shell designs selected for testing.

Figure 9.2: Model of a protective shell enclosure. Each shell enclosure contained multiple tabs with corresponding slots to allow alignment of the two halves.

The enclosures were designed such that each shell half could be fitted to a piece of 1/4 in, threaded acetal rod and secured in place with two 1/4 in nylon nuts. These threaded rods were inserted into acetal blocks which were then glued to the base of a flume tank. The six shell designs were tested in a recirculating flume tank located at the Woods Hole Oceanographic Institution's Shore Lab. The tank allowed 0.45μm filtered seawater to pass through the shells continuously for 56 days.

The flume measured 72 in x 6 in x 12 in and was constructed using 0.5 in acrylic. The dark colored acrylic prevented light from passing through, thereby mitigating the effects of biofouling (Park et al. (2016)). Fresh filtered seawater, with temperature held at 20 $\pm 1.5°C$, was fed into the system from the head tank at flow-rates up to 1.5 L/min. As fresh seawater was pumped into the flume, a 9 in stand pipe near the recirculation outlet ensured the water level in the flume remained at a constant level. An inlet and outlet allowed the seawater within the flume to be recirculated at a constant flow rate. A diagram of the flume experiment is shown in figure 9.4.

A Finnish Thompson DB8 centrifugal, nonmetalic, pump recirculated seawater in the flume at a rate of 100 L/min, corresponding to a linear flow rate in the flume of 4.8 cm/s. The flow rate was regulated using a globe valve positioned after the pump's discharge port. The volumetric flow rate was continuously monitored using an Omega FP2010-RT flow meter in line between the recirculation outlet and the pump.

To ensure that no shell enclosures were in the wake of another, the six shell enclosures were staggered in their vertical placement in the flume. A seventh threaded rod and block was added to allow for an unenclosed piece of adsorbent that served as the control. A baffle, made of stacked 1/2 in PVC pipe segments and installed near

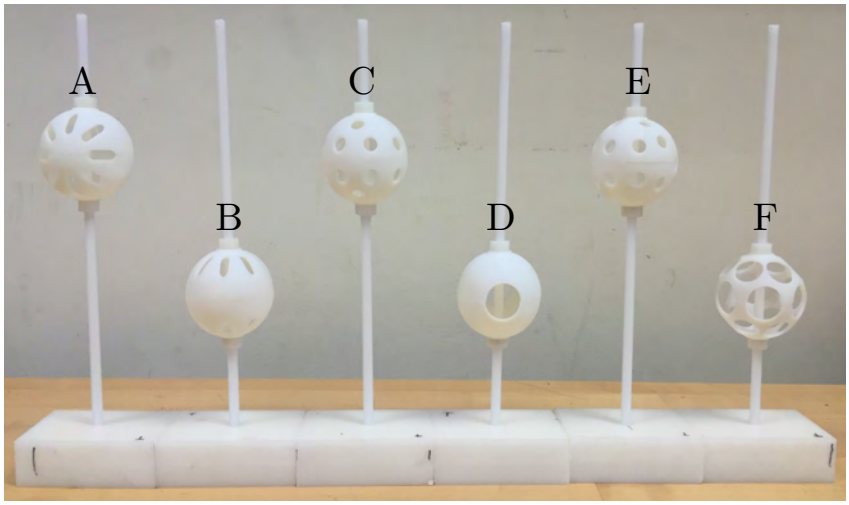

Figure 9.3: Six shell designs selected for testing. Each shell enclosure was fabricated in two halves. The upper half of each shell can be removed to allow for quick and easy sampling of the adsorbent. The outer diameter of all shell enclosures was 4 cm.

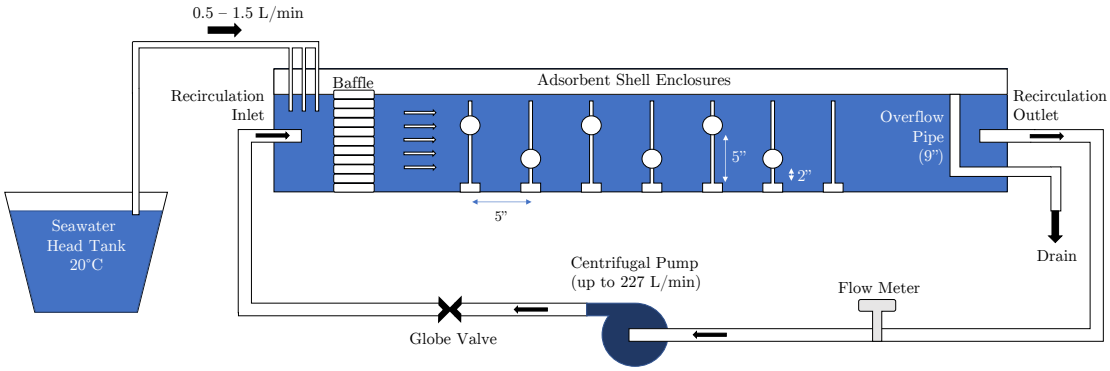

Figure 9.4: Diagram of the flume setup used to test the adsorbent enclosures. Fresh seawater is pumped in from a head tank using three tubes near the recirculation inlet. Overflow pipe ensures a constant water level of 9 in. A Finish Thompson DB8 Centrifugal Pump constantly recirculates the filtered seawater.

the recirculation inlet of the flume, minimized turbulence as the flow approached the shell enclosures.

A digital pressure meter was used to measure the pressure before the recirculation inlet and after the recirculation outlet to determine the pressure loss across the flume. The pressures were found to be 4.1 psi and 4.0 psi respectively, indicating a negligible pressure loss of 0.1 psi across the flume and confirming that the flow meter's measurement would not be affected by the pressure drop. The pump, flow meter, and all piping components were chosen such that all wetted components were made of plastic, thereby minimizing the possibility of contaminating the adsorbents with other metal ions.

Figure 9.5: Flume tank setup with flow meter, centrifugal pump, and globe valve connected.

Figure 9.6: All six shells positioned in the flume tank.

9.1.2 Design Analysis

In order to ensure dynamic similarity between the experiment and a full-scale scenario, Reynolds number scaling was used. For a shell of diameter d, the Reynolds number is given by

$$\mathrm{Re} = \frac{ud}{\nu}, \tag{9.1}$$

where u is the free stream velocity and ν is the kinematic viscosity. The kinematic viscosity of seawater at atmospheric pressure, salinity of 35 psu, and temperature of 20°C, is $\nu = 1.05 \times 10^{-6}$ m^2/s. For a full-scale shell of 500 mm in a flow of 10 cm/s (on the lower end of what is expected in an ocean setting), $\mathrm{Re}_{\text{full-scale}} = 4.76 \times 10^4$. For a 50 mm diameter shell being tested in the flume at 4.8 cm/s, the Reynolds number is $Re_{\text{model}} = 2.29 \times 10^3$. $\mathrm{Re}_{\text{full scale}} > 10^4$ indicates the flow is in the turbulent regime, whereas $Re_{model} < 10^4$ suggests the flow may not be turbulent in the flume.

To further ensure that the same physical phenomena were being witnessed in the flume as in the open ocean, the drag coefficient at various Reynolds numbers for the case of the standard wiffle ball (enclosure C) were further investigated. If the drag coefficient at $\mathrm{Re}_{\text{model}}$ was found to be similar to be $\mathrm{Re}_{\text{full scale}}$, it can be concluded that the shells in the model and at full scale would likely be seeing the same drag force due to the flow. This would suggest that the results of the flume experiment would be indicative of a full scale test in the ocean.

The drag coefficient and Reynolds number at linear flow rates ranging from 1.8 to 10 cm/s were calculated using FlowSimulation, CFD modeling software, for a shell 50 mm in diameter (1/10th physical scale) as well as a 500 mm diameter (full scale) shell. Additionally, a Tow Tank experiment was used to experimentally verify the drag coefficient, C_D, for a solid sphere and wiffle ball for a series of Reynold's numbers (Hamlet, 2017). As can be seen from figure 9.7, the experimentally determined C_D for the case of the wiffle ball enclosure (indicated by the green diamonds) ranges from 0.9-0.7, whereas the C_D determined from simulations of the wiffle ball enclosure (indicated by the red asterisks and yellow circles) range from 0.75-0.5. Although the experimentally and flow simulated drag coefficients of the wiffle ball do not agree exactly, they do exhibit the same trend: decreasing drag with increasing Reynold's number, which is indicative of turbulent flow. Additionally, in the experimental regime of the flume test (indicated by the black circle) the drag coefficient has decreased, suggesting the onset of turbulent flow. Thus, from these results it can be concluded that the forces seen on the shells in the flume test are likely indicative of those that would be seen by a full-scale shell in the ocean.

The shell locations within the flume were chosen to ensure shells would not lie in the boundary layer created by the walls of the flume or in the wake created by shells upstream. The free stream velocity is given by the volumetric flow rate divided by the cross sectional area of the flume:

$$u = \frac{Q}{w_f d_f} \tag{9.2}$$

where u is the free stream velocity, Q is the volumetric flow rate, w_f is the width of the flume and d_f is the depth of the water filling the flume. The flow regime at any point in the flume can be determined from the local Reynolds number, given by:

$$\mathrm{Re}(x) = \frac{ux}{\nu} \tag{9.3}$$

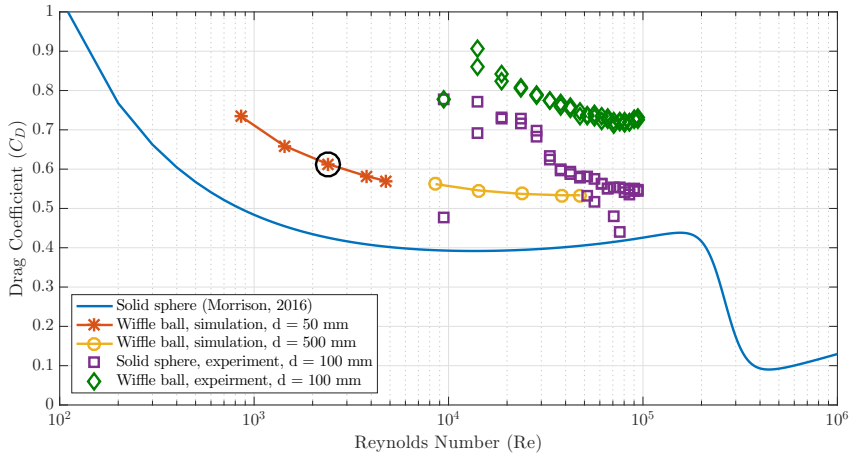

Figure 9.7: Drag coefficient as a function of the Reynolds number for a solid sphere as predicted by Morrison, 2016 (solid blue line), a wiffle shell with diameter 50 mm (red stars) and 500 mm (yellow circles) as determined from CFD simulations, as well as those determined by Tow Tank drag experiments for a solid sphere (purple squares) and a wiffle ball (green diamonds) of diameter 100 mm. The black circle indicates the experimental regime of the flume test described in this chapter. Tow Tank drag experiments were performed by Amanda Hamlet (Hamlet, 2017)

where $Re(x)$ is the local Reynolds number, u is the free stream velocity, x is the distance downstream from the boundary layer, and ν is the kinematic viscosity of seawater.

Since the fluid's velocity asymptotically approaches the free stream velocity, the thickness of the boundary layer is commonly taken as the point where the fluid velocity equals 99% of the free stream velocity. From (9.3), it was found that any free stream velocity greater than 0.92 cm/s resulted in a non-laminar flow regime within the flume, for which the boundary layer thickness is then given by:

$$\delta = \frac{0.382x}{\mathrm{Re}(x)^{1/5}} \tag{9.4}$$

where δ is the boundary layer thickness, x is the distance downstream from the start of the inlet, and $\mathrm{Re}(x)$ is the local Reynolds number.

With this information, for a flow rate of 4.8 cm/s and a shell spacing of 5 in, the boundary layer at the last shell would be approximately 1.77 in thick (on either side of the tank walls), meaning that the flow in a shell with a diameter greater than 2.45 in would be affected by the boundary layers. A shell with a diameter of 50 mm (1.97 in), as those used in this experiment, should not be affected by the boundary layer.

9.1.3 Adsorbent preparation, sampling, and analysis

Each shell contained a pre-weight, small mass of adsorbent fiber cut from a common AI8 adsorbent braid prepared by Oak Ridge National Laboratory Gill et al. (2016). Samples were collected after the first 24 hours and then again once per week for

eight weeks, for a total of nine samples over a 56-day test. Samples were taken by snipping small pieces ($\sim$ 35 mg) of the braid in each enclosure at these different time points. This allowed for the study of the adsorption kinetics of uranium and other trace elements. The adsorbent samples were analyzed at the Marine Sciences Lab at Pacific Northwest National Laboratory. In addition to adsorbent samples, salinity measurements were taken using a YSI Pro30 Conductivity Probe and water samples were also collected on each of the nine sample dates for trace metal analysis.

Figure 9.8: Photography showing the adsorbent in shells in the flume.

9.2 Results

Due to the conservative behavior of uranium in seawater, (Not et al., 2012) all uranium adsorption capacity data was normalized to a salinity of 35 psu in order to correct for the varying salinity of natural seawater observed in different adsorption experiments. Adsorption kinetics and saturation capacity were determined by fitting time-dependent measurements of adsorption capacity using a one-site ligand saturation model as described by (5.1). Figure 9.9 shows the time-dependent measurements of adsorption capacities for all trace metals retained by the AI8 adsorbent for each enclosure. As can be seen, uranium is not the dominant metal adsorbed by the fiber.

The uranium adsorption capacity (g-U/kg-adsorbent) for all adsorbents in all the enclosures is shown in figure 9.10, with the lines indicating the one-site ligand saturation model fits for each enclosure. The results from a flume study conducted in 2015 of the AI8 fiber alone are also included in the graphic. As can be seen, there is good agreement between the 2015 flume study and the study presented here. Furthermore, there is very little difference in the uranium adsorbed between the

different enclosure types. This suggests that the shell enclosure is likely not inhibiting the uranium adsorption of the fibers it encases, no matter the shell design.

The saturation capacity, β_{max}, and half saturation time, K_D, as well as the uptake predicted for an immersion time of 56 days as predicted from the one-site ligand modeling (equation (5.1)), is shown in figure 9.11. The error bars detail the $\pm$ 95% confidence intervals of the coefficients. As shown in the figure, there is little variability between the coefficients of the fits for each shell enclosure, suggesting no significant difference in the uranium uptake by the adsorbent in different shell enclosures.

This result is further seen in figure 9.12 which shows the total uranium adsorbed (g U/kg adsorbent) at day 56 for the adsorbent fibers in each of the different enclosures. Enclosure F resulted in the highest uranium uptake of 3.74 g U/kg adsorbent, whereas enclosure A saw the least amount at 3.23 g U/kg adsorbent, and the control with no enclosure saw an uptake of 3.54 g U/kg adsorbent. The difference in uranium adsorbed by enclosure F and A was only 13.5%, and the difference between the uranium adsorbed by any enclosure and the control adsorbent was at most 8%. This suggests, again, that there was no significant difference in the uranium adsorbed by fibers in the shells as compared to the control, and no significant difference between the uranium adsorbed between the different enclosure designs.

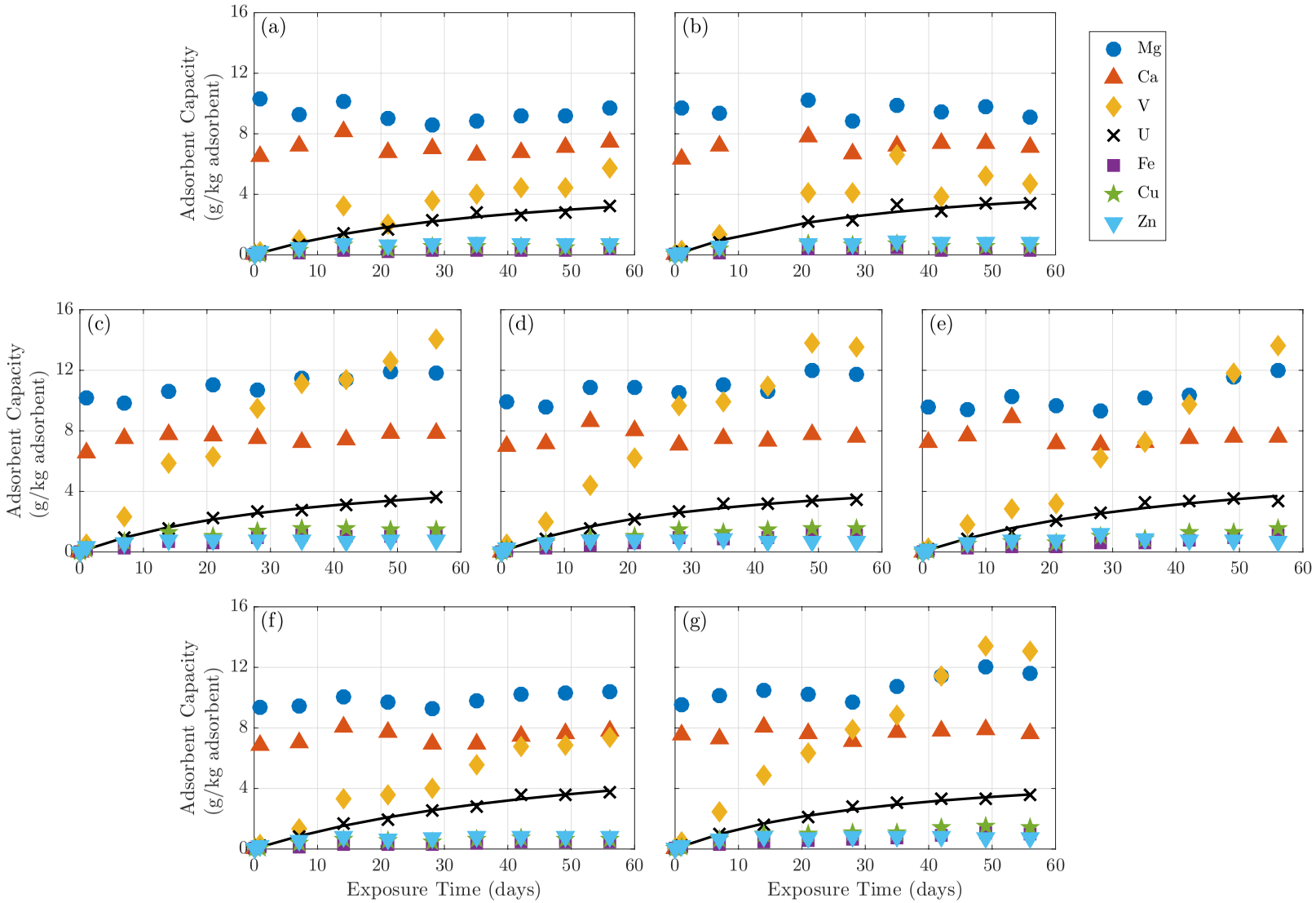

Figure 9.9: Time-dependent measurements of adsorption capacities (g element/kg adsorbent) for several trace elements retained by the ORNL AI8 adsorbent exposed to filtered natural seawater in a flume in various shell enclosures, (a)-(f) (as shown in figure 9.3), and without any enclosure, (g). The black line drawn through the uranium adsorption data represents fitting to a one-site ligand model (equation (5.1))

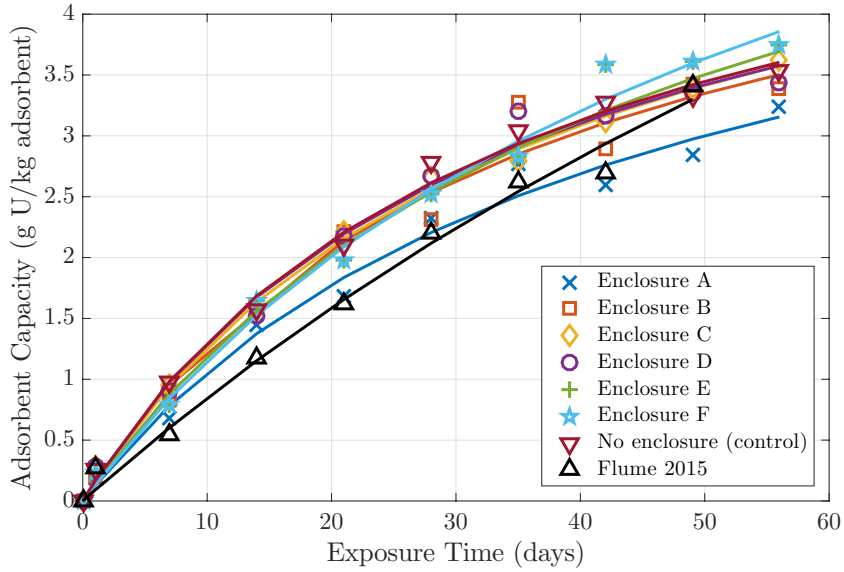

Figure 9.10: Time-dependent measurements of uranium adsorption capacity (g-U/kg-adsorbent) for the flume experiment for the seven AI8 adsorbent braids enclosed by various shell designs (Enclosures A-F), as well as the results from the control adsorbent in no enclosure and the results from a flume experiment conducted in 2015 on AI8 fibers alone. The uranium adsorption capacity was normalized to a salinity of 35 psu. Curves drawn through the data represent fitting to a one-site ligand model (equation(5.1)). Figure 9.11 details the saturation capacity and half-saturation times as predicted from the one-site ligand modeling

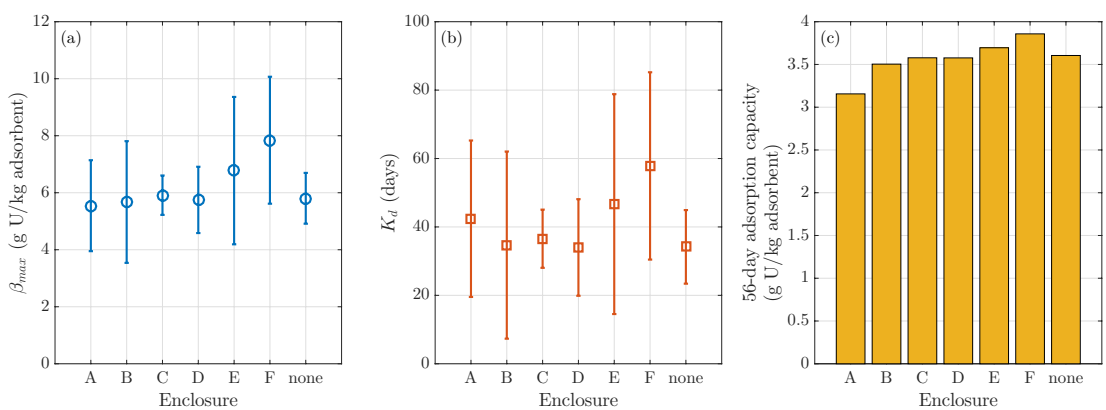

Figure 9.11: The (a) saturation capacity, β_{max}, (b) half saturation time, K_D, and (c) 56-day uranium uptake predicted by the one-site ligand model (equation (5.1))

9.3 Discussion

Results from this experiment will help inform the types of protective shell enclosures to be used in a large-scale ocean test of a uranium harvesting system. The flow rate of 4.8 cm/s used in this experiment, while chosen so as to reduce the boundary layer

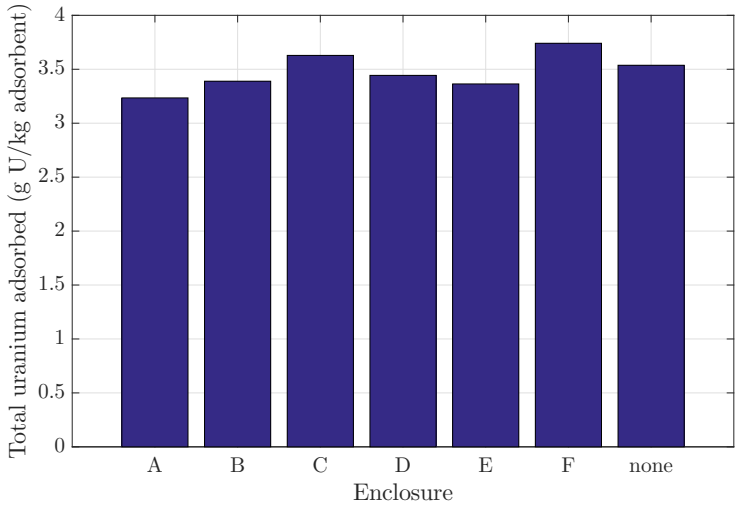

Figure 9.12: The total uranium adsorbed at day 56 by the adsorbent fibers in each enclosure from the flume experiment.

effects and ensure similarity between the forces on the shells in the flume as in the open ocean, is much lower than is expected in the ocean of eastern boundary currents, which can range from 10-30 cm/s. These are locations that have been hypothesized to be the best for the deployment of a uranium harvesting system in order to maximize the water flow seen by the adsorbent.

There was no difference in the amount of uranium adsorbed by the fibers in each of the shell enclosures, suggesting that the enclosures do not inhibit the uptake of uranium. It is highly unlikely that the flow field is the same inside each shell (a topic being investigated by Amanda Hamlet (Hamlet, 2017)). Thus, the lack of difference in uranium uptake between shells suggests that the linear velocity of the water is high enough that the reaction is no longer mass limited, as evidenced by Ladshaw et al. (2017) for similar linear velocities.

Additionally, experiments should investigate how the fiber may survive in such strong currents. Biofouling of adsorbent fibers can have an adverse effect on uranium uptake (Park et al., 2016), and future work should examine the effects of adsorbent shell enclosures on the biofouling of adsorbent fibers. Lastly, further structural analysis of protective shell enclosures used in this experiment should be conducted to determine the effects of distributed and point loads on different shell geometries.

Symbiotic Machine for Ocean uRanium Extraction (SMORE) Design

This chapter describes the design of the Symbiotic Machine for Ocean uRanium Extraction (SMORE) which was tested at a 1/10th scale. This chapter has also been detailed in milestone report: M3NU-14-MA-MIT-0601-016.

10.1 Functional Requirements

The functional requirements of a symbiotic device to harvest uranium from seawater are:

1. use the amidoxime-based polymeric adsorbent developed by Oak Ridge National Laboratory known as AI8 Gill et al. (2016);
2. recover 1.2 tonnes of uranium from seawater per year, enough annual fuel to power a 5-MW nuclear power plant annually; and
3. bring the cost of uranium extraction from seawater as close as possible to terrestrial uranium mining.

The uranium uptake for this system was predicted using the one-site ligand-saturation model:

$$y = \frac{\beta_{max} t}{K_D + t}, \tag{10.1}$$

where y is the amount of uranium adsorbed by g U/kg adsorbent, β_{max} is the saturation capacity in g U/kg adsorbent, K_D is the half-saturation time in days, and t is the immersion time in days.

Further analysis on the adsorbent behavior, recovery rate, and degradation, reveals that in order to achieve functional requirement (2), the sorption process can be optimized on the device using approximately 45 tonnes of adsorbent that is submerged in seawater for 23 days and cycled 15 times. While (10.1) is an idealized model not taking into account temperature, which has been found to have a large impact on the uptake of uranium, it allows for a starting point in determining the mechanical design of a potential system. In general, the immersion time and number of elution cycles, and hence total amount of adsorbent required, can be left as variables that propagate through the design tool, thereby allowing for the quick analysis of numerous designs.

10.2 Elution and Regeneration

Unlike previous designs developed by Picard et al. (2014) and Haji et al. (2016), which utilize on-site continuous acidic elution and bicarbonate regeneration processes, this design employs a single, 24-hour bicarbonate elution as described by Pan et al. (2017). Recent work has shown that the acidic elution process leads to degradation of the adsorbent with subsequent reuse, which may be mitigated or removed altogether by the replacement of acid by a potassium bicarbonate solution (Pan et al., 2017). Additionally, the adsorbent no longer needs to be regenerated with alkaline solution since a basic solution has replaced the previously used acids. The elimination of this step provides a significant cost savings through the reduction of chemical consumptions (Byers, 2015).

10.3 Mooring and Recovery

Uranium-adsorbing materials with the optimal chemical properties for high adsorbent capacity, in general, have inherently low tensile strength and durability. Hence, the designs previously studied by Picard et al. (2014), which require the adsorbent to be woven into a belt which is held in tension, are likely not feasible with the AF1 adsorbent, as it will probably not possess the necessary durability and tensile strength required. The design presented here utilizes the shell enclosure strategy in which the mechanical and chemical requirements of the system are decoupled. In these designs and the system presented in this chapter, the uranium adsorbent material with high adsorbent capacity is enclosed in a hard permeable outer shell with sufficient mechanical strength and durability for use in an offshore environment and chemical resilience against elution treatments.

10.4 Mechanical Design

Because offshore wind turbine data is proprietary and often very difficult to use for public work, the present design for SMORE utilizes the StatOil OC3-Hywind spar with a 5-MW National Renewable Energy Laboratory (NREWL) turbine, a device well documented by NREL (Jonkman et al., 2009; Jonkman, 2010). This wind turbine, as shown in figure 10.1, has a total draft of $D_{system} = 120$ m, an upper spar diameter of $d_{upper} = 6.4$ m and a lower spar diameter of $d_{lower} = 9.4$ m (Jonkman, 2010).

Design analysis and prototype testing by Haji et al. (2016) found that devices which used multiple subsystems for a uranium harvester allowed for a higher device uptime because complications that arise at sea were highly unlikely to affect all subsystems. However, because the cost of such a device is closely related to the material required, the considerable number of large gears to move the ball-chain enclosures suggest that the designs investigated by Haji et al. (2016) are likely to be extremely costly to fabricate, deploy, and maintain (Haji et al., 2017). The design presented

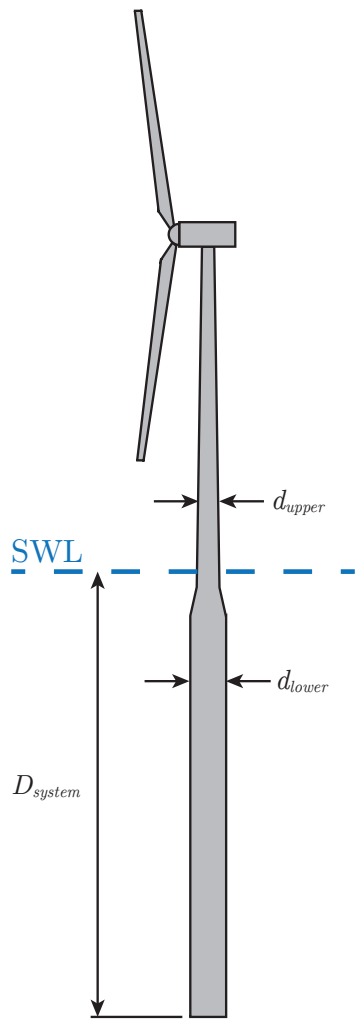

Figure 10.1: Schematic of 5-MW NREL-OC3-Hywind offshore wind turbine used as the base of the design of SMORE where SWL is the still water line. The turbine has a total draft of D_{system} = 120 m, an upper spar diameter of d_{upper} = 6.4 m and a lower spar diameter of d_{lower} = 9.4 m (Jonkman, 2010).

here utilizes adsorbent shells that are incrementally paced along high strength mooring rope, resembling conventional ball-chain belts, similar to those in the designs by Haji et al. (2016). The design described in this chapter mimics the modularized design structure of Haji et al. (2016), while using drastically fewer components. This design, referred to as the Symbiotic Machine for Ocean uRanium Extraction (SMORE), uses large rollers to move multiple ball-chain lengths at once. A simple schematic of a version of SMORE is shown in figure 10.2.

10.4.1 Ball-Chain Net

In this design, as in Haji et al. (2016), the shell enclosures of diameter d_s containing the adsorbent fibers are strung along high-strength marine grade rope, into a component

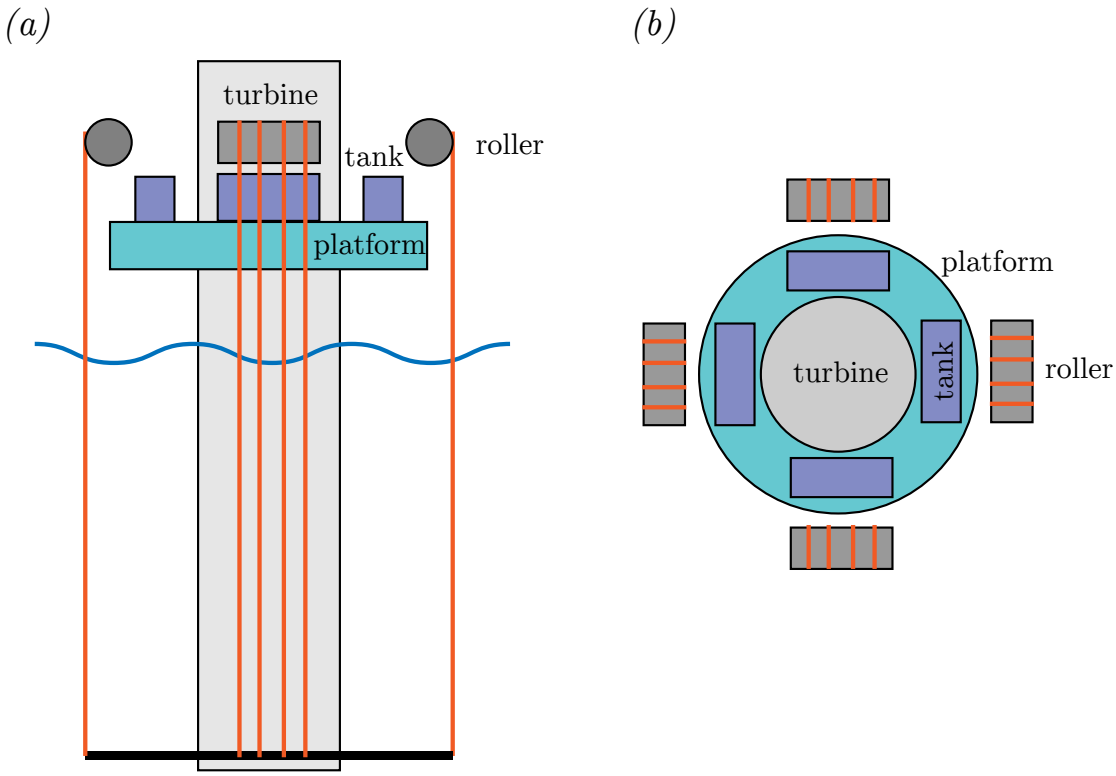

Figure 10.2: Schematic of the Symbiotic Machine for Ocean uRanium Extraction (SMORE). In this design, large rollers are used to move multiple ball-chain lengths of shell enclosures containing adsorbent fibers.

known as a ball-chain length for this design. The spacing between shells is given by L_s. Unlike the design in Haji et al. (2016), these lengths are then also placed together in multiple rows of spacing L_b such that cross-members of high-strength marine grade rope can be added after a certain number of shells in order to develop a net-like structure. These cross-members decrease the likelihood of tangling between ball-chain lengths and increase the rigidity of the overall component. A schematic of a ball-chain net is shown in figure 10.3, where the number of ball-chain lengths per net is $N_b = 4$.

Assuming a constant degradation of $d = 5\%$ with each elution cycle, an operating temperature of $T = 20°\text{C}$, the sorption optimization algorithm developed in Haji et al. (2015), indicates the device must be sized for approximately 45 tonnes of adsorbent. Note that the effects of biofouling are neglected for this first order analysis. Optimization on the design feasibility of winding the adsorbent fiber into filament balls as described Haji et al. (2015) shows this can feasibly be done with a shell diameter of $d_s = 0.5$ m and a total number of shells of $N_{st} = 11,064$. For this case study, the spacing between shells, L_s is taken to be 0.05 m.

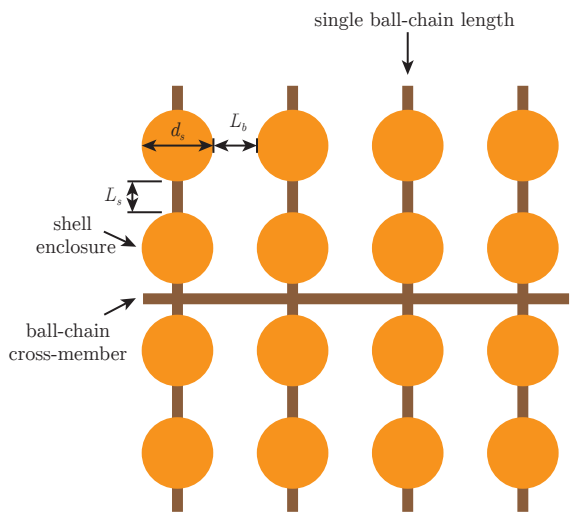

Figure 10.3: Schematic of a ball-chain net. In this image, the number of ball-chain lengths $N_b = 4$.

10.4.2 Roller Design

In SMORE, the adsorbent ball-chain nets are engaged and motorized by a roller. Each roller is sized to fit 12 shell enclosures around its circumference and the number of rollers per device is determined by the overall adsorbent required.

The roller diameter is determined by

$$d_{roller} = \frac{\sqrt{d_s^2 + L_s^2 - 2d_s L_s \cos(\alpha)}}{2\sin\left(\frac{\pi}{2N_{s,r}}\right)}, \tag{10.2}$$

where d_s is the shell diameter, L_s is the spacing between shells on the same ball-chain length, α is the angle separating the midpoints of the irregular polygon created by the shells and spaces that make up the circumference of the roller (see figure 10.4, and $N_{s,r}$ is the number of shells engaged by half of the roller, taken to be six in this design (so that the roller has places for 12 shells total around its circumference). By geometry, the angle α is given by

$$\alpha = \pi\left(1 - \frac{1}{2N_{roller}}\right). \tag{10.3}$$

Equations (10.2) and (10.3) result in a roller outer diameter of approximately $d_{roller} = 2.3$ m, and length of

$$L_{roller} = N_b(L_b + d_s) + 2N_b + 2d_{rail} \tag{10.4}$$

where d_{rail} is the diameter of the circular rail on the inside edges of the roller that act like a track for a set of U-groove wheels that rotate the roller. These dimensions are discussed in section 10.6. For this case study, the desired number of subsystems is four, hence $N_b = 10$ ball-chain lengths per roller. These rollers can be manufactured out of steel pipe, sized to be at least 0.05m thick.

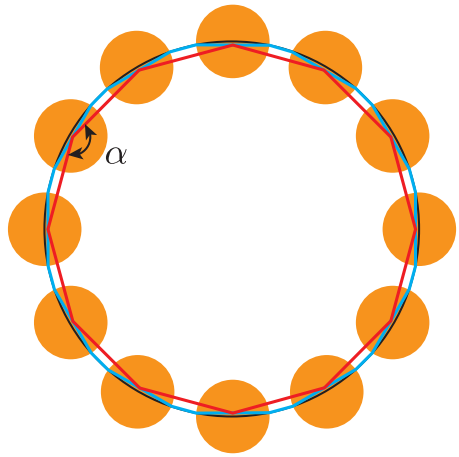

Figure 10.4: Schematic describing α. in terms of the shells (orange) around the roller (black line). The blue line is the irregular polygon created by the shells and the spaces that make up the circumference of the roller and the red line is the regular polygon inscribed by the midpoints of the irregular polygon sides. Here $N_{s,r} = 6$.

10.4.3 Platform Length

To determine the platform length, a spacing of $L_{sp,roller} = 1$ m between rollers is assumed. With this in mind, the total platform length required to fit all the rollers around the turbine (such that when viewed from above the turbine is circumscribed by a polygon made up of the rollers and spaces between them, a similar analysis as was done to determine the size of the roller to hold the desired number of shells around its circumference) is given by

$$L_{pt} = \frac{N_{roller}\left(L_{roller} + L_{sp,roller}\right)}{2\pi} - r_{upper} - \frac{d_{roller}}{2}, \tag{10.5}$$

where N_{roller} is the number of rollers (four for this design), L_{roller} is the length of the roller, $L_{sp,roller}$ is the spacing between rollers, and r_{upper} is the radius of the turbine at the top ($r_{upper} = \frac{d_{upper}}{2}$). Equation (10.5) yields a platform that must be at least $L_{platform} = 2.74$ m long, from the edge of the turbine. Furthermore, to ensure that the rollers are out of water and not impacted by slamming loads due to waves, the platform would be raised approximately $H_{platform} = 10$ m above the sea surface. Further analysis for a real ocean implementation would require that this height be adjusted according to the wave climate of the region of deployment.

10.5 Elution and Regeneration

Given that the bicarbonate elution process requires 24 hours of polymer immersion time and an additional 3 hours for regeneration, the rollers on SMORE would act mostly as anchors for the ball-chain lengths hanging off the system. The rollers would be motorized so that after a campaign length (taken to be 23 days for this design),

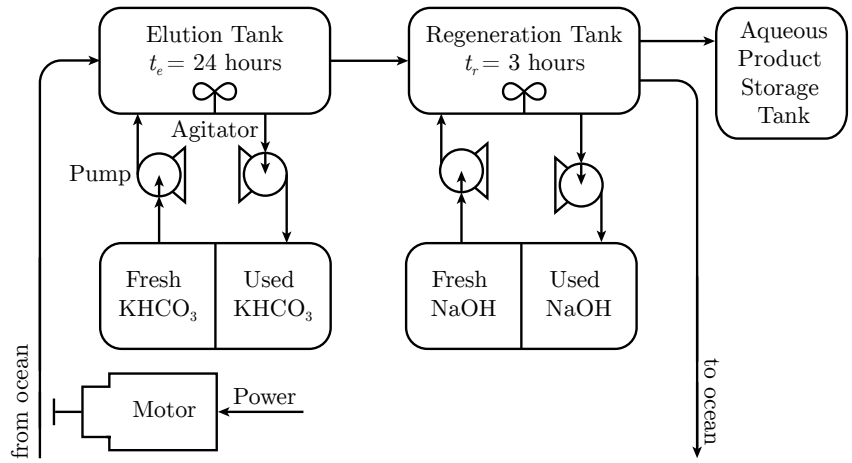

Figure 10.5: Schematic describing elution and regeneration process of polymer adsorbent.

the ball-chain lengths could be pulled up and deposited into a chemical tank beneath the rollers. This tank would then be filled with the solution required for elution of the adsorbent polymer. After 24 hours, the rollers would be powered in the opposite direction to redeploy the uranium adsorbent. One chemical tank is envisioned per subsystem. Figure 10.5 describes the elution and regeneration process including the chemicals and tanks involved. Further design analysis is required to determine the details of each of these tank systems which was not the primary focus of this project.

10.6 Roller and Wheel Subassembly

As described previously, each roller would be motorized in order to wind and unwind the ball-chain lengths. This is accomplished using grooved wheels on a circular track welded to the interior of the roller on both ends. The number of grooved wheels required is determined by using the maximum contact pressure for an ellipsoid region of Hertz contact between the wheels and the groove, given by

$$P_{max} = \frac{3F_c}{2\pi cd}, \tag{10.6}$$

where F_c is the contact force between each wheel and the rail (taken to be half the force on the roller divided by the number of wheels) and c and d are the major and minor contact area elliptical semi-axes, respectively. The semi-axes are a function of the geometry and material of the wheel and rail, and the angle between the planes of principal curvature of the two bodies. Their definitions can be found in Slocum (2008).

In order for the design to be feasible, two criteria must be met with respect to the wheels:

$$P_{max} \leq 1.5\sigma_{ult} \tag{10.7}$$

and

$$\gamma > 20^\circ \tag{10.8}$$

where σ_{ult} is the ultimate tensile strength of the grooved wheel and γ is the contact angle in degrees between the groove and the rail, found by

$$\gamma = \tan\left(\frac{r_{groove}}{b}\right)^{-1}, \tag{10.9}$$

where r_{groove} is the radius of the groove on the wheel. Analysis using equations (10.6)-(10.9) suggests that seven polyurethane wheels of approximately $d_{wheel} = 0.4$ m diameter with a groove diameter of approximately $d_{groove} = 0.35$ m on a $d_{rail} = 0.25$ m diameter steel track bent into a 2.1 m diameter circle to fit inside the roller. Furthermore, a 0.25 m diameter pipe may be bent into a minimum of a four times its diameter, or a 1 m diameter circle (H and H Tooling), therefore bending it to fit inside the 2.1 m inner diameter of the roller is feasible. To support the weight of the roller and the ball-chain lengths, each subsystem would be supported by circular steel tubing of appropriate diameter and thickness with a 45° angle cross-brace. Having determined this rail diameter, the resulting roller length is $L_{roller} = 6.6$ m by equation 10.4.

In order to move the rollers, one of the polyurethane wheels would be oriented completely vertically, so as to take the total load of half of the roller, and actuated using a motor. The torque required to move the roller due to friction between the wheel and the rail is

$$\tau_{fr} = \mu F_N \left(\frac{d_{roller}}{2} - d_{rail}\right), \tag{10.10}$$

where μ is the coefficient of friction between the polyurethane groove and the steel rail (taken to be $\mu = 0.2$) and F_N is half the total force on the roller due to the shells, its mass, and the tension on the ball-chain net. Analysis of this friction force indicates that the friction between the wheel and rail provides enough torque needed to move the rollers.

10.7 Power Requirement

The power required for the full-scale system is a combination of the power required to move the adsorbent ball-chain net using the rollers, the power required for the chemical elution and regeneration, and the power required to pump the chemicals throughout the system.

10.7.1 Friction Between Wheels and Rail

In the case of the power required to move the adsorbent ball-chain, the dominant forces to overcome are the friction between the driving wheel and rail and the tension force required to keep the ball-chain net taut. Given τ_{fr} by equation (10.10), the power required to move the roller against this friction is

$$P = \tau_{fr}\omega, \tag{10.11}$$

where ω is the roller speed in rad/s.

10.7.2 Ball-Chain Tension

Following the analysis presented by Hamlet (2017), the tension force required to keep the ball-chain from deflecting under the current loads of the ocean can be found by considering the cable to be a tensioned-beam. Following the analysis described in Sparks (2007), the ball-chain rope can be considered a cable under a lateral current load. Figure 10.6 illustrates this scenario, where $f(s)$ is the force per unit length due to the ocean currents, and w is the apparent weight per unit length (assumed to be constant). The angle of deflection θ is assumed to be large in this analysis.

Considering the forces normal to the segment axis and assuming static equilibrium yields

$$F - wds\cos(\theta + d\theta) - (F + \delta F)\cos d\theta + (T + dT)\sin d\theta - f(s)ds = 0, \tag{10.12}$$

where F is the shear force and T is the tension in the ball-chain. Dividing by the length ds, and simplifying gives,

$$\frac{dF}{ds} + w\cos\theta - T\frac{d\theta}{ds} + f(s) = 0. \tag{10.13}$$

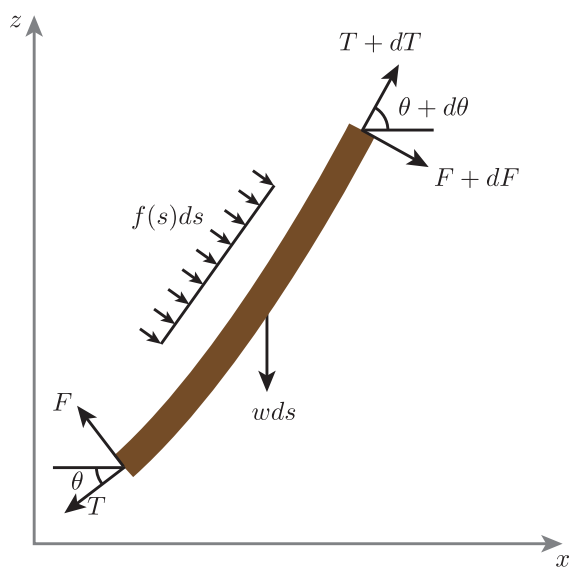

Figure 10.6: Model of small segment, ds, of the ball-chain under a lateral current load, $f(s)$, with constant apparent weight per unit length, w. The axis following the segment is given by s, F is a sheer force, T is the tension in the ball-chain, and θ is the angle the cable makes with the horizontal.

The shear force F is equal to $\frac{dM}{ds}$, and the curvature $\frac{1}{R} = \frac{M}{EI} = \frac{d\theta}{ds}$, where M represents the internal moment, E is the Youngs Modulus, and I is moment of inertia of the cross section (Sparks, 2007). Equation (10.13) is therefore recast as

$$\frac{d^2}{ds^2}\left(EI\frac{d\theta}{ds}\right) - T\frac{d\theta}{ds} + w\cos\theta + f(s) = 0, \tag{10.14}$$

where EI is the bending stiffness, T is the effective tension, w is the apparent weight per unit length, and $f(s)$ is the applied load function. A cable can be considered to be a tensioned-beam for which the bending stiffness is neglected, (i.e. $EI \approx 0$), which results in equation (10.14) simplifying to

$$\frac{d\theta}{ds} = \frac{w\cos\theta + f(s)}{T}. \tag{10.15}$$

Similarly, considering the forces tangent to the segment, assuming static equilibrium and neglecting bending stiffness ($EI \approx 0$), and neglecting components of $f(s)$ tangent to the ball-chain, results in

$$\frac{dT}{ds} = w\sin\theta. \tag{10.16}$$

The current load is expressed as

$$f(s) = \frac{1}{2}\rho C_d d(s) U(s)^2, \tag{10.17}$$

where ρ is the density of seawater, C_d is the drag coefficient, $d(s)$ is the weighted hydraulic diameter of the segment (taking into account both the shell and rope sections), and only the component of the current normal to the ball-chain is considered, that is $U(s) = u(s)\sin\theta$.

The elongation of the rope chosen to string the shells together in the ball-chain arrangement is also considered. Given the tension in a segment of the rope and the equation found for strain, the elongated length of each segment of rope is written:

$$ds_{elong} = ds_{initial}(1 + \epsilon(s)), \tag{10.18}$$

where $\epsilon(s)$ is the strain of the ball-chain segment, which at each point can be computed from the tension.

Equations (10.15), (10.16), and (10.18) govern the forces on the ball-chain length and can be used to determine the tension, T, and angle, θ, for each point along the ball-chain length. In order to satisfy boundary conditions which were given by the SMORE geometry, the initial tension and angle at the bottom of the roller were imposed and the Forward Euler method of numerical integration was used to calculate the position of the top end of the rope. The calculated position was compared to the known boundary condition on the top end, and if they were sufficiently similar, less than 10^{-4} difference, the initial guesses were correct. If not, the system was solved iteratively using Excel's GRG nonlinear engine to find the correct initial tension and angle.

10.7.3 Elution and Regeneration Processes

The chemical elution and regeneration processes require power for a propeller to agitate the chemical bath as well as temperature control for the baths. For the initial design, the agitator power was determined as a percentage of the power required in the reference case of 3 kW, detailed by Sachde (2011) and Schneider and Sachde (2013), based on the the amount of adsorbent eluted annually by SMORE as compared to that in the reference case.

In addition to this, the chemical baths must be raised to 40°C for the full duration of the elution and regeneration (University of Idaho). The power required to maintain this temperature is given by

$$P = \frac{Q}{t} = \frac{mc_p \Delta T}{t}, \tag{10.19}$$

where Q is the energy required, t is the time over which the chemical processes take place ($t_e = 24$ hours and $t_r = 3$ hours for the elution and regeneration processes, respectively), m is the mass of the chemicals and adsorbent required to be headed, c_p is the specific heat of the solution (taken to be that of water for initial analysis), and ΔT is the temperature difference. For this case study, a temperature difference of 20°C was considered.

10.7.4 Chemical Pumping Power

For this design, it is assumed that the chemicals could be stored within the turbine itself. This is very advantageous as offshore wind turbines often require a lot of ballast mass to ensure stability. The overall weight of the reference turbine, is 7466 tonnes (Jonkman, 2010). Because the numbers for the amount of ballast used for a wind turbine are proprietary and therefore very difficult to find, it is assumed that the ballast is likely no more than 10% of the overall system mass, or 747 tonnes.

The power required to pump the chemicals from the bottom of the turbine to the location of the chemical tanks on the platform can be determined from

$$P = N_p \frac{P_h}{\eta_p} \tag{10.20}$$

$$= N_p \frac{\rho g h_{sys} q}{(3.6 \times 10^6)\eta_p} \tag{10.21}$$

where N_p is the number of pumps (determined by the number of subsystems), P_h is the hydraulic power in kW, η_p is the pump's efficiency (taken to be 30%), ρ is the density of the solution being pumped (assumed to be similar to water), g is gravity, h_{sys} is the head distance over which the fluid needs to be pumped and q is the flow capacity in m^3/h, taken to be 1 m^3/h for this analysis.

10.8 Design Analysis

The detailed design analysis was incorporated into an Excel spreadsheet that allowed for the quick analysis of various designs by changing only a few constraints. For instance, the current speed in the proposed deployment location could be changed, thereby resulting in a new tension force required to keep the ball-chain net taut, and hence a new torque requirement for the roller system. Additionally, the system could be changed from a stationary system (in which the rollers are only used to wind up the adsorbent net for chemical processing) to a continuous system (in which the adsorbent net is strung between an upper and lower set of rollers such that it is moved continuously). An example design is detailed in table 10.1 and a three-dimensional sketch of a 1/10th physical scale system of such a design is shown in figure 10.7.

Table 10.1: Example SMORE design

Parameter	**Value**	**Notes**
System type	Stationary	
Current speed, V_{cs}	1 m/s	Reasonable for boundary currents
Bottom current speed, $V_{cs,b}$	0.01 m/s	
Depth to bottom current, D_{cb}	25 m	
Shell diameter, d_s	0.5 m	Input
Spacing between shells, L_s	0.1 m	Input
Shells per turbine, N_{st}	5532	Optimized by shell model (Haji et al., 2015)
Ball-chains lengths per roller	10	Input
System depth, D_{sys}	80 m	Input
Platform height above SWL, H_p	10 m	Input
Rollers, N_{roller}	4	
Roller diameter, d_{roller}	2.3 m	
Roller inner diameter, $d_{roller,in}$	2.1 m	
Roller length, L_{roller}	6.6 m	
Spacing between rollers, $L_{sp,roller}$	1 m	
Platform length, L_{pt}	2.74 m	
Rail radius, r_{rail}	0.25 m	
Groove radius, r_{groove}	0.35 m	
Wheels per rail, N_{wheel}	7	Considering polyurethane wheels
Ball-chain rope diameter, d_r	0.016 m	
Ball-chain top tension, T_{top}	18620 N	
Ball-chain bottom tension, T_{bot}	17911 N	
Ball-chain max displacement, y_{max}	1.94 m	
Chemical agitation power, P_{ag}	12 kW	
Chemical heating power, P_{heat}	9.96 kW	
Chemical pumping power, P_{pump}	2.98 kW	
Roller motorizing power, P_{roller}	117 kW	
Total power required, P_{total}	172 kW	

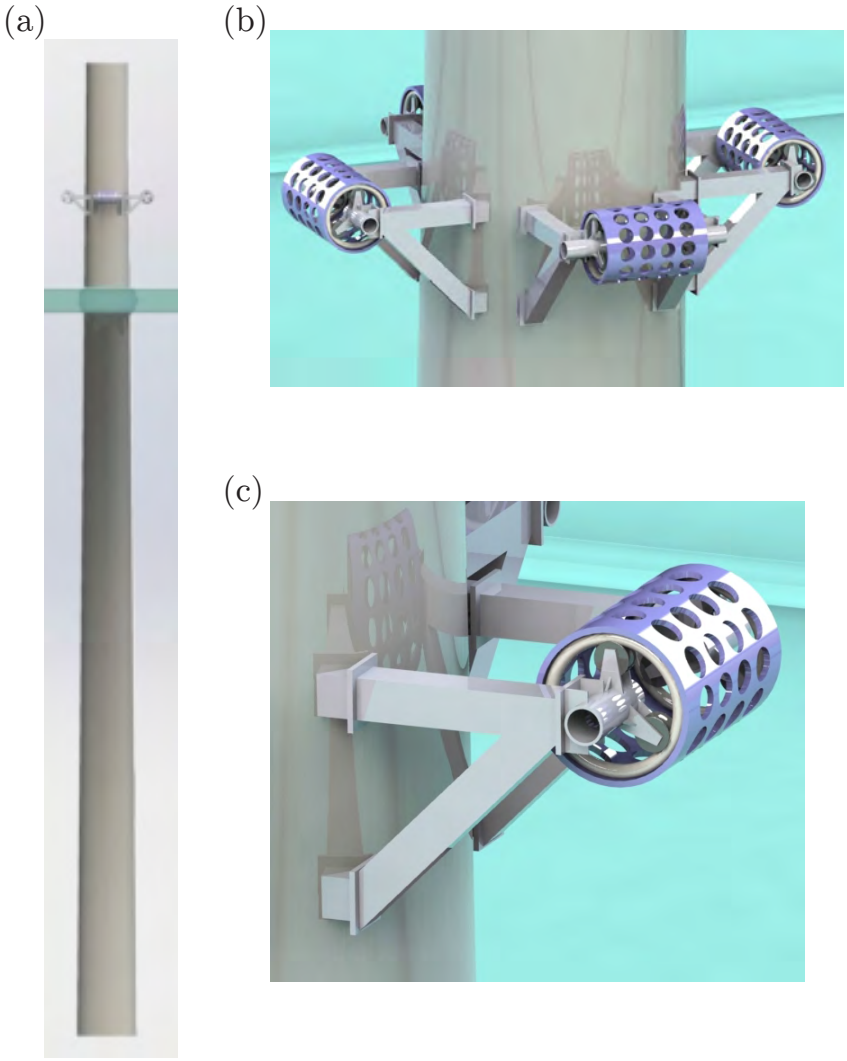

Figure 10.7: Three-dimensional model of SMORE for the a 1/10th physical scale version of the design case outlined in table 10.1. The entire 1/10th scale system is show on the turbine spar in (a); whereas (b) shows a close-up of the upper platform, and (c) is a close up of one of the roller subsystems (shown in purple).

SMORE 1/10th Physical Scale Prototype Ocean Test

This chapter describes the design and ocean testing of a 1/10th physical scale prototype of the Symbiotic Machine for Ocean uRanium Extraction (SMORE). This research was done in collaboration with Dr. Ken Buesseler and Jessica Drysdale at the Woods Hole Oceanographic Institution. The results of this test will inform the design of a full-scale, symbiotic system to harvest uranium from seawater. This chapter has also been detailed in milestone report: M3NU-14-MA-MIT-0601-016.

11.1 1/10th Physical Scale Prototypes

In the full-scale design, described in the previous chapter, large rollers are used to move ball-chain nets down the entire length of the turbine. One question that arose in the development of the design was whether the ball-chain nets should be continuously moving through the ocean or (i.e. should the rollers continuously cycle the ball-chain net like a conveyor belt through the ocean?) completely stationary. The additional movement of the ball-chain net might induce more seawater flow to the fiber adsorbents within the shells and hence increase the uranium adsorbed. However, the additional complexity of a continuously moving system as opposed to a stationary system would likely result in higher capital and operational costs for the machine. The question remains as to whether the value of the additional uranium adsorbed by a system continuously moving the adsorbent fibers would offset the increased cost of the system due to its increased complexity. For this reason, two modules were prototyped at a 1/10th physical scale for prolonged ocean testing: one system in which the net remained stationary and another in which the net was continuously moving. Figure 11.1 shows the main components of each of the two systems and their location on a wooden float for ocean testing.

11.1.1 System 1: Stationary net system

The stationary net system, shown in figure 11.2, comprised a roller and wheel assembly, surface support structure, motor and gearbox, power transmission using a timing belt, battery, 18 ft long bottom support structure, and two guide wires. The roller was constructed from a 8.625 in outer diameter pipe, 0.322 in thick, with a length of

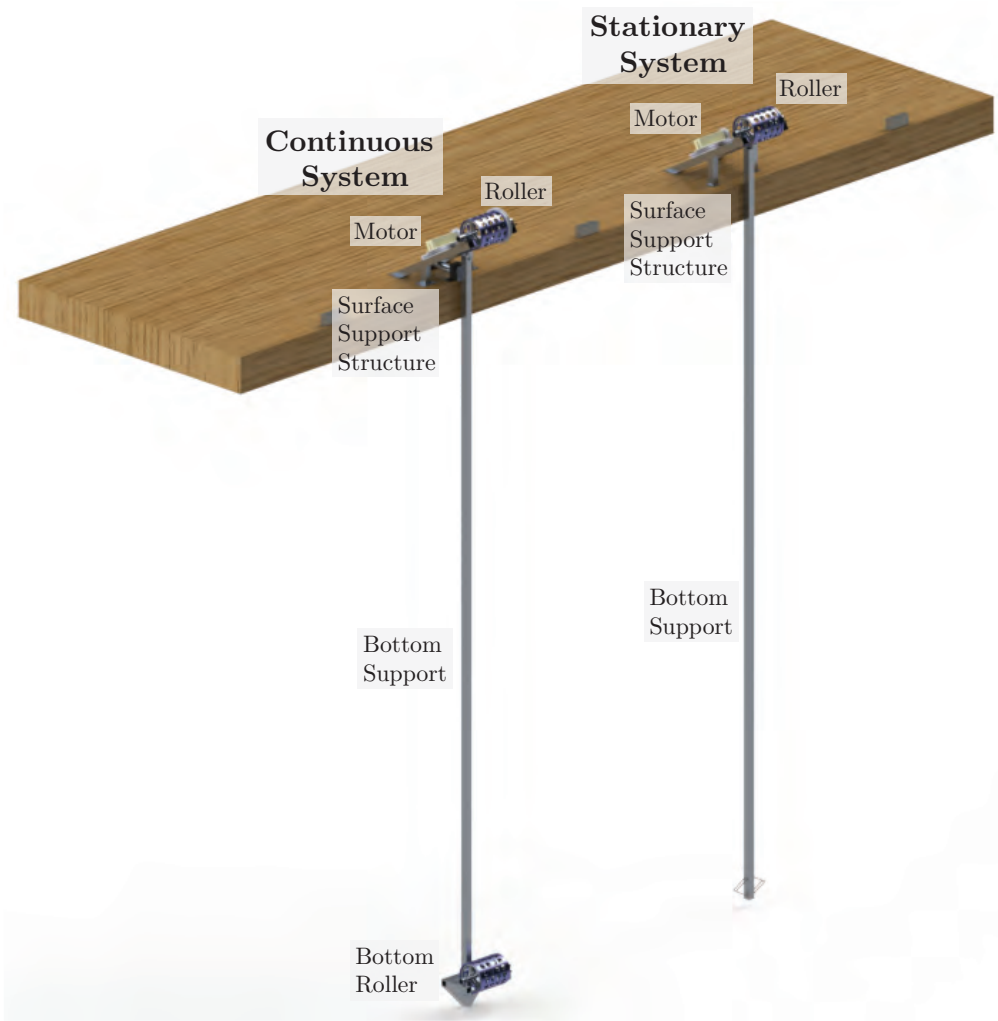

Figure 11.1: Three-dimensional model of 1/10th physical scale model for ocean testing of the SMORE design. Both a stationary and continuous version of the design were fabricated and mounted to a wooden float for ocean testing.

11 in and 1.6 in diameter circular holes to fit the shells of the adsorbent net. The roller was designed to fit 13 shells along its circumference and four shells along its length.

The roller was motorized in order to wind and unwind the shell enclosure net periodically to retrieve adsorbent samples. This motorization was accomplished using grooved wheels on a circular track welded to the interior of the roller on either end (figure 11.2b). The number of grooved wheels required was determined by using the maximum pressure of the contact for an ellipsoid Hertz contact between the wheels and the groove, as well as the friction required to provide sufficient torque to move the roller. Using a similar analysis to that described in chapter 10, it was found that three polyurethane wheels of approximately 1.77 in outer diameter along a 0.675 in diameter aluminum rail would be sufficient.

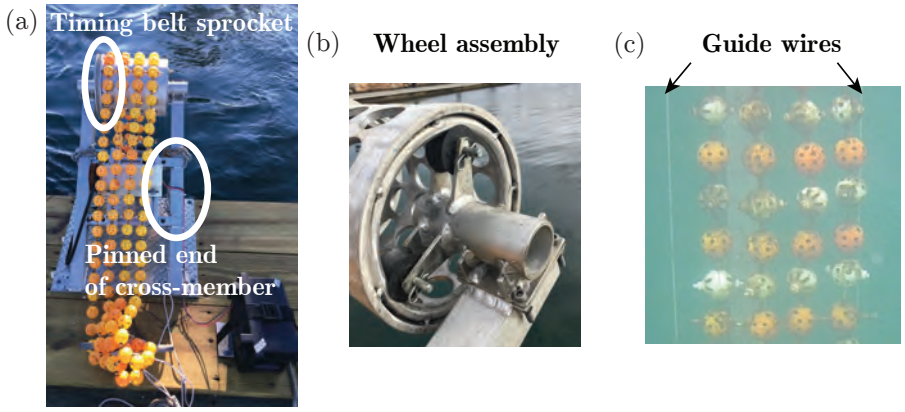

Figure 11.2: Stationary system design of (a) surface structure, (b) wheel assemblies, and (c) net and guide wires.

A brushed DC motor with a torque rating of 345 oz-in was used to drive the roller. The motor was fitted with a 12:1 gearbox in order to reduce the speed. The power was transmitted using a timing belt from the motor to a fabricated sprocket welded to the exterior of the roller. The motor was powered using a 7 amp, rechargeable lead acid battery housed in a waterproof battery box mounted next to the surface structure of the stationary system.

A thrust bearing was used on one side of the top wheel on the belt side of the roller to counteract the force of the timing belt pulling the belt side of the roller and thereby causing the top wheel to fall out of alignment and possibly causing it to rub to one side resulting in premature failure due to friction. This bearing was able to take the radial load of the wheel pushing against the side support and push the wheel back towards the intended alignment. All other wheels would then move to compensate for the imperfections in the welded rails as needed, so as not to over-constrain the system.

The wheel assemblies were first connected to the roller and then bolted into surface support members. In order to ensure alignment between the roller and both wheel assemblies without over-constraining the system, the surface support structure was fabricated with a cross-member connecting the two sides. This cross-member was welded to one surface support and pinned to the other using carriage bolts through a thin attachment plate. These cross-members also served as a mount for the motor subassembly. The entire surface assembly was then bolted into an aluminum plate to maintain alignment and this aluminum plate was then bolted onto the wooden float.

To reduce the likelihood of the stationary adsorbent net experiencing entanglement or being dragged away by strong currents, it was clipped in place to galvanized vinyl-coated wire rope that was attached on either side of the bottom support pole (figure 11.2c). Given that the net was inherently buoyant, small dive weights were added to the bottom of the net to ensure it did not float.

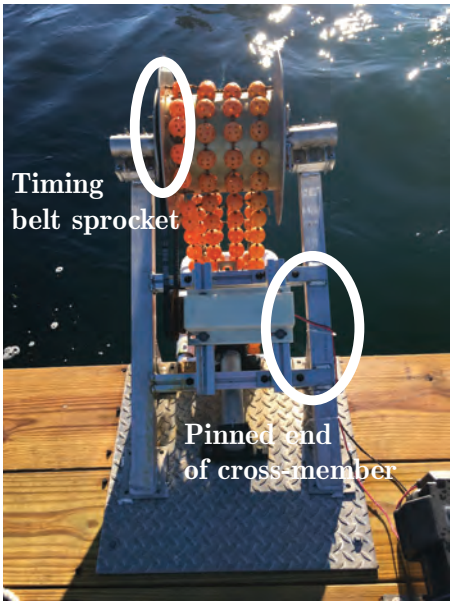

Figure 11.3: Fabricated surface structure of the continuous system design.

11.1.2 System 2: Continuous net system

Aside from the bottom support, net, and motor assembly, the continuous net system was analogous to the stationary net system. In the case of the continuous net system, the shell enclosure net was a complete loop, effectively making a conveyor belt. Originally, a roller, similar to the one on the surface, was designed to be attached to the bottom of the 18 ft long bottom support.

As with the stationary system, a brushed DC motor with a torque rating of 345 oz-in was used to drive the roller. However, the speed was reduced significantly using a 256:1 gearbox. The motor was powered by a 12V AC to DC converter, rated for up to 25 amps. On average, the system drew approximately 8 amps, resulting in an output torque of approximately 15 oz-in. The resulting linear velocity of the adsorbent net was approximately 4.7 in/s ($\sim$ 12 cm/s).

11.2 Ocean Test Site

The prototypes were tested at the Massachusetts Maritime Academy (MMA) in Buzzards Bay, MA. They were located at the end of the MMA dock where the water depth was approximately 23 feet at low-tide. Although fairly close to shore, the tides in this location vary up to 6 feet and the currents can be extremely strong due to the proximity to the Cape Cod Canal, which frequently has currents of about 5 knots (2.6 m/s). Additionally, the wind often generates waves of approximately 1-2 feet in height at this location. For these reasons, this site was deemed to have conditions that could provide valuable results from the prolonged ocean testing of the 1/10th physical scale SMORE prototypes.

(a) (b)

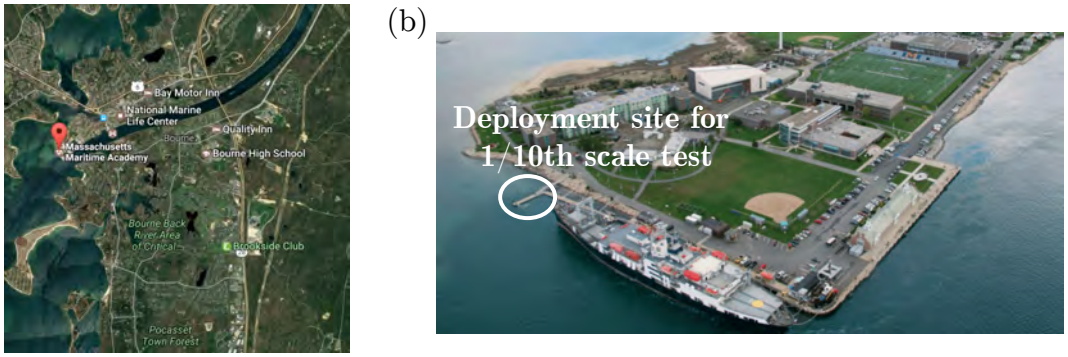

Figure 11.4: Massachusetts Maritime Academy (MMA) (a) location in reference to Cape Cod Canal and Buzzards Bay, and (b) aerial view of MMA's campus with the location of the prototype test indicated by the white circle.

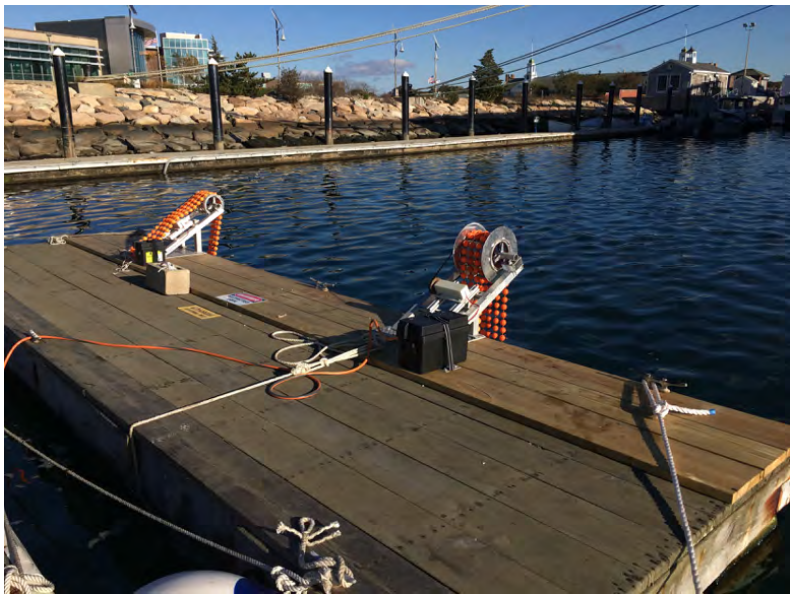

Figure 11.5: Both prototypes mounted to the wooden float and moored to the end of the MMA dock during testing.

Both systems were mounted to a single wooden float measuring 24 ft long and 7 ft wide which was moored to the end of the MMA concrete dock. A variety of ocean sensors were also deployed along with the prototypes. These sensors were mounted at various depths along a piling located at the end of the concrete dock within 3 ft of the wooden float, where the ocean depth was approximately 19 ft at low tide.

11.3 Shell Enclosure Net

In the prototypes designed and tested in this chapter, the adsorbent shells were incrementally spaced along high strength mooring rope, and then strung together to

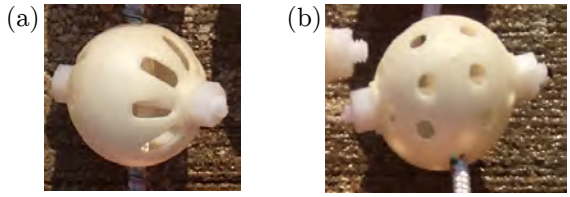

Figure 11.6: Shell designs for the testing of uranium adsorption fibers using (a) slotted holes and (b) circular holes.

Figure 11.7: Small section of net with white shells for adsorbent fibers. Adsorbent enclosure shells were alternated with orange placeholder shells used for mechanical testing.

create a net using cross-members of the same rope to increase the net's rigidity and reduce the likelihood of tangling. Both prototypes used the same type of net, with four lengths of shells combined to make a single net. The vast majority of the shells for the ocean test did not contain uranium adsorbing fibers and were used primarily to test the mechanical components of the system. The net for the stationary system was approximately 20 ft long and used a total of 430 shells. The net for the continuous system was about 42 ft in length and required 960 shells.

The net was constructed by stringing placeholder 1.6 in diameter shells along 3/16 in diameter rope. The rope comprised of a braided cover and a braided core made from high-performance aramid, also known as Technora, resulting in a high-temperature (rated up to 300°F), wear-resistant rope meant for lifting (rated for 550 lbs capacity). The shells were spaced approximately 0.45 in apart lengthwise such that 13 shells fit around the circumference of a 8.625 in diameter roller, and approximately 2.23 in apart widthwise, so that four lengths fit along the length of the 11 in roller. The shells were kept in place along the rope by 16 gauge steel c-ring staples.

To test the uranium uptake of the AI8 adsorbent fibers used on the prototypes, two shell designs were investigated, as shown in figure 11.6. The first used slotted holes while the second used circular holes. Each net included nine of each type of design, for a total of 18 shells per net that would include AI8 fibers (see figure 11.7). The shells were 3D printed out of acrylonitrile butadiene styrene in two halves with a

series of tabs and corresponding slots to ensure the two halves were aligned the same way each time they were connected. The two halves were kept together using a 1/4 in threaded acetal rod placed through the middle and two nylon hex nuts on either end. On the stationary net, the shells with the adsorbent fiber were placed approximately 10 ft below the ocean surface so that they were about mid-depth in the water column when deployed. In the case of the net for the continuously moving system, two narrow cable ties were also used to secure each half of the shells together to ensure the shells would not come apart unintentionally. The shells were made water-proof using three coats of polyurethane to reduce the amount of water absorbed by the shells which could cause unwanted deformation during the experiment.

11.4 Adsorbent Deployment and Sampling

As mentioned previously, each system contained 18 shells in which the uranium adsorbent was placed, for a total of 36 shells with adsorbent fibers. The adsorbent was deployed as a "mini braid" (figure 11.8), a pre-weighed, small mass (80-100 mg) of adsorbent fiber that was cut from a common AI8 adsorbent braid prepared by Oak Ridge National Laboratory. Each mini braid was weighed before deployment, after retrieval, and also after sample digestion. The weight after retrieval would include any amount of biofouling (the growth of organisms on the fiber), however it would not account for any loss of fiber occurring during the deployment. The weight after sample digestion would allow for the determination of adsorption capacity as a function of the adsorbent mass.

The stationary system included two mini braids per shell while the continuous system had about one to two mini braids per shell. Additionally, mini braids were included in two nylon mesh bags at the bottom of the stationary net to act as controls (i.e. to determine if the shells significantly inhibited the uptake of uranium due to the shell's obstruction of seawater flow). The first adsorbent sample was collected 24 hours after deployment. The eight subsequent samples were collected every seven days

Figure 11.8: Pre-weighed adsorbent mini braid. One to two of these mini braids were placed in each shell design on each of the two prototypes.

after deployment. This sampling resulted in a determination of uranium adsorption as a function of time for each system, each shell design, as well as the control bags. Water samples were also collected on each of the nine sample dates for trace metal analysis.

11.5 Ocean Test Measurements

Along with the mechanical testing of the physical prototype, sensors were placed throughout the water column to measure physical properties of the ocean that directly affected the uranium adsorption rates of the fibers during the deployment. Most of the sensors were mounted at various depths along a piling at the end of the dock at MMA, within 3 ft of the wooden float with the prototypes. All sensors placed on the piling were deployed on August 10, 2016 and retrieved on December 18, 2016. In addition to the sensors on the piling, a Xylem EXO-2 Sonde measured salinity as part of a water quality assessment of Buzzards Bay from October 4, 2016 to December 13, 2016. The location of the prototype float test, the pilings, and the Xylem sensor are shown in figure 11.9. Figure 11.10 shows the distribution of sensors along the piling.

Temperature has been shown to have strong implications of the adsorbent's uranium uptake. For the case of the AI8 fiber, equation (10.1) becomes:

$$y = \frac{(0.3775T - 0.2077)t}{(0.4083T + 14.13) + t} \tag{11.1}$$

where T is the temperature, °C and y is the resulting uptake of uranium (g U/kg adsorbent). Figure 11.11 shows the resulting time-dependent uptake for the AI8 adsorbent for T = 10°C, 15°C and 20°C as predicted by (11.1). As can be seen from the figure, a difference of just 5° in temperature results in an over 50% increase in the uranium uptake.

Temperature was measured throughout the water column as well as on the two prototypes using ONSET Tidbit Water Temperature Loggers. One Tidbit, sampling in 30 second intervals, was mounted on the continuously moving net below the section of the white shells containing adsorbent. Another, sampling at 5 minute intervals, was mounted in a similar location on the stationary system, and a third, sampling at 5 minute intervals, was placed in one of the nylon mesh bags at the bottom of the stationary system.

Salinity has also shown to have a large impact on the adsorbent's uranium uptake as it directly indicates the amount of uranium present in the water by a well-defined relationship between ^{238}U concentration in seawater and salinity where the concentration of ^{238}U in (ng g^{-1}) shown by Owens et al. (2011) to be described as

$$^{238}\mathrm{U}(\pm 0.061) = 0.100 \times \mathrm{S} - 0.326 \tag{11.2}$$

where S is the salinity.

Hence, the salinity was measured at mid-depth in the water column using a HOBO U24 Conductivity Logger (which also measured temperature), sampling at 15 minute

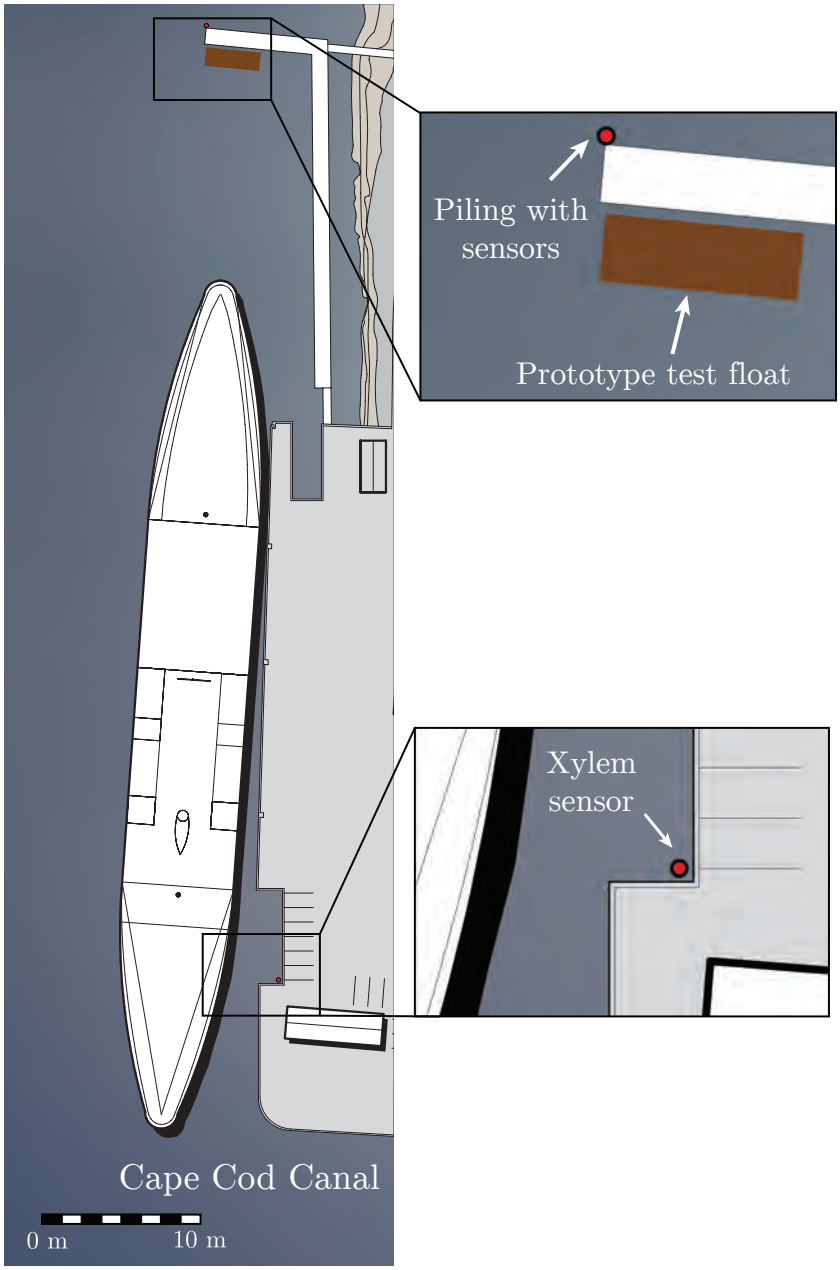

Figure 11.9: Map of MMA indicating the location of the wooden float with the prototypes, the piling to which most of the ocean sensors were attached, and the Xylem sensor. Note: the pier to which the Xylem sensor was located is fixed, not floating, on pilings and has water free flowing under it. The spot that the Xylem sensor was located was not protected by the pier and ship as the bird's eye view suggests.

intervals. It was also measured by the Xylem EXO-2 Sonde, mounted 3 ft above the seafloor, sampling at 15 minute intervals.

The amount of light has been shown to have strong effects on the biofouling

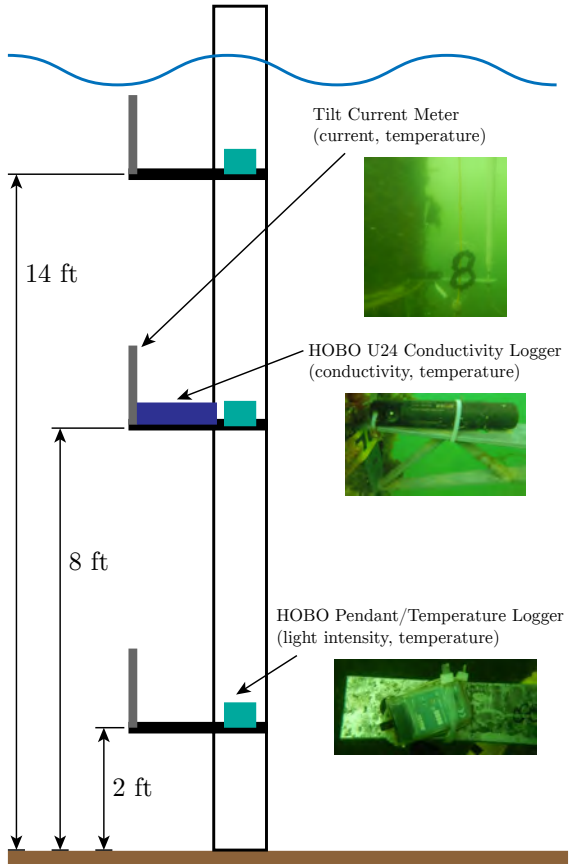

Figure 11.10: Layout of instruments attached to piling at the end of the dock.

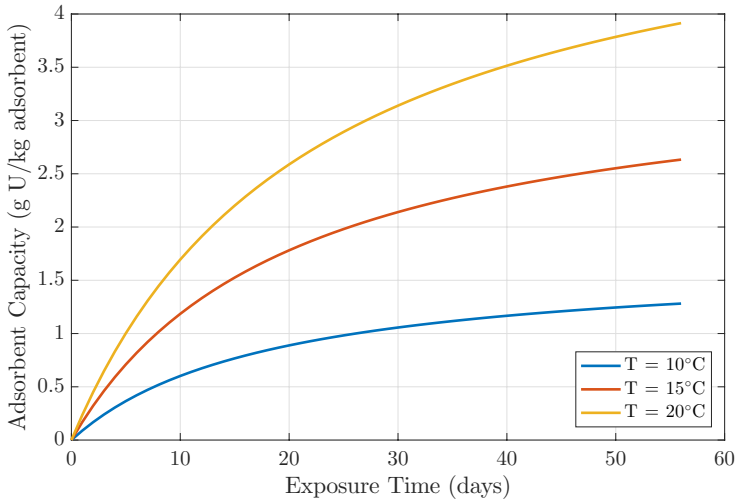

Figure 11.11: Time-dependent uptake of uranium for the AI8 adsorbent fiber as predicted by 11.1 for T = 10°C (blue line), 15°C (red line) and 20°C (yellow line).

of the adsorbent and the related uranium uptake (Park et al., 2016). In order to gather quantifiable data related to biofouling, light was measured at three depths

using HOBO Pendant Light/Temperature Loggers (which also measure temperature), sampling at 10 minute intervals.

Previous work has shown that the uranium adsorbed by the adsorbent fibers is also highly dependent on the flow rate of the water (Ladshaw et al., 2017). In order to gather information regarding the water flow seen by the two prototypes, current was measured using Tilt Current Meters from Lowell Instruments, placed at three depths. The current meters also measured temperature and were programmed to sample every second.

11.6 Results

The prototypes were deployed for a total of 56-days, starting on October 18, 2016 and ending on December 13, 2016. The first adsorbent sample was taken 24 hours after deployment on October 20, 2016 and the ninth and final sample was completed on day 56. The results described below include insights gained from the mechanical testing of the system, comparison between the stationary and moving systems, as well as the physical properties and changes over time of the seawater at the test site itself.

11.6.1 Continuous System Modifications

In the original the continuous net system design, the adsorbent net was placed in tension between the roller above the ocean surface and one attached to the bottom support structure, such that the adsorbent net transmitted the movement from the upper roller to the submerged roller. Ensuring there was enough tension in the system in order to accomplish this proved to be difficult as the currents could be extremely strong and resulted in either causing the adsorbent net to slip off the bottom roller (figure 11.12*a*), or, after additional guides were welded on to the ends of the bottom roller, to move out of alignment on the roller (figure 11.12*b*).

Because providing enough tension was difficult, the moving bottom roller was replaced with a stationary 4 in diameter PVC pipe. This allowed for the adsorbent net

(a) (b)

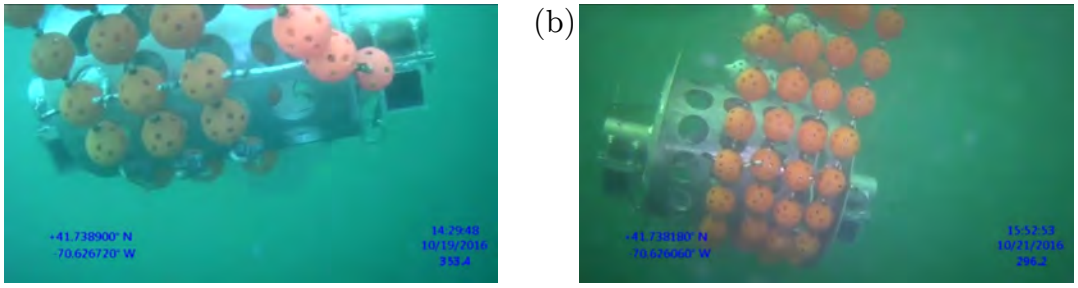

Figure 11.12: Issues with the bottom roller that arose due to the inability to provide enough tension in the adsorbent net for prolonged periods of time. The adsorbent net was found to (a) slip off or (b) fall out of alignment with the roller.

(a) (b)

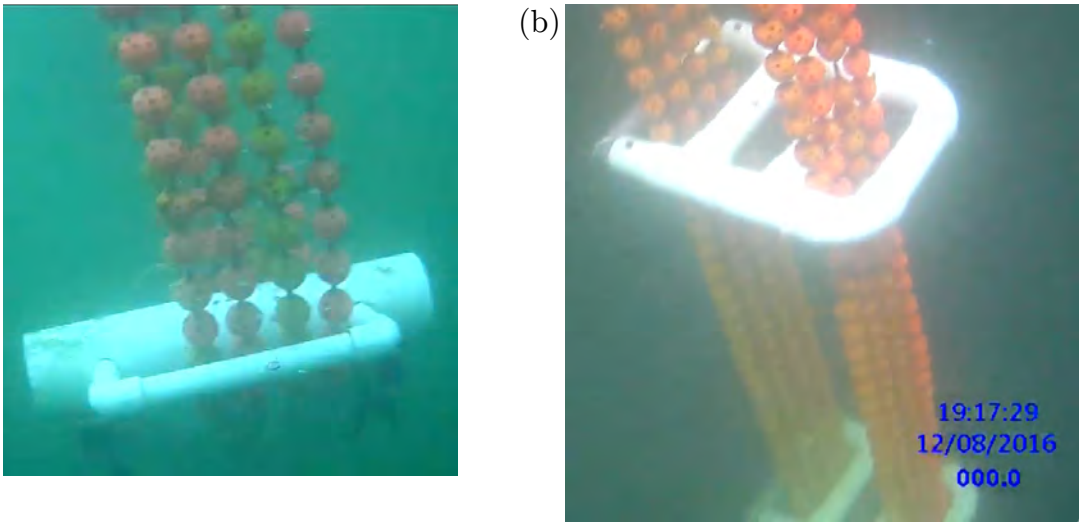

Figure 11.13: Major modifications made to the continuous system consisted of a (a) stationary 4 in diameter PVC pipe to replace the moving bottom roller and (b) a series of PVC guides along the length of the bottom support to keep the net separated and prevent tangling and misalignment due to strong currents.

to easily slide over the pipe and be completely driven by the upper roller. Additionally, to prevent movement and tangling between the two sides of the net due to the strong currents, guides that separated the two sides of the net were added at four points along the length of the bottom support. The guides also ensured good alignment between the net and the upper roller as it exited the water.

These complications and design modifications resulted in intermittent operation of the continuous system. In total, the continuous system was moving for approximately 37% of the total deployment, mostly towards the end of the experiment, with the longest three operations being 5.9 days, 5 days, and 4.7 days. Failures toward the end of the deployment were due to ice build up caused by the dropping temperatures off the coast of Massachusetts with the onset of winter.

11.6.2 Sensor Data

With the exception of the failure of the Tidbit temperature sensor located with the shells of the stationary net, the premature battery failure of the current meters (which stopped logging at approximately day 25 of the 56-day deployment), and an issue with the U24 meter's conductivity readings, data was collected from all sensors throughout the entirety of the experiment.

As expected, the light intensity dropped off exponentially with depth (figure 11.14*a*). The exponential drop off is most pronounced in the beginning of September (with a difference of about 88% in the light intensity between the upper and lower light sensors) and is least pronounced in December (with a difference of about 59% between the upper and lower light sensors). This reduction in light attenuation was likely due to less plankton and biota in the water in the fall and winter than the

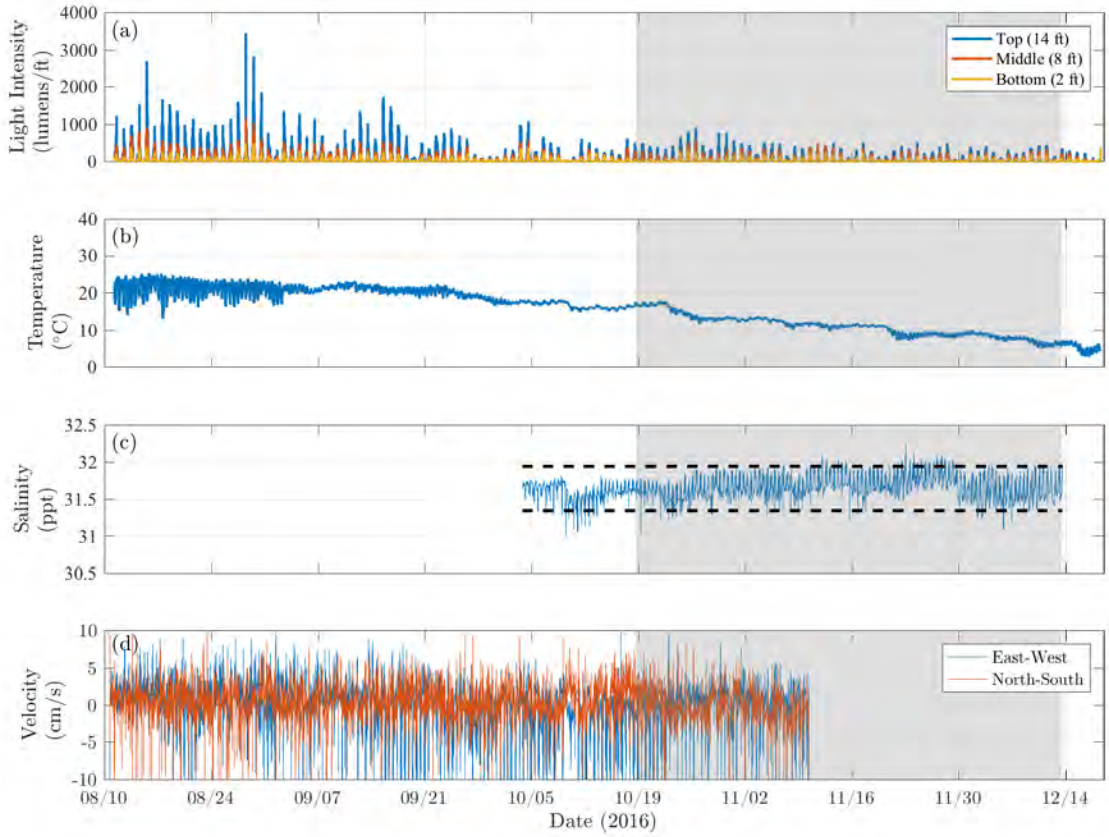

Figure 11.14: (a) Light intensity as measured by the top, middle, and bottom light sensors. (b) Temperature as measured from the U24 conductivity logger. (c) Salinity as measured from the Xylem EXO-2 Sonde salinity meter with dashed lines indicating $\pm 2\hat{\sigma}$ where $\hat{\sigma}$ is the robust standard deviation. (d) Current as measured from the bottom current meter with the dashed lines indicating $\pm$ 20 cm/s. The gray rectangle indicates the period of the ocean test, October 20, 2016 - December 13, 2016.

summer.

Similarly, seasonal variations could also be seen in the temperature data as shown in figure 11.14b (note that there was excellent agreement in the temperature measured by all instruments so only the data from the conductivity logger is shown). The short term temperature differences were linked to the tidal variations at the site, with these variations becoming less pronounced over time. From equation (11.1), it is clear that temperature has a major affect on the uranium uptake. For instance, at a temperature of 18°C, as seen close to the start of the 56-day deployment, by (11.1), the adsorbent capacity is estimated to be approximately 3.47 g-U/kg-ads after 56 days. On the other hand, at a temperature of 5°C, as seen close to the end of the 56-day deployment, the capacity is predicted to be decreased by 83% to approximately 0.60 g-U/kg-ads. Given that the incremental adsorption of uranium decreases over time, it is likely that the colder temperatures could have a minimal affect on the uptake since they occurred toward the end of the deployment.

The salinity of the ocean test side, shown in figure 11.14c, also varied with tides. Overall, the salinity remained between 31 ppt and 32.5 ppt, with no clear seasonal pattern.

Unfortunately, due to premature battery failure of the current meters from an error in programming upon deployment, the current data does not span the entirety of the deployment. As can be seen from figure 11.14d, which shows currents measured from the instrument near the bottom of the piling (approximately 2 ft from the seafloor), while there were large short term variations in the currents (likely due to tides), overall there were little seasonal changes in the currents. In general, the currents were approximately 10-15 cm/s, with stronger periods of over 80 cm/s at times. Note that the current meters saturate at approximately ± 80 cm/s and therefore readings beyond this are not reliable. The currents seen at this ocean site are much larger than those tested in a lab setting which, to date, have been tested in flow rates of up to 8.24 cm/s (Ladshaw et al., 2017).

11.6.3 Biofouling

Biofouling of the adsorbent fibers can have a detrimental affect on their ability to uptake uranium (Park et al., 2016). One striking result between the two systems was the difference in biofouling. At the end of the 56-day ocean test, the stationary system had a significantly higher amount of biofouling on its shells than the continuously moving system (figure 11.15). Biofouling begins with a thin biofilm and microorganisms followed by the attachment of larger organisms.

To further investigate if the reduced biofouling of the outer shells on the continuous system translated to reduced biofouling on the adsorbent fibers, the weight of the fibers after deployment (which would account for any organism growth) was compared to the weight of the fibers measured before deployment. Figure 11.16 details the percent weight gained or lost by the adsorbent fibers before and after deployment. The results show that in general, for all enclosures and systems, there was a trend toward weight loss in the beginning of the deployed and weight gain by the end of the deployment. The initial weight loss was likely due to the harsh marine environment shedding away some of the adsorbent fibers. On the other hand, the weight gain seen was likely due to biofouling and growth on the adsorbent fibers. However, there was little variation between the weight gained or lost between the different designs or systems.

This point is further illustrated by figure 11.17 which shows the average percent weight gained or lost of the adsorbent fibers in each enclosure and system. As can be seen in the figure, the large standard deviation for all the enclosures suggests there was no significant difference in the weight gained or lost between the different enclosure and system types. This may have been due to the fact that the continuous system was only up for 37% of the deployment, with the majority of its uptime occurring at the end of the 56-day deployment. Considering that biofouling occurs within days to weeks of the adsorbent being placed in the ocean, it is likely that both systems saw about the same colonization of organisms given that the continuous system was not moving in the first few weeks of the ocean trial. Additionally, when the system

Figure 11.15: Biofouling on the (a) stationary net and (b) continuously moving net at the end of the ocean test.

was moving, the colder water temperature likely inhibited biofouling for all fibers, regardless of their enclosure or system.

11.6.4 Water Flow Rate

One of the objectives in the ocean test of the two prototypes was to determine if increased water flow could be achieved by continuously moving ball-chain through the ocean and if that translated to an increase in uranium uptake of the fibers enclosed by the shells on the net. To determine the answer, a novel method using the collection and measurement of radium extracted onto Mn-O_2 impregnated acrylic fibers was developed to quantify the volume of water passing through the fibers. This method was then utilized to quantify the water flow through each of the different types of enclosures, namely the control nylon mesh bag, the two shell designs on each of the two systems.

Preparation of the MnO_2 impregnated acrylic fiber involved a 20 min immersion of raw acrylic fiber into a saturated $KMnO_4$ solution heated to 75° until the fiber turned black. At this point it was removed and rinsed throughly using deionized

water that was previously filtered through MnO_2 impregnated acrylic fibers to remove any radium. The fibers are then stored in damp plastic bags until they are ready to be used. (Moore, 1976).

The MnO_2 impregnated acrylic fibers, which adsorb radium, were placed in a control cartridge, and each of the different types of enclosures. Figure 11.18a shows one of these fibers and figure 11.18b shows the control cartridge used in this experiment. The fibers in each of the different enclosures were in the ocean for approximately 6.5 hours. At the same time, seawater from the same location was pumped up from about mid-depth in the water column to fill a large container in which the control car-

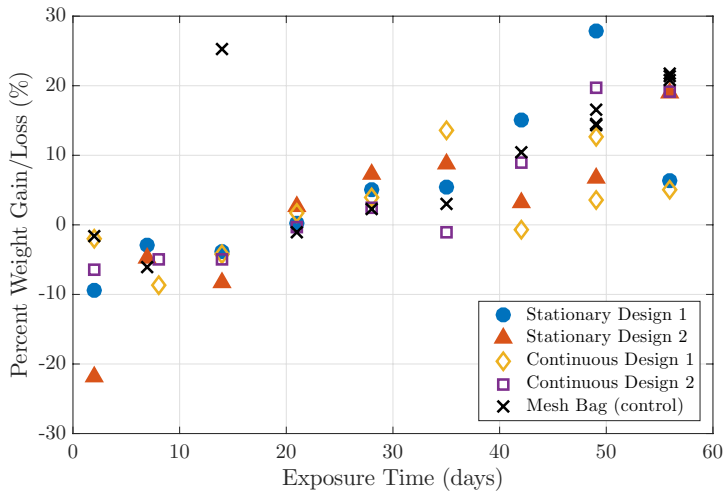

Figure 11.16: Percent weight gain or loss in the adsorbent fibers before and after deployment at each sampling.

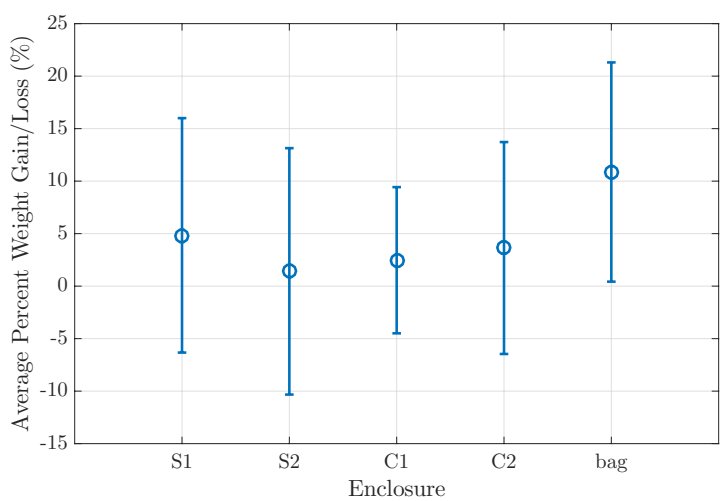

Figure 11.17: Average percent weight gain or loss in the adsorbent fibers for each enclosure and system of all the time-dependent measurements with error bars indicating the standard deviation.

(a) (b)

Figure 11.18: (a) MnO_2 impregnated acrylic fibers used in this study and (b) the control cartridge housing some of these fibers through which a known volume of water was filtered.

(a) *(b)*

Figure 11.19: The ashing process showing (a) one clump of MnO_2 impregnated acrylic fiber in a container ready for ashing and (b) all samples in a muffle furnace prior to ashing.

tridge was placed. A known volume of the water in this container was slowly pumped through the control cartridge at about 1-2 L/min (a rate below 2 L/min has been shown to achieve quantitative radium adsorption (Moore, 1976; Moore et al., 1995)). At the end of the 6.5 hour seawater exposure for all the test enclosures, the water still remaining in the large container to be pumped through the control cartridge was collected in smaller containers and processed at a later time.

After the seawater exposure, following the method of Moore (1984) the fibers were ashed in a muffle furnace at 820°C for 24 hours, resulting in a mass reduction of up to 60% (this step is shown in figure 11.19). After a three-week waiting period, which allows all daughters of ^{226}Ra to grow into equilibrium, the samples were counted for ^{226}Ra using γ-spectrometry by its photopeak at 352 keV.

The known volume of water filtered through the cartridge and the amount of radium adsorbed by the fiber in the control cartridge can be used to determine a relationship between the radium adsorbed and the water flow seen by the fiber. Figure 11.20 shows the results determined using this method after correcting for the differences in the amount of radium fibers initially placed in each of the enclosures and adjusting for weight due to ash loss. The results indicate that there was a significant difference in the water seen by the enclosures on the different systems. In particular, the shells on the continuous system saw the most amount of water flow, whereas the shells on the stationary system saw the least amount. In particular, the continuous

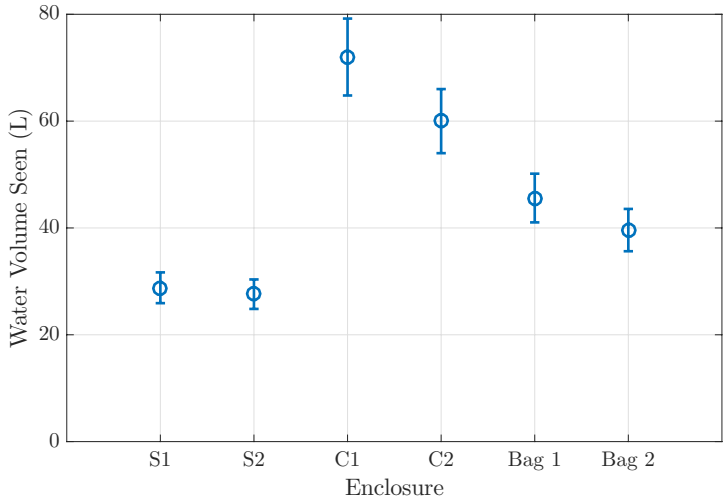

Figure 11.20: Volume of water seen by MnO_2 impregnated acrylic fibers in different enclosure types on different prototype systems as determined by ^{226}Ra count using γ-spectrometry. The control cartridge saw 120 L.

system shells saw approximately 57% more water than the shells on the stationary system and 35% more water than the nylon mesh bags.

However, as indicated by the error bars in figure 11.20, there was no significant difference in the water flow seen by enclosures on the same system. That is, there was no difference in the water seen between the slotted and circular hole designs on the continuous system. As in the flume experiment, these results suggest that the actual design of the shell enclosure has little affect on amount of water flow to the interior. However, there was a significant difference in the water flow seen by the shell enclosures and the mesh bags on the stationary system. Though neither of these types of enclosures was moving, the mesh bags saw 33.8% more water flow than either of the shell designs. The results from the uranium adsorbed from the fibers on the stationary system from the mesh bag and the different shell designs will inform whether or not this increased water flow resulted in more uranium adsorbed, as was hypothesized.

11.6.5 Uranium Uptake

Due to the conservative behavior of uranium in seawater, (Not et al., 2012) all uranium adsorption capacity data was normalized to a salinity of 35 psu to correct for the varying salinity of natural seawater observed in different adsorption experiments. Adsorption kinetics and saturation capacity were determined by fitting time-dependent measurements of adsorption capacity using a one-site ligand saturation model described by (10.1). Figure 11.21 shows the time-dependent measurements of adsorption capacities for all trace metals retained by the AI8 adsorbent for each enclosure. As can be seen in the figure, uranium is not the dominant metal adsorbed by the fiber.

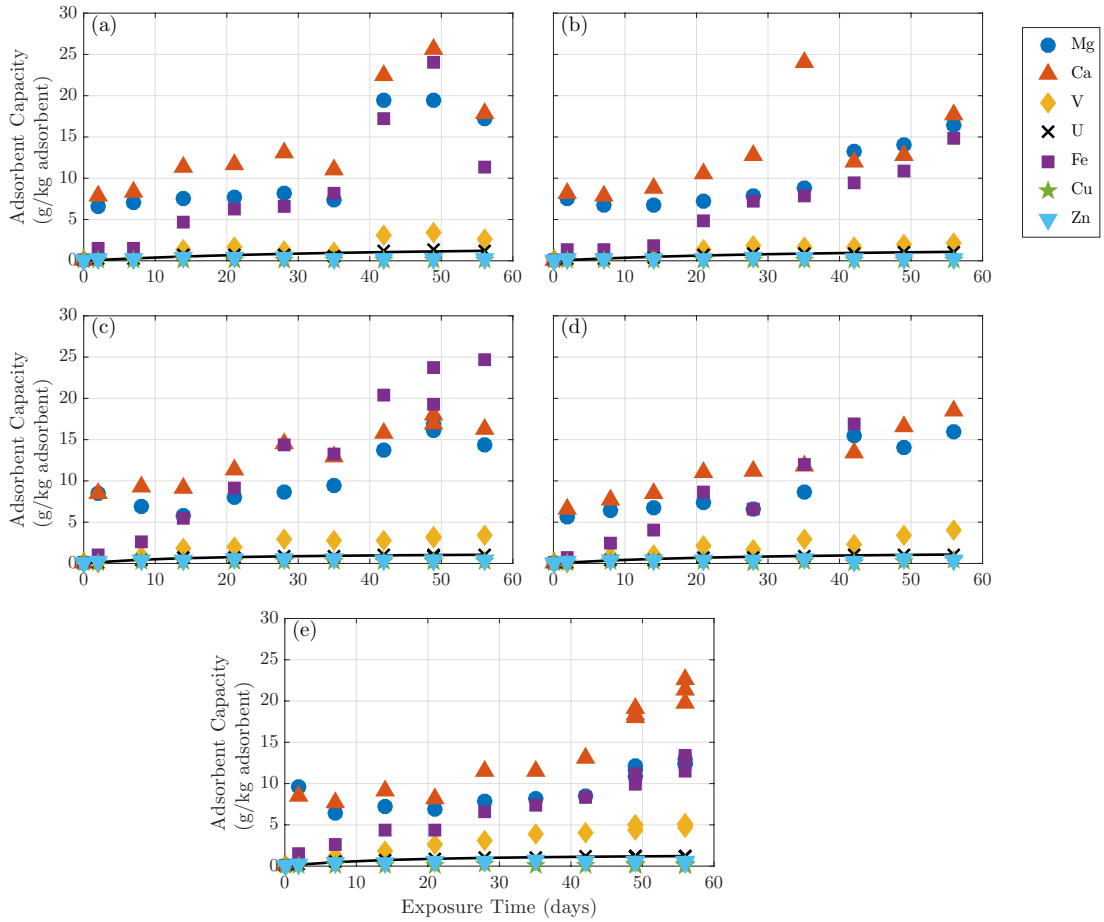

Figure 11.21: Time-dependent measurements of adsorption capacities (g element/kg adsorbent) for several trace elements retained by the ORNL AI8 adsorbent used in the ocean test and enclosed in (a) shells with slotted and (b) circular holes of the stationary system, (c) shells with slotted and (d) circular holes of the continuous system, and (e) in the mesh bag on the stationary system. The black line drawn through the uranium adsorption data represents fitting to a one-site ligand model by (10.1)

The uranium adsorption capacity (g U/kg adsorbent) for all adsorbents in all the enclosures and systems is shown in figure 11.22, with the lines indicating the one-site ligand saturation model fits for each enclosure. As can be seen, there is very little difference in the uranium adsorbed between the different enclosure or system types. This is further confirmed by figure 11.23 which shows the saturation capacity, β_{max}, and half saturation time, K_D, as well as the uptake predicted for an immersion time of 56 days as predicted from the one-site ligand modeling. The error bars detail the $\pm$ 95% confidence intervals of the coefficients. As shown in the figure, there is no significant difference between the coefficients of the fits for each enclosure and system type, suggesting no significant difference in the uranium uptake by the adsorbent in different enclosures and on different systems. This suggests that the system move-

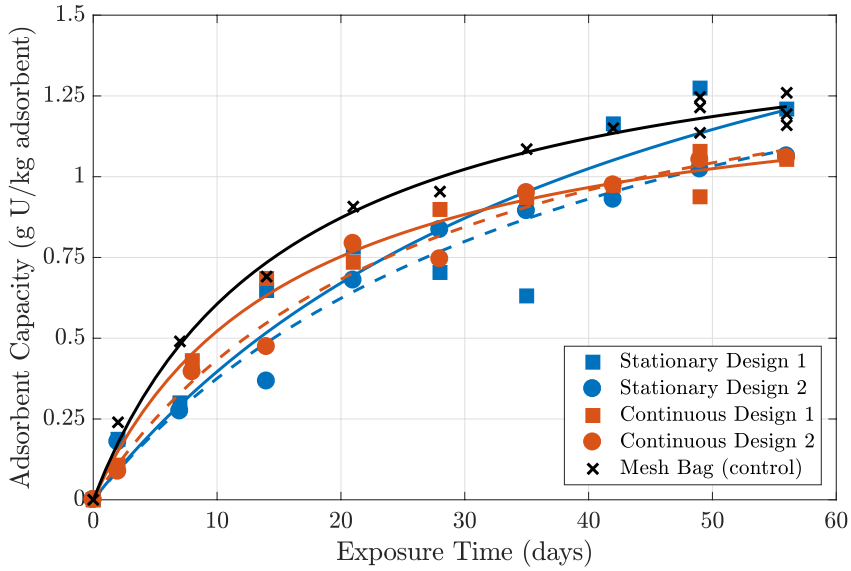

Figure 11.22: Time-dependent measurements of uranium adsorption capacity (g U/kg adsorbent) for the AI8 adsorbent braids enclosed by the different shell designs on the two different systems, and enclosed only by a mesh bag (control). The uranium adsorption capacity was normalized to a salinity of 35 psu. Curves drawn through the data represent fitting to a one-site ligand model by (10.1).

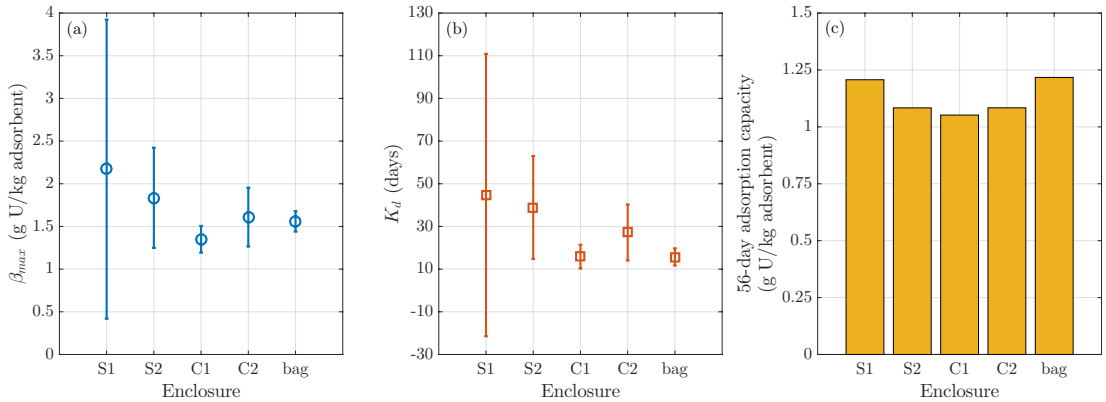

Figure 11.23: The uranium (a) saturation capacity, β_{max}, (b) half saturation time, K_D, and (c) uranium uptake predicted from the one-site ligand model for the adsorbent enclosed different shell designs on the two different systems, and enclosed only by a mesh bag (control).

ment, although increasing water flow to the adsorbent and decreasing biofouling on the shells, may not have helped increase the adsorbent uptake of uranium. This may have been due to the fact that the continuous system was not moving until the last 21 days of the deployment, when the water temperature was colder and towards the end of the deployment, both factors that reduce the uranium uptake of the adsorbent.

This result is further seen in figure 11.24 which shows the total uranium adsorbed

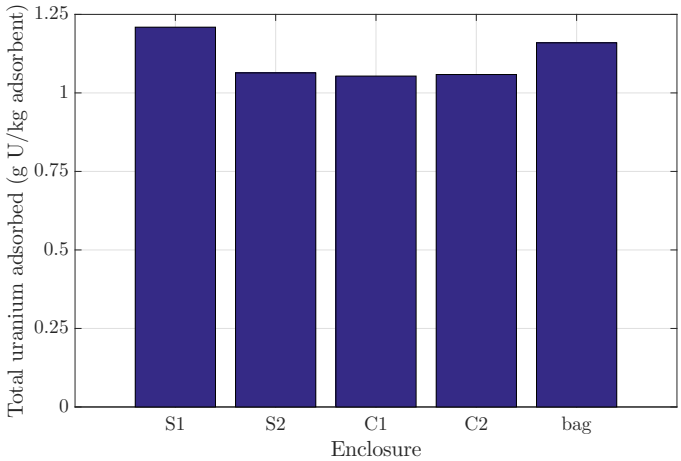

Figure 11.24: The total uranium adsorbed at day 56 by the adsorbent fibers in each enclosure.

(g-U/kg-adsorbent) at day 56 for the adsorbent fibers in each of the different enclosures and systems. The highest uranium uptake was seen by the slotted hole design on the stationary system, which saw a uranium uptake of 1.21 g-U/kg-adsorbent, whereas the same design on the continuous system saw the least amount with 1.06 g-U/kg-adsorbent, and the control with the adsorbent in the mesh bag on the stationary system saw an uptake of 1.16 g-U/kg-adsorbent. The difference in uranium adsorbed by the slotted design on the stationary and continuous systems was only 12.9%, and the difference between the uranium adsorbed by any enclosure and system and the control mesh bag was at most 10%. This suggests again, that there was no significant difference in the uranium adsorbed by fibers in the shells on the different systems as compared to the control, and no significant difference between the uranium adsorbed between the different shell enclosures and systems.

11.7 Discussion

This chapter discussed the design, fabrication, and deployment of two prototypes for the harvesting of uranium from seawater using fiber adsorbents. These prototypes were successfully tested in the ocean off the coast of Massachusetts in collaboration with Massachusetts Maritime Academy for a total of 56-days. Throughout the deployment, adsorbent fibers were sampled from the two different prototypes, and from two different shell designs on each prototype, as well as a nylon mesh bag as a control. Analysis of the uranium adsorbing fibers was conducted by the Pacific Northwest National Laboratory and the radium adsorbent fibers by the Woods Hole Oceanographic Institution.

The results showed that, compared to the stationary system, the continuous system shells saw less biofouling. There may have been a few factors which limited the amount of initial biofilm the formed on the shells of the continuously moving system and hence inhibited larger growth.

The first factor is thought to be that the shells in the continuously moving system were periodically exposed to air. Every 85 seconds, for a period of 20 seconds, the net was exposed to air as it moved over the upper roller. In comparison, the stationary net system was only exposed to air when adsorbent samples were taken, a total of nine times during the 56-day deployment for no more than 10 minutes at a time. This air exposure of the continuous system could have been enough to deter large amounts of growth from microorganisms and hence limited the amount of macrofouling that could have occurred.

Another cause for the marked reduction in biofouling of the continuous system could have been due to the rubbing of the shells against the PVC pipe on the bottom support or the separation guides. Given that the net was inherently buoyant, once it reached the stationary PVC pipe at the bottom of the system, the shells would rub up against the bottom of the pipe as they moved past. Additional rubbing was noted to occur on various points of the separation guides along the length of the bottom support. This rubbing could have inhibited biofouling and even removed any growth that had already accumulated on the shells.

If either of these factors caused a drastic reduction in biofouling, it lends credence to a few design ideas for mitigating biofouling in such a uranium harvester. Specifically, air exposure could be optimized to reduce the likelihood of microorganism growth, while maximizing the amount of water flow seen by the adsorbent. Secondly, a bristle brush could be added at various parts of the structure to gently brush the shells as they pass, further reducing chances of growth. Additionally, UV light has been shown to have strong antibacterial properties (Lakretz et al., 2010). Adding UV LEDs to a point in the adsorbent net's path could also prevent the formation of biofilm and hence reduce biofouling.

Research has also shown that there exists critical values of current speeds for different species of marine organisms above which fouling biomass is greatly reduced and in general fouling is not possible at speeds greater than 1.5 m/s (Railkin, 2003). This suggests that movement of the shell enclosures and adsorbent fibers could also inhibit biofouling growth. However, 1.5 m/s is extremely fast and would likely damage the adsorbent. Hence, more research should be done to determine at which speeds the adsorbent is damaged. Furthermore, research should be done to determine at which speeds biofouling is reduced as a function of immersion time. This will give valuable insight into the design of the SMORE system. For instance, if it is found that speeds of 0.5 cm/s inhibit biofouling for up to 14 days, this can be used to determine the speed of movement of the adsorbent net as well as the frequency of other biofouling mitigation such as moving the net through a series of UV LEDs. Another thought is that the elution bath may also kill all organisms and hence reduce biofouling. Thus, these results could also be used to determine the frequency of elution of the adsorbent.

Although the adsorbent shells of the continuous system such much less biofouling than those on the stationary system, the adsorbent fibers on the shells in both systems saw no significant difference in weight gain. This discrepancy may have been due to the fact that the continuous system was only up for 37% of the deployment, with the majority of its uptime occurring at the end of the 56-day deployment. Considering that biofouling occurs within days to weeks of the adsorbent being placed in the

ocean, it is likely that both systems saw about the same colonization of organisms given that the continuous system was not moving in the first few weeks of the ocean trial. Additionally, when the system was moving, the colder water temperature likely inhibited biofouling for all fibers, regardless of their enclosure or system.

The ocean trial described in this chapter also employed a novel method using the radium adsorbed by MnO_2 impregnated acrylic fibers was used to quantify the water flow seen within all the enclosures. The results showed no significant difference in the water flow both shell designs on the same system, however the continuous system shells saw more water flow than the stationary system shells and control bags. This suggests that movement does in fact increase the water flow seen by the adsorbent and that the design of the shell enclosure makes little difference on uptake of the adsorbent inside.

Moreover, the results of the uranium adsorbed by the fibers in each of the shell enclosures and systems showed no significant difference in the uptake of the fibers. Although the shells on the continuous system saw the most water flow, this did not translate into increased uranium uptake. Again, as with the biofouling of the fibers, this may have been due to the fact that the continuous system was not moving reliably until the last few weeks of the test, when the water temperature was colder and towards the end of the deployment, both factors that reduce the adsorbent's uptake. Additionally, results from Ladshaw et al. (2017) suggest that for flow rates of > 5.52 cm/s the uptake of the adsorbent will no longer increase with increasing velocity. If this is the case, given that the ocean currents are usually > 5.52 cm/s, the increased water flow to the continuously moving shells will likely not translate to an increase in uranium uptake by the adsorbent fiber.

SMORE Hydrodynamic Response

This chapter details the hydrodynamic response of a full-scale Symbiotic Machine for Ocean uRanium Extraction. Given that the device is hypothesized to be coupled to a floating offshore wind turbine, it is extremely important that the addition of the uranium harvester device does not adversely affect the hydrodynamic response of the offshore wind turbine. This work was done in collaboration with Jocelyn Kluger (Kluger, 2017).

12.1 Theory

As mentioned in chapter 10, because offshore wind turbine data is proprietary and often very difficult to use for public work, the present design for SMORE utilizes the StatOil OC3-Hywind spar with a 5-MW NREL turbine, a device well documented by NREL (Jonkman et al., 2009; Jonkman, 2010).

The problem set up is shown in figure 12.1. The hydrodynamics of the floating spar buoy are considered in head-on incident waves of amplitude A and frequency ω. These result in coupled degrees of freedom in heave, X_3, surge, X_1, and pitch, X_5, taken about the still water line (SWL).

The linear equations of motion of the system are given by

$$(\mathbf{M} + \mathbf{A})\ddot{\xi} + \mathbf{B}\dot{\xi} + \mathbf{C}\xi = \mathbf{X}(t), \tag{12.1}$$

where $\mathbf{M}$ is the mass matrix, $\mathbf{A}$ is the added mass coefficient matrix, $\mathbf{B}$ is the linear damping coefficient matrix, $\mathbf{C}$ is the restoring coefficient matrix, ξ is the turbine displacement, and $\mathbf{X}$ is a matrix of the hydrodynamic excitation forces and moments.

Utilizing a linear frequency-domain analysis, the exciting forces and moments due to plane progressive waves will be assumed to be of the form

$$X_j(t) = \Re\left\{\mathbb{X}_j(\omega)e^{i\omega t}\right\}, \quad \text{for } j = 1, \ldots, 6 \tag{12.2}$$

where $\mathbb{X}_j(\omega)$ is a complex quantity. By virtue of linearity, the turbine's response to wave excitation will be of the form

$$\xi_j(t) = \Re\left\{\Xi_j(\omega)e^{i\omega t}\right\}, \quad \text{for } j = 1, \ldots, 6, \tag{12.3}$$

where $\Xi_j(\omega)$ is a complex quantity. Combining (12.1)-(12.3) yields the following equations of motion in the frequency domain

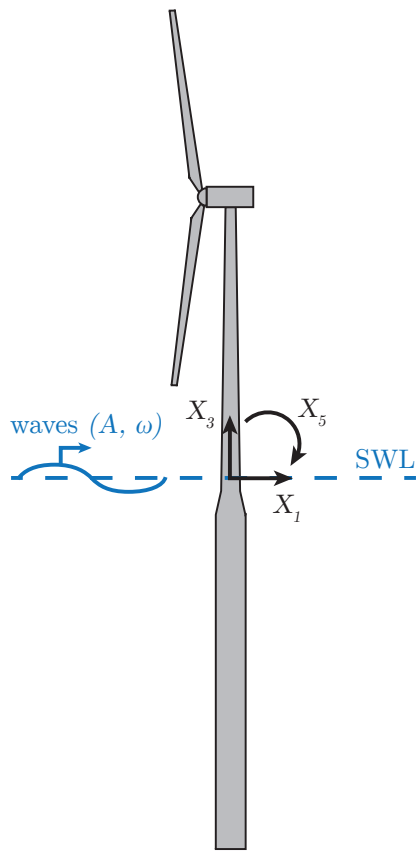

Figure 12.1: Floating spar wind turbine, similar to that of the NREL 5-MW wind turbine mounted on the OC3-Hywind spar (Jonkman et al., 2009; Jonkman, 2010) with incident waves of amplitude A and frequency ω. The motions of the turbine are described about the still water line (SWL).

$$\left[-\omega^2(M_{ij} + A_{ij}(\omega)) + i\omega B_{ij}(\omega) + C_{ij}\right] \Xi_j(\omega) = \mathbb{X}_i(\omega). \tag{12.4}$$

The principal seakeeping quantity from a linear seakeeping analysis of a floating body at zero speed is the Response Amplitude Operator (RAO), defined as

$$RAO_j(\omega) = \left|\frac{\Xi_j(\omega)}{A/R^n}\right|, \tag{12.5}$$

where R is the turbine radius, $n = 0$ for $j = 1, 3, 5$ and $n = 1$ for $j = 2, 4, 6$.

For the case of an arbitrary shape such as an offshore wind turbine, it is common practice to examine the dynamic response numerically. Jonkman (2010) conducted a numerical study of the hydrodynamic response of the OC3-Hywind spar buoy using the WAMIT computer program (Newman and Sclavounos, 1988; Lee and Newman, 2006). This program uses a three-dimensional numerical-panel method in the frequency domain to solve response of the turbine to linear wave forcing due to potential flow. The excitation force and RAOs determined by Jonkman (2010) will be used as

comparison for the results of the excitation forces and RAOs found in the experiment detailed in this chapter.

12.2 Experimental Setup

This experiment was done in collaboration with Jocelyn Kluger, which did the vast majority of the experimental set-up (Kluger, 2017). This section details the scaling of the designs for testing, the experimental facilities used, and the experimental methods used to determine the excitation forces and response amplitude operators.

12.2.1 Model scaling

A 1:150 Froude scaled model of two different versions of SMORE and the reference floating wind turbine were developed for testing to determine the wave excitation forces on the structure as well as each design's response. The Froude number is a dimensionless number that describes a ratio of the flow inertia to the external field and is given by

$$Fr = \frac{U}{\sqrt{gL}}, \tag{12.6}$$

where U is the characteristic velocity, g is acceleration due to gravity, and L is a corresponding characteristic length. The geometric scale, λ is defined to be

$$\lambda = \frac{L_f}{L_m}, \tag{12.7}$$

where L_f is the full-scale characteristic length and L_m is the model scale characteristic length. For this experiment, $\lambda = 150$. Matching the model and full-scale Froude numbers amounts to

$$Fr_f = Fr_m \tag{12.8}$$

$$\frac{U_f}{\sqrt{gL_f}} = \frac{U_m}{\sqrt{gL_m}} \tag{12.9}$$

$$\Rightarrow U_m = U_f\sqrt{\frac{L_m}{L_f}} = U_f\sqrt{\frac{1}{\lambda}}. \tag{12.10}$$

Hence, the full-scale velocity is scaled by $\sqrt{\lambda}$ to achieve the model scale velocity. This process can be repeated to determine the scale ratio between the model scale and full-scale of various important physical parameters, such as mass, acceleration, and force. Table 12.1 details the scale ratios for many of the physical parameters utilized in this experiment. For instance, while acceleration varies only by a ratio of 1 between the model and full scale, the force scales by a factor of λ^3 (Chakrabarti, 1994).

Table 12.1: Scaling ratios for various physical parameters

Variable	Dimensions	Units	Scale Ratio
Length	L	m	λ
Mass	M	kg	λ^3
Angle	none	rad	1
Acceleration	L/T^2	m/s^2	1
Angular Acceleration	$1/T^2$	$1/s^2$	λ^{-1}
Angular Velocity	1/T	1/s	$\lambda^{-0.5}$
Force	$(M\times L)/T^2$	$kg\times m/s^2$	λ^3
Wave Height	L	m	λ
Wave Period	T	m	$\sqrt{\lambda}$
Velocity	L/T	m/s	$\sqrt{\lambda}$
Moment of Inertia	$M\times L^2$	$kg\times m^2$	λ^5

12.2.2 Models for testing

As mentioned, two designs of SMORE were developed for testing, in addition to a scale model of the reference floating wind turbine. The reference floating wind turbine was scaled from dimensions detailed by Jonkman et al. (2009) and Jonkman (2010). Some of the key parameters and their full-scale and model values are detailed in table 12.2, as determined from Jonkman (2010) and Myhr et al. (2014).

The model scale reference floating wind turbine was fabricated using aluminum cylinders turned down to the diameters of the upper and lower turbine spar, an aluminum tube for the turbine tower, a circular plate to simulate the rotor damping on the turbine, and a transition region 3D printed from acrylonitrile butadiene styrene. All holes and joints were made waterproof using Permatex® Sensor-Safe Blue RTV Silicone Gasket Maker.

It was thought that a SMORE design such as that described in chapter 10 in which the upper platform with the top rollers were out of the water could have significant

Table 12.2: Scaling factors employed for wave model testing

Variable	Unit	Full-Scale	Model Scale
Total draft	m	120	0.8
Tower height	m	77.6	0.52
Depth to Top of Taper Below SWL	m	4	0.027
Depth to Bottom of Taper Below SWL	m	12	0.080
Diameter Above Taper	m	6.5	0.043
Diameter Below Taper	m	9.4	0.063
Platform Mass	kg	1700000	0.5
Tower Mass	kg	249718	0.074
Ballast	kg	5766000	1.71
CM Location Below SWL	m	89.92	0.60

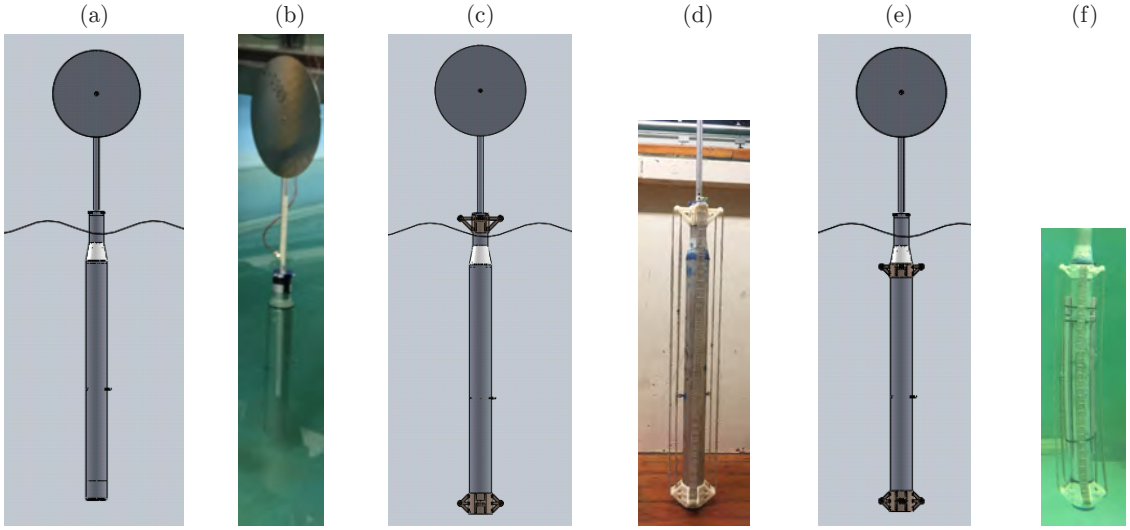

Figure 12.2: Three-dimensional solid models and fabricated designs for the reference floating wind turbine, (a) and (b), the SMORE design with the upper platform out of the water, (c) and (d), and the SMORE design with the upper platform submerged, (e) and (f).

risks due to the wave loads near the surface. Given that the wave energy decays exponentially with depth, placing the upper platform underneath the water surface could be one way to mitigate these risks. Therefore, in addition to the reference floating wind turbine, two SMORE designs were tested. In the first, the top set of rollers was placed out of the water at 0.03 m above the SWL (corresponding to 4.5 m in a full-scale design). In the second design, the top set of rollers was submerged 0.12 m below the SWL (corresponding to 18 m in a full-scale design). Figure 12.2 shows the three-dimensional models and fabricated designs used for testing.

For the SMORE designs, The adsorbent ball-chain net was modeled using 3 mm diameter (#6 trade size) nickel-plated steel bead chain and the upper and bottom platforms of rollers were 3D printed out of acrylonitrile butadiene styrene. At every five beads, the chains were hot-glued together to mimic the increased rigidity that would be provided by rope cross-members of the ball-chain net. Because 3 mm diameter bead-chain was not available in plastic, the bead-chain net added extra weight to the model than would be seen in the full-scale version. Therefore, strips of foam were added along the length of the turbine to increase its buoyancy and ensure it had a draft of approximately 0.8 m. By adding the foam strips along the length of the turbine, they mimicked the additional buoyancy that plastic shells with polymer adsorbents would provide to the overall structure. Additionally, the strips were added to the turbine in such a way as to limit the effects of the changed geometry on the turbine's hydrodynamic coefficients.

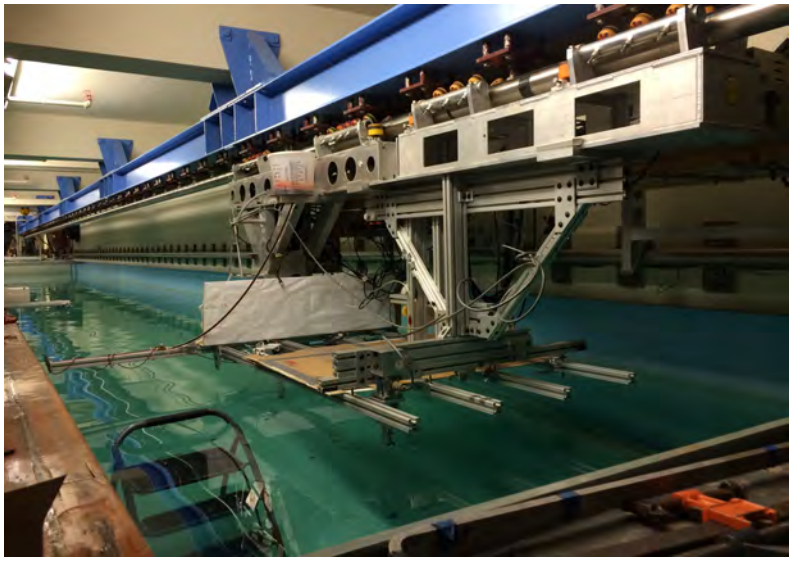

Figure 12.3: MIT Tow Tank where scale model hydrodynamic response tests were conducted of two designs of SMORE and the reference floating wind turbine.

12.2.3 Experimental facilities

The tests described in this chapter were conducted in the MIT Tow Tank, shown in figure 12.3, which is 30.5 m long, 2.1 m wide, and 1.2 m deep (100 ft long, 8 ft wide, and 4 ft deep) with a wave maker. The wave maker is a hydraulically driven vertical paddle with controllable amplitude and frequency that are programmed using LabView.

As shown in figure 12.4, two wave probes were used to measure the amplitude of the passing waves. One probe was located approximately at mid-width in the tank 11.9 m (39.17 ft) downstream of the wave maker and another was located approximately 9.5 m (31 ft) downstream of the wave maker, closer to one of the walls of the tank. The models for testing were located about half-way down the length of the tank.

12.2.4 Excitation Forces

In order to measure the excitation forces on the designs, the models were constrained by a set of three load cells in the configuration shown in figure 12.5. All load cells were SMT Overload Protected S-Type Load Cells. The heave load cell was rated to 5 lbf ($\sim$ 22.24 N) and the top and bottom surge load cells were rated to 2.2 lbf ($\sim$ 9.79 N). Stinger rods measuring 24 mm and 12 mm connected the bottom and top surge, and heave load cell to the turbine tower, respectively. Each load cell was connected to a LabView data acquisition unit through a DC powered FUTEK amplifier module to increase the signal readings. The load cells were powered with a stacked dual power supply outputting $\sim$20.7 V for all trials. The bottom surge load cell was approximately 0.057 m above the SWL and the top surge load cell was 0.24

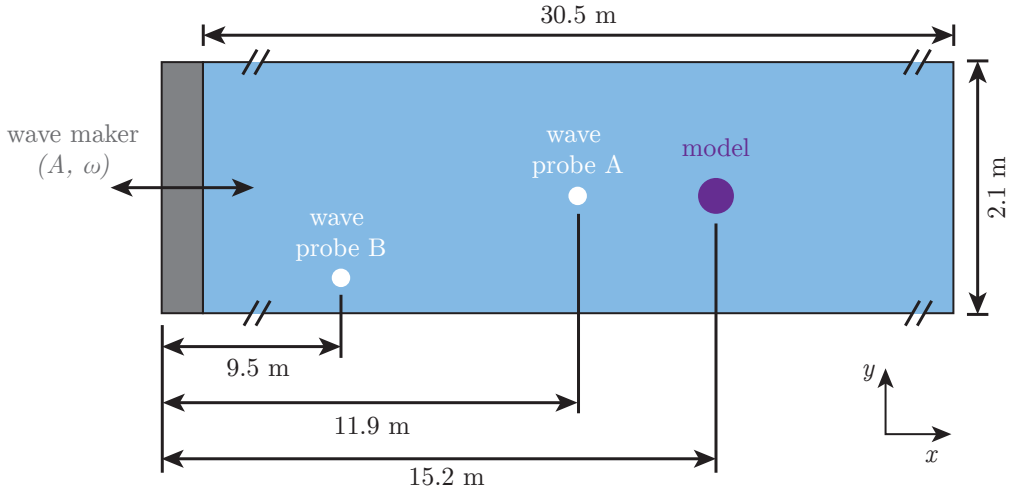

Figure 12.4: Schematic of the experimental configuration. The wave maker on the left was excited at an amplitude, A, and frequency ω. Two wave probes (white dots) downstream measured the amplitude incoming to the model (purple) for all tests.

m above the SWL. The surge force was taken to be the sum of the readings of the top and bottom load cells. The resulting pitch torque was determined by

$$X_5 = X_{1,top} z_{top} + X_{1,bottom} z_{bottom}, \tag{12.11}$$

where $X_{1,top}$ and $X_{1,bottom}$ are the top and bottom surge force load cell readings, respectively, and z_{top} and z_{bottom} are the distances of the load cells to the SWL, respectively.

In order to obtain frequency dependent data for both the wave excitation forces and response amplitude operators, the wave maker was excited at various frequencies and amplitudes for each model test. The wavemaker parameters used for the excitation force measurement experiment are detailed in table 12.3 where the amplitude was measured by the wave probe. The wavemaker was programed to excite waves for 20 periods for all tests. Because the wave excitation force varies with frequency, ω, the load cell data were filtered using a Fast-Fourier Transform to obtain the amplitude of the forces at the frequency of interest.

12.2.5 Response Amplitude Operators

To determine the response amplitude operators of the models, tests were conducted in which the models were freely floating and an accelerometer mounted to the tower of the turbine measured heave, surge, and pitch motions. The accelerometer used in this setup was a SparkFun 9 Degree of Freedom Sensor Stick, utilizing the LSM9DS1 motion-sensing system-in-a-chip which required an operating voltage of 3.3V. The accelerometer was configured to measure ± 2 g in acceleration and ± 245 deg/s in angular velocity using a Teensy 3.2 USB development board powered through a laptop USB port. The experimental setup is shown in figure 12.6.

Table 12.3: Parameters for Excitation Force Experiment

	Amplitude (m)					
	FWT Alone		**SMORE Above**		**SMORE Below**	
Frequency (Hz)	**Small**	**Large**	**Small**	**Large**	**Small**	**Large**
0.4		0.0088	0.0068	0.0138	0.007	0.014
0.5	0.0023	0.0079	0.0069	0.0088	0.0069	0.01
0.6	0.0131		0.0139	0.03	0.0122	0.024
0.7	0.0087	0.0162	0.0076	0.015	0.0078	0.0151
0.8	0.0096	0.0175	0.008	0.0187	0.009	0.0175
1.1	0.0101	0.0211	0.0051	0.0216	0.0109	0.0207
1.6	0.0096	0.0154	0.01	0.0161	0.0109	0.0144

Because the accelerometer was mounted above the SWL, the measurements had to be translated by

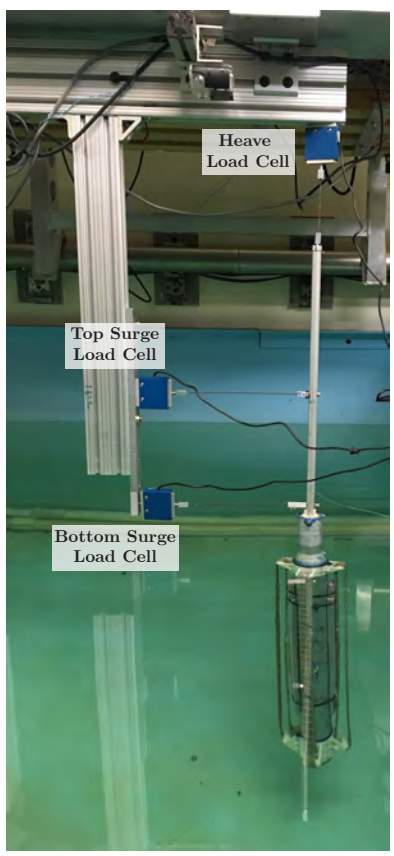

Figure 12.5: Experimental setup of the excitation force test. One load cell was used to measure heave and two were used to measure surge. The difference in measurement of the two surge load cells and their distance from the SWL was used to determine the pitch torque.

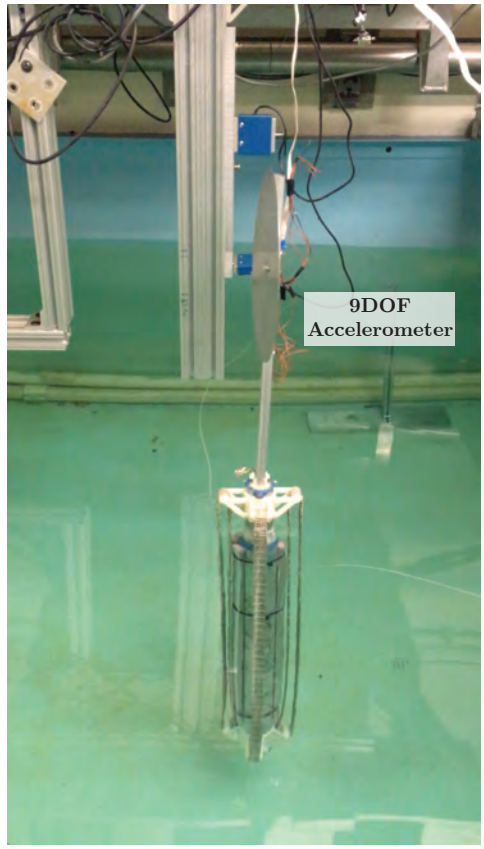

Figure 12.6: Experimental setup of the RAO test. A 9DOF accelerometer mounted to the tower of the turbine was used to measure heave, surge, and pitch motions.

$$\mathbf{a}^{\mathrm{SWL}} = \mathbf{a}^{0} + \boldsymbol{\omega}^{\mathrm{T}} \times \left(\boldsymbol{\omega}^{\mathrm{T}} \times \mathbf{r}^{0,\mathrm{SWL}}\right) + \boldsymbol{\alpha}^{\mathrm{B}} \times \mathbf{r}^{0,\mathrm{SWL}}, \tag{12.12}$$

where $\mathbf{a}^{\mathrm{SWL}}$ is the acceleration of the turbine at the SWL, $\mathbf{a}^{0}$ is the acceleration of the turbine measured at the accelerometer, $\boldsymbol{\omega}^{\mathrm{T}}$ is the angular acceleration of the turbine as measured by the accelerometer, $\mathbf{r}^{0,\mathrm{SWL}}$ is the position vector from the location of the accelerometer to the SWL, and $\boldsymbol{\alpha}^{\mathrm{T}}$ is the angular acceleration of the turbine, as determined from the accelerometer. Note that because the turbine is assumed to be a rigid body, the angular velocity, $\boldsymbol{\omega}^{\mathrm{T}}$, and angular acceleration, $\boldsymbol{\alpha}^{\mathrm{T}}$ are the same at all points on the body.

In order to obtain frequency dependent data for the response amplitude operators, the wave maker was excited at various frequencies and amplitudes for each model test. The test parameters used for the RAO determination experiment are detailed in table 12.4 where the amplitude was measured by the wave probe. The wavemaker was programed to excite waves for 20 periods for all tests. Given that the response amplitude operator is a function of frequency, ω, the acceleration and angular velocity data were filtered using a Fast-Fourier Transform to obtain the amplitude of the response at the frequency of interest.

Table 12.4: Parameters for RAO Experiment

	Amplitude (m)						
	FWT Alone			SMORE Above		SMORE Below	
Frequency (Hz)	**Small**	**Medium**	**Large**	**Small**	**Large**	**Small**	**Large**
0.4	0.004			0.0069	0.0138	0.0069	0.0135
0.5	0.0046		0.0063	0.0072	0.009	0.0068	0.0074
0.6	0.005	0.0054	0.0163	0.0128	0.0273	0.0147	0.0286
0.7	0.0074	0.0115	0.0121	0.0079	0.0166	0.0079	0.0154
0.8	0.0089	0.0154	0.0229	0.0092	0.0196	0.0092	0.0183
1.1	0.0107	0.0179	0.0272	0.0109	0.0209	0.008	0.0184
1.6	0.0113	0.0172	0.0232	0.0103	0.016	0.0098	0.0162

12.3 Results

The results for the excitation force and RAOs for all models tested are shown and discussed in this section. All experimentally determined results are compared to the numerical results determined by Jonkman (2010) for the case of the unmodified, reference wind turbine.

12.3.1 Excitation Forces

Surge Excitation Force

Figure 12.7 shows the full-scale surge excitation force for the reference turbine, SMORE with the upper platform above the water, and SMORE with the upper platform submerged. In the case of the unmodified wind turbine, the surge excitation force is slightly increased as compared to that determined numerically by Jonkman (2010).

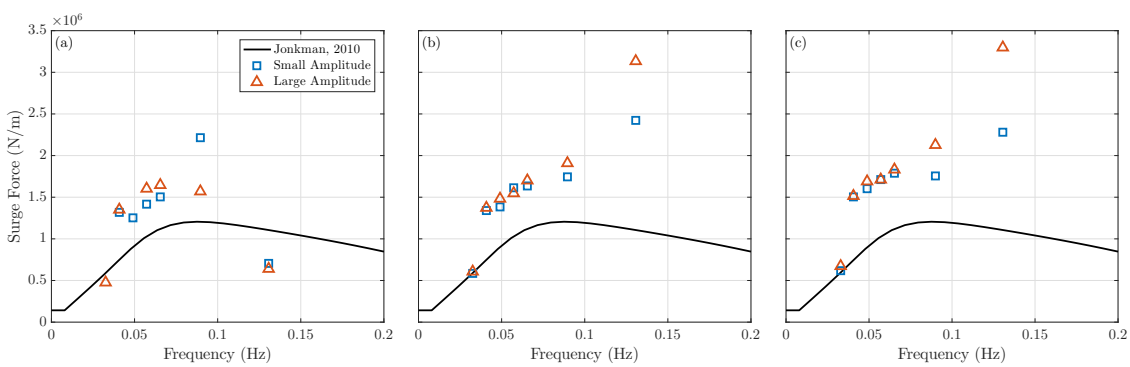

Figure 12.7: Full-scale surge excitation force as determined by the load cell tests for small (blue squares) and large (red triangles) amplitude waves as compared to that numerically determined by Jonkman (2010) (black line) for the (a) reference floating wind turbine, (b) SMORE design with the upper platform above the water, and (c) SMORE design with the upper platform submerged.

This discrepancy could be due to slight differences in the model turbine's properties as compared to the full scale turbine. For instance, the data from Jonkman (2010) mentions the platform mass, including ballast to be 7466 tonnes. Myhr et al. (2014) details the platform uses 1700 tonnes of steel, therefore it was assumed the difference in mass, 5766 tonnes, was ballast in the turbine, which may not actually be the case. Although the magnitude of the surge excitation force is increased for the experimentally tested turbine as compared to those determined numerically, the trends are consistent between the experimentally and numerically determined surge excitation force. Additionally, there is good agreement in the excitation force for waves of different amplitudes excited at the same frequency, as expected.

For the case of both SMORE (figure 12.7b) with the upper platform out of the water and with the platform submerged (figure 12.7c), the surge excitation force is in good agreement with that experimentally measured in the reference floating wind turbine test (figure 12.7a). This suggests that the SMORE design with the upper platform above the water surface does not have significantly difference excitation forces as those acting on the unmodified wind turbine.

Heave Excitation Force

As seen in figure 12.8a, there is excellent agreement in the heave excitation force for the unmodified turbine as determined numerically by Jonkman (2010) and measured by the load cells. The experimentally determined heave excitation force for SMORE with the upper platform above the water (figure 12.8b) agrees well with the heave excitation force for the unmodified turbine both determined experimentally and by Jonkman (2010). On the other hand, the heave excitation force of SMORE with the upper platform submerged (figure 12.8c) shows an increase in the full-scale heave excitation force compared to those both determined experimentally for the unmodified turbine (figure 12.8a) and those found by Jonkman (2010). This is expected as the

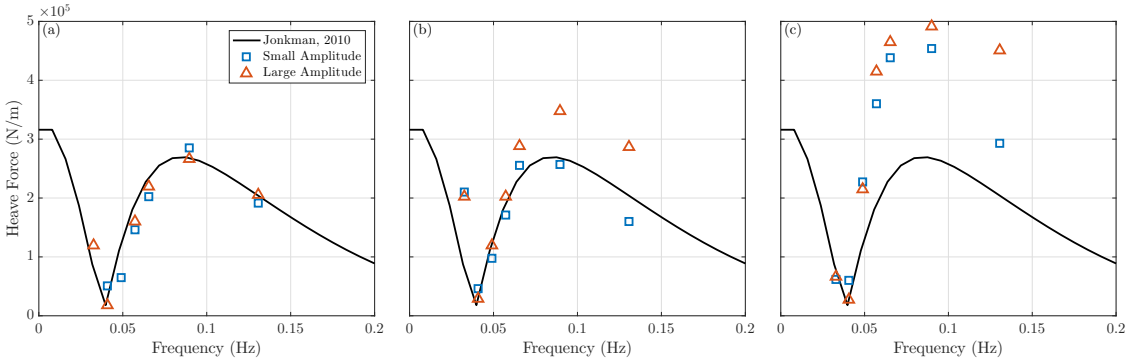

Figure 12.8: Full-scale heave excitation force as determined by the load cell tests for small (blue squares) and large (red triangles) amplitude waves as compared to that numerically determined by Jonkman (2010) (black line) for the (a) reference floating wind turbine, (b) SMORE design with the upper platform above the water, and (c) SMORE design with the upper platform submerged.

submerging of the upper platform adds a significant amount to the water plane area of the system and hence affects the heave hydrostatic restoring force. Although the heave excitation force is increased, the same trend for the case of this SMORE design as with the unmodified turbine can be seen, suggesting that the dominant excitation frequencies remain the same.

Pitch Excitation Torque

Similarly to the experimentally determined surge excitation force, the and pitch excitation torque for the unmodified turbine (figure 12.9a) is slightly increased as compared to that determined numerically by Jonkman (2010). Because the surge and pitch motions of a floating wind turbine are coupled, this discrepancy is likely due to the same reason the measured surge excitation force is larger than that predicted Jonkman (2010). Although the magnitude of the pitch excitation torque is increased for the experimentally tested turbine as compared to that determined numerically, the trends are consistent between the experimentally and numerically determined pitch excitation torque.

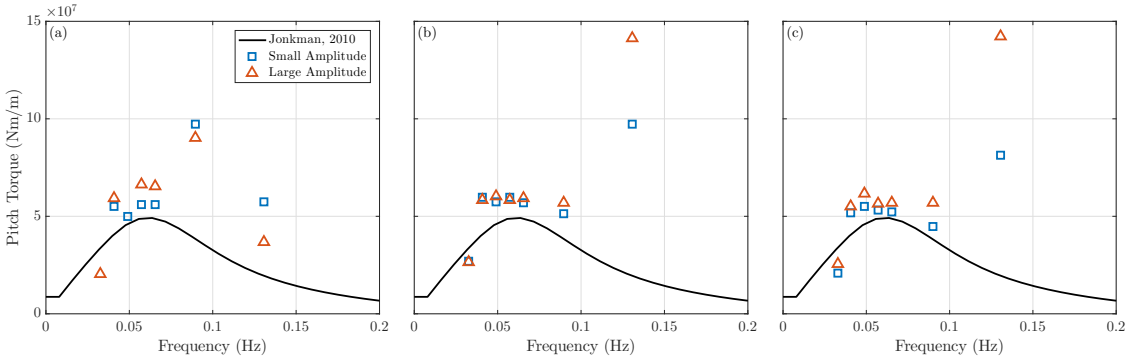

Figure 12.9: Full-scale pitch excitation torque as determined by the load cell tests for small (blue squares) and large (red triangles) amplitude waves as compared to that numerically determined by Jonkman (2010) (black line) for the (a) reference floating wind turbine, (b) SMORE design with the upper platform above the water, and (c) SMORE design with the upper platform submerged.

12.3.2 Response Amplitude Operators

Surge RAO

For the unmodified floating wind turbine, the experimentally determined surge RAO (figure 12.10a) is slightly increased from that determined numerically by Jonkman (2010). The surge RAO for both SMORE with the upper platform above the water (figure 12.10b) and SMORE with the upper platform submerged (figure 12.10c) show good agreement with the experimentally determined surge RAO for the unmodified turbine. This suggests that the surge response of the turbine is unaffected by the addition of either SMORE design.

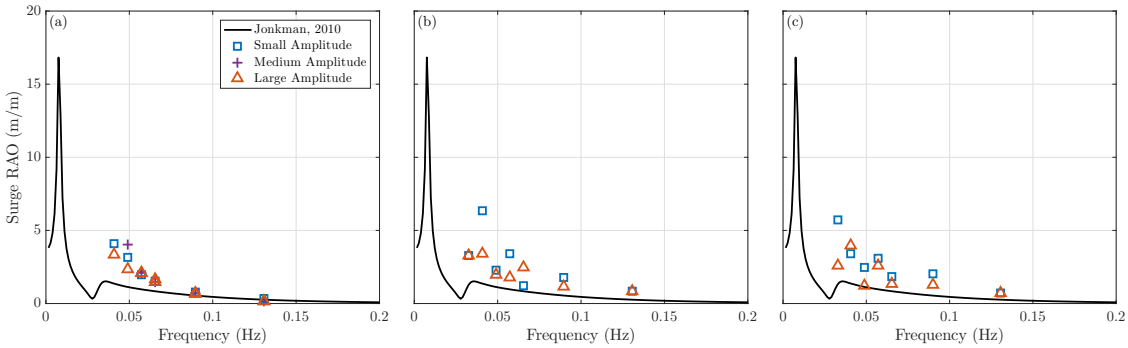

Figure 12.10: Full-scale surge RAO as determined by the accelerometer tests for the (a) reference floating wind turbine, (b) SMORE with the upper platform above the water, and (c) SMORE with the upper platform submerged, for small (blue squares), medium (purple crosses) and large (red triangles) amplitude waves as compared to that numerically determined by Jonkman (2010) (black line).

Heave RAO

In the case of the heave RAO, the unmodified floating wind turbine experimentally determined response agrees extremely well with that numerically determined by Jonkman (2010) (figure 12.11a). The SMORE design with the upper platform above the water also exhibits a similar heave response (figure 12.11b), suggesting the addition of this type of SMORE design does not affect the turbine's heave motion. On the other hand, the heave response is slightly decreased for the SMORE design with the upper platform submerged (figure 12.11c) from that determined by Jonkman (2010). This is likely due to the additional damping in heave provided by all of the submerged structures on the floating wind turbine.

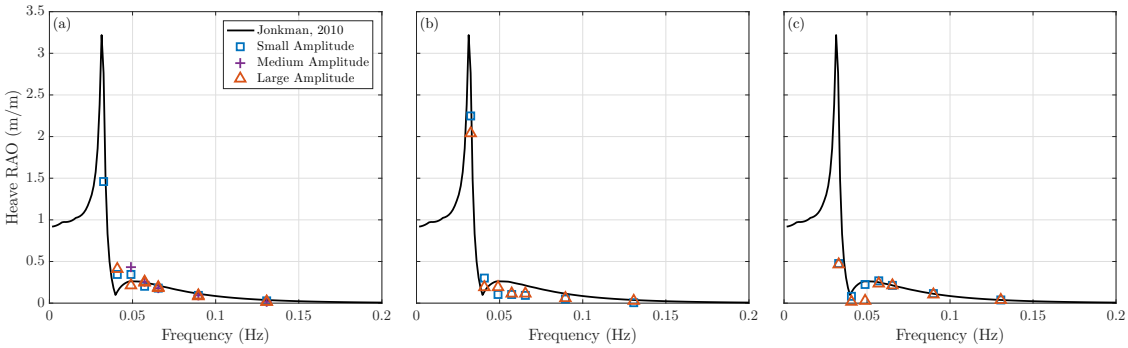

Figure 12.11: Full-scale heave RAO as determined by the accelerometer tests for the (a) reference floating wind turbine, (b) SMORE with the upper platform above the water, and (c) SMORE with the upper platform submerged, for small (blue squares), medium (purple crosses) and large (red triangles) amplitude waves as compared to that numerically determined by Jonkman (2010) (black line).

Pitch RAO

As with the heave RAO, the unmodified wind turbine's measured pitch RAO (figure 12.12a) agrees well with that determined numerically by Jonkman (2010). The same is true for the pitch RAO for the SMORE design with the upper platform submerged (figure 12.12c), suggesting this modification to the turbine does not affect its pitch motions. On the other hand, the upper platform above the water shows a decrease in the pitch response, especially near the pitch resonant frequency for the unmodified turbine (figure 12.12b). This is likely due to the additional roller platform near the bottom of the turbine which acts to increase the restoring pitch torque.

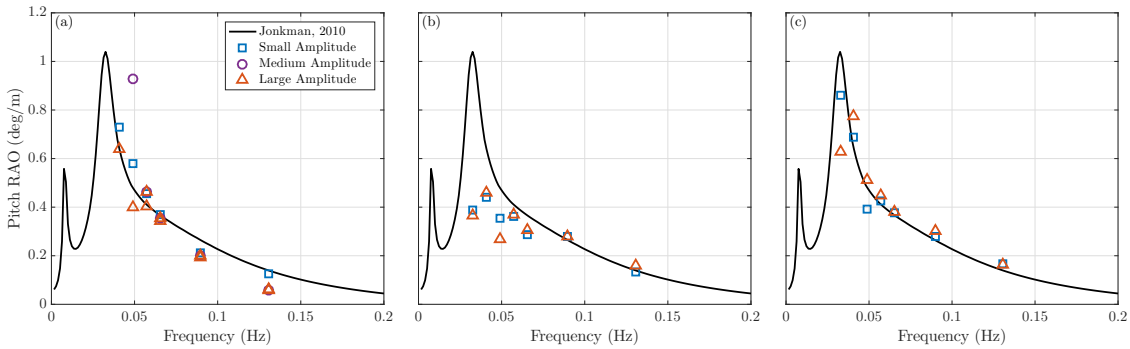

Figure 12.12: Full-scale pitch RAO as determined by the accelerometer tests for the (a) reference floating wind turbine, (b) SMORE with the upper platform above the water, and (c) SMORE with the upper platform submerged, for small (blue squares), medium (purple crosses) and large (red triangles) amplitude waves as compared to that numerically determined by Jonkman (2010) (black line).

12.4 Discussion

The results of the model testing of various SMORE designs indicate that for both designs, one in which the upper platform is out of the water and another in which it is submerged, there is little effect on the overall hydrodynamics of the wind turbine to which the uranium harvester is attached. While the magnitude of the excitation forces or turbine response to these waves may vary from an unmodified wind turbine, in general the variations are minor. Furthermore, the resonant peaks of the turbine response are not affected by the addition of either of the SMORE systems. This is key because an offshore wind turbine is tuned such that its resonant frequencies for various motions will be out of the frequency of storms. The resonant frequencies of the unmodified turbine are in the very low frequency range (0.0077-0.0313 Hz, ∼0.04-0.3 rad/s), for which there is little energy in typical ocean spectra. The addition of either SMORE design does not impact this resonant frequency.

Although both SMORE designs do not affect the dynamics of the turbine they are attached to, other considerations should be taken into account when determining the design of SMORE. Specifically, a SMORE design with the upper platform submerged

may have added benefits like reduced light and air contact on the adsorbent, which could translate to reduced biofouling. Additionally, submerging the upper platform to below the ocean surface could greatly reduce wave loads on the uranium harvester since wave forcing decreases exponentially with depth. On the other hand, designing a chemical system to extract uranium from the adsorbent for SMORE with a submerged upper platform will likely be more difficult than if the platform were above the water. These considerations must be further investigated before designing a system for a large-scale pilot study.

SMORE Cost-Analysis

This chapter describes the economic analysis technique used to determine the uranium production cost for previous deployment strategies (Schneider and Sachde, 2013; Schneider and Linder, 2014; Byers and Schneider, 2015; Byers, 2015; Byers et al., 2016; Haji et al., 2017). It is then used to analyze the uranium production cost from a SMORE device. The resulting cost is compared to that from the reference deployment scheme (which has been used as the base case for cost estimates to date). All costs are presented in 2015 dollars. The technique used in this chapter is described in detail by Byers (2015) and the work presented in this chapter was done in collaboration with Dr. Erich Schneider and Maggie Flicker Byers from the University of Texas at Austin.

13.1 Discounted Cash Flow Methodology

The economic cost analysis considers the deployment strategy to consist of three steps. In the first step, the adsorbent is produced using radical polymerization. Next, it is fabricated into either a braid (for the reference deployment scheme) or filament balls (for SMORE and any other strategies in which a shell is used to enclose the adsorbent) and deployed. In the third step (also referred to as the back end), a chemical bath is used to elute the uranium and other metal ions from the polymer. The costs of these three steps are considered individually and then summed and the steps are repeated until it is no longer economically effective to do so.

For each of the three steps, the capital, operating, and decommissioning costs are evaluated, resulting in a timeline of when costs are incurred. A discounted cash flow technique in which the time value of money is taken into account is then used to sum these costs (Park, 2016). In order to compare costs of seawater uranium production for various deployment strategies, the discounted cash flow technique is used to track the lifecycle of a unit mass of adsorbent from its initial fabrication through its reuses and final disposal. The overall procedure relies primarily on the Economic Modeling Working Group (EMWG) Of the Generation IV International Forum cost estimation guidelines as a reference (EMW, 2007).

The lifecycle discounted cash flow approach is given by

$$AF = \frac{\left(1 - \frac{1}{1+i_c}\right)^{t_{proj}}}{i_c} \tag{13.1}$$

where AF is the amortization factor, i_c is the interest rate on capital, and t_{proj} is the length of time over which the debt is financed. AF is used to derive a schedule on which capital expenses are made payable. In this technique, the point of initial deployment of the adsorbent is set to $t = 0$. This analysis also assumes that all costs are incurred when they are encountered in the lifecycle. Moreover, all unit masses of adsorbent are treated as having identical timelines, one of which is shown in figure 13.1.

Each cost component is normalized to common units, such as cost per ton of adsorbent produced or cost per ton of adsorbent deployed depending on the process step. The unit cost for each process is then found by summing all cost components for a given system process. For mooring and back end costs, the lifecycle unit cost of these processes is found by discounting the unit costs from the future at which each use occurs back to the present, and summed over all N. The only costs components that occur once in the lifecycle are the adsorbent production and disposal, and are therefore discounted to the past or the future, respectively. The total lifecycle cost of a unit of adsorbent, luc_{ads} is the sum of the total system steps. The final cost of uranium is then given by dividing luc_{ads} by the discounted uranium recovery rate per unit adsorbent, l_c (the details of this are described in Byers (2015)):

$$uc_u = \frac{luc_{ads}}{l_c}. \tag{13.2}$$

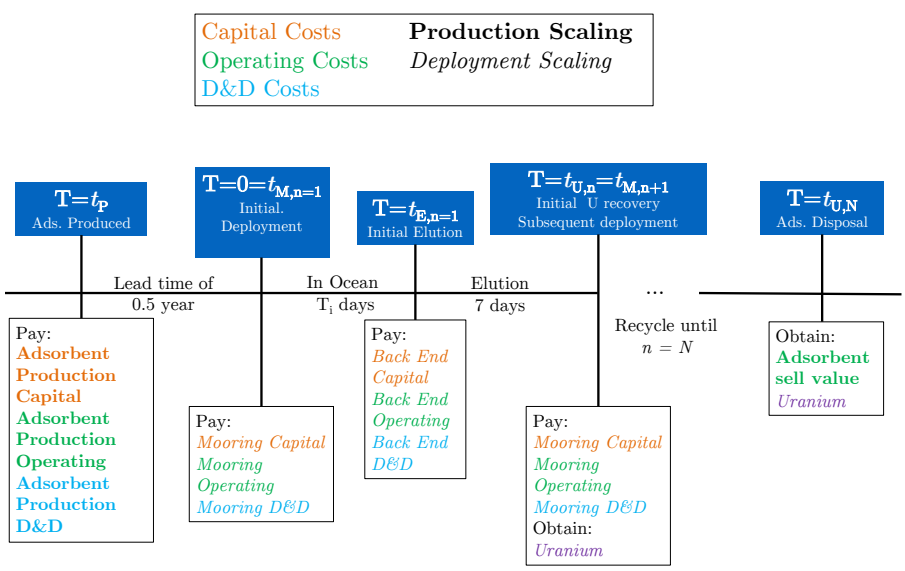

Figure 13.1: Timeline of the lifecycle of an adsorbent following the discounted cash flow technique.

13.2 Cost Components

The components of the production cost of uranium from seawater are broken down into the following categories:

1. Adsorbent Production
2. Mooring and Deployment
3. Elution and Regeneration (also known as Back End)

Relationships and reference data described below can be found in Byers (2015); Schneider and Sachde (2013) and Lindner and Schneider (2015).

13.2.1 Adsorbent Production Cost

The adsorbent production process involves three steps: fiber spinning, irradiation, and grafting. It can be broken down into capital costs, operating costs, and disposal and decommissioning costs.

Capital Costs

The main contributors to the capital cost of the adsorbent production are the cost of the buildings and equipment used for manufacturing the adsorbent backbone, grafting the ligand, fabricating the adsorbent into either a braid or a koosh ball, and conditioning the fibers before they are sent out to sea. Some of the costs are derived from scaling the costs of existing and theoretical chemical plants. Miscellaneous factors such as land, contractor's fees, and electrical systems are estimated to be a fraction of the equipment cost. These costs are considered to be amortized over the project lifetime and are a function of the amortization factor, AF from (13.1).

Operating Costs

In addition to capital cots, there will be costs associated with operating and maintaining the facility and equipment for the adsorbent production process. Specifically, the main cost components for the adsorbent operating costs are the labor, utilities, and material costs. All chemicals are assumed to be used with 100% efficiency of their nominal values. For the chemicals which are known to be reusable, only 90% is assumed to be recycled to account for some inevitable loss. Additionally, miscellaneous costs such as taxes, contingency, etc. scale with the production rate of the finished adsorbent. Incineration, considered to be the disposal method for select materials, and hazardous waste disposal are both included in the cost estimate.

Disposal and Decommissioning (D&D) Costs

When the project is complete, all facilities and equipment related to the adsorbent production must be decommissioned and/or disposed of. For this cost analysis, these disposal and decommissioning (D&D) costs are estimated to be 10% of the adsorbent production capital cost. The D&D costs are considered to be made payable on a yearly basis and the funds set aside for the D&D of facilities earn interest in a sinking fund throughout the lifetime of the project.

13.2.2 Mooring and Deployment Cost

Mooring equipment and marine transportation are required for the mooring, deployment, and retrieval of the adsorbents at the selected site. As with the adsorbent production, the costs associated with this aspect of seawater uranium production can be categorized into capital costs, operating costs, and disposal and decommissioning costs.

Capital Costs

In the case of the mooring and deployment, the capital cost is determined by the strategy used for the deployment of the adsorbent at sea. Unlike the adsorbent production, because this process occurs at sea there is no building cost. Rather, the major cost components include the cost of boats to install and retrieve the adsorbent and any equipment needed for operations of a specific deployment strategy. For instance, the capital cost components of the reference deployment strategy include mooring chains to keep the buoyant adsorbent braids weighted down to the seafloor. On the other hand, in the case of SMORE, the capital cost includes all additional equipment attached to the wind turbine to secure or cycle the adsorbent shell nets, such as the steel rollers.

Operating Costs

As with the adsorbent production, the mooring and deployment process includes costs for operation and maintenance of the deployment. As in the adsorbent production process, these chemicals are assumed to be used with 100% efficiency and 90% recyclability. Like the mooring and deployment capital costs, the operating costs will vary depending on the deployment strategy. For example, in the case of the reference deployment strategy operating costs include the cost of labor, ships, and fuel for frequent visits for retrieval and redeployment of the adsorbent between the field site and a mothership on which the elution process takes place. Additional cost components contributing to the operating and maintenance cost of the mooring and deployment process include the off-shore lease, which is a function of the area required for the adsorbent field.

Disposal and Decommissioning (D&D) Costs

All facilities and equipment related to the mooring and deployment must be decommissioned and/or disposed of at the end of the project's lifetime. As with the adsorbent production, these D&D costs are estimated to be 10% of the mooring and deployment capital cost that are made payable on a yearly basis and the funds set aside for the D&D of facilities earn interest in a sinking fund throughout the lifetime of the project.

13.2.3 Elution and Regeneration Cost

Finally, the elution and regeneration process also incurs capital, operating, and D&D costs. This process includes the elution of metals from the adsorbent, the purification of uranium to transform it to purified ammonium diuranate (ADU), and any reconditioning required to prepare the adsorbent for redeployment. The reconditioning of the adsorbent only occurs when the adsorbent will be redeployment and therefore is not considered to occur after the last adsorbent reuse. These costs are referred to as "back end" costs.

Capital Costs

The capital costs related to the back end include the costs of buildings and equipment needed to both elute the uranium off the braided adsorbent, to purify the products to ADU, and recondition the polymer for reuse. These costs include the expenses for building the facilities, stocking them with necessary equipment and initial inventory, and other expenses. One month's worth of initial chemical inventory is included in the capital cost. These costs will vary between deployment strategies as the reference deployment strategy considers the elution and regeneration steps to take place on a mothership close to the deployment site, while the SMORE strategy considers the elution and regeneration steps to take place at the deployment site. However, the purification step to ADU is still assumed to be preformed at a dedicated onshore facility for all deployment strategies.

Operating Costs

The operating and maintenance costs for the back end steps include costs due to chemicals, labor, and utilities required. These costs will largely be the same for each deployment strategy, with the exception of labor as the SMORE strategy runs these processes autonomously while the reference strategy requires operators to run the elution and regeneration processes. Additionally, the chemicals required for the back end will vary depending on the adsorbent used for the deployment.

Disposal and Decommissioning (D&D) Costs

The D&D costs associated for the back end are considered as they are for the adsorbent production process. That is, upon the project's completion, all facilities and

equipment related to the back end must be decommissioned and/or disposed of. The D%D costs are considered to be 10% of the back end capital cost and are made payable on a yearly basis with the funds set aside for the D&D of facilities earning interest in a sinking fund throughout the lifetime of the project. Selling the adsorbent for its backbone fiber as an alternative to the disposal of the adsorbent is also considered in this cost-analysis methodology. Specifically, the adsorbent could be recycled as a source of high-density polyethylene (HDPE), for which considerable knowledge into its recycle and reconstitution exists. Applications of the recovered HDPE include building and paving materials, or it may be directly recycled into the adsorbent fabrication process, thereby reducing the need to purchase virgin HDPE.

13.3 Parameter Space

This section describes the parameter space used in the cost analysis of the uranium from seawater production cost.

13.3.1 Length of campaign

As described in (10.1), the adsorbent uptake can be modeled as a one-side ligand saturation model and is a function of the immersion time, t, of the adsorbent in seawater. The immersion time is referred to as the length of campaign for the purposes of this cost analysis. Realistically, the campaign must be greater than 0 and should not exceed the time it takes to reach 95% of the saturation capacity of the adsorbent. This realistic limit is imposed because little gain will be realized by extending soaking times due to the asymptotic nature of (10.1).

13.3.2 Temperature

The uranium uptake of the adsorbent has been shown to be strongly affected by the seawater temperature. In general, a higher temperature leads to both higher saturation capacity and half-saturation time, and thereby a greater adsorbent uptake. At present, the cost-analysis tool allows users to input a temperature for the deployment's entire lifetime.

13.3.3 Degree of grafting

The amidoxime functional groups of the adsorbent are attached to the HDPE adsorbent backbone through a process known as irradiation induced-grafting. The degree of grafting (DOG) is a measure of this addition of the amidoxime group to the HDPE backbone and is defined by

$$DOG = \frac{W_G - W_O}{W_O} \times 100\%, \tag{13.3}$$

where W_G is the weight of the grafted polyethylene and W_O is the weight of the ungrafted polyethylene fibers. Although increasing the ratio of ligand to backbone improves the adsorbents uptake, it also increases the adsorbent production operating costs as it increases the grafting chemical consumption. Higher degrees of grafting lead to more available binding sites and a higher uranium capacity per mass of adsorbent, however experiments suggest that increasing the degree of grafting beyond 250% yields only marginal increase in the adsorbent's uranium uptake (Janke et al., 2014a). Thus, the feasible domain for capacity is bounded such that it cannot exceed 250%.

13.3.4 Number of reuses

The cost of uranium production from seawater is also affected by the number of times the adsorbent is used. With each subsequent reuse, the chemical baths involved in the elution process degrade the uranium binding sites on the adsorbent. Hence, with each reuse, the adsorbent suffers degradation which compounds with use. The end of the adsorbent's lifetime is taken to be the point at which the accumulated degradation becomes so high that the marginal benefits of redeployment are outweighed by the marginal costs.

13.3.5 Degradation

The degradation of the adsorbent polymer directly influences the number of uses that are economically feasible. Initial experimental data suggested that the adsorbent would consistently suffer 5% loss in uptake after each reuse (Sugo et al., 2001). However, more recent experimental data suggests that the adsorbent degradation rate

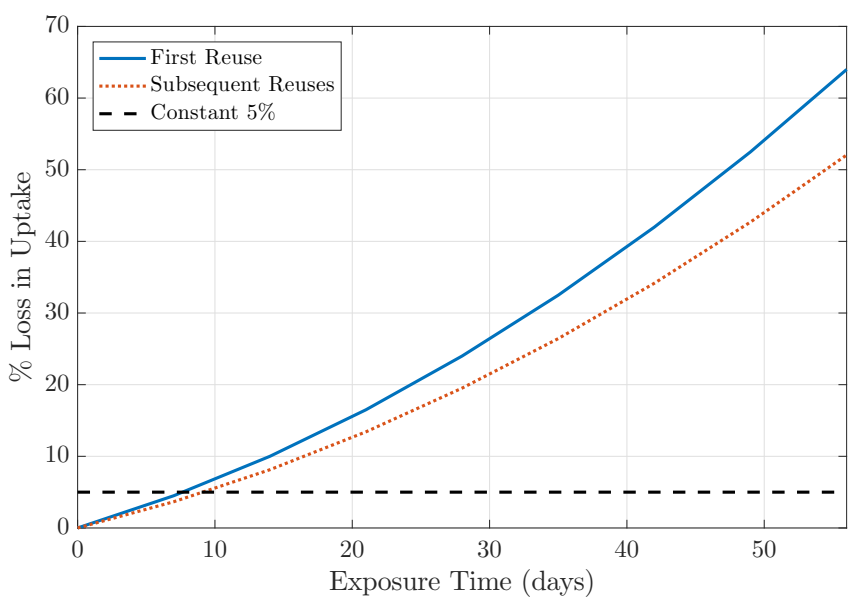

Figure 13.2: Loss in adsorbent uptake as a function of campaign length for the worst case degradation scenario, adapted from Byers and Schneider (2016b)

is a function of campaign length and number of reuses, with the first reuse suffering the greatest loss in uptake (Kuo et al., 2015), as shown in figure 13.2 (Byers and Schneider, 2016b). Work by Pan et al. (2017) suggests that a bicarbonate elution process may remove uranium from the adsorbent with observed degradation rates of below 1% per reuse. Thus, the time dependent model for degradation will serves as an upper bound on the adsorbent degradation while the constant 5% loss in uptake provides the lower bound.

13.3.6 Biofouling

Biofouling has a significant affect on the adsorbent's ability to uptake uranium, namely decreasing the saturation capacity of the adsorbent. In the experiment by Park et al. (2016), the adsorbent fibers exposed to unfiltered seawater and kept in the presence of light suffered 30% loss in uptake as compared to control fibers. Additionally, this loss was consistent for all measured time-points. Therefore, the cost analysis model described in this chapter assumes the effects of biofouling with time to be negligible and a constant 30% loss in uptake is considered independent of campaign length.

Moreover, because biofouling is dependent on the temperature of seawater, in the absence of experimental data, a placeholder relationship between the temperature and biofouling of the adsorbent was derived and is integrated into the cost analysis by Byers (2015) to offset the unrealistic monotonic relationship between increasing temperature and uptake. In particular, while the uranium complexation with amidoxime fiber favors warmer waters , it is likely that a competing feedback of increased biofouling also exists at these elevated temperatures. In general, the adsorbent in warmer waters will likely experience a greater amount of biofouling. White et al. (1991) present the following formula relating the heterotrophic bacterial specific growth rate, G (day^{-1}), and the ocean temperature, T (°C):

$$\log(G) = -1.54 + (0.052 \pm 0.05)T. \tag{13.4}$$

Equation (13.4) is used in this cost analysis correlate the effects of biofouling to water temperature. The temperature dependent biofouling is applied only to the adsorbent saturation capacity because experiments have shown that temperature affects the adsorbent capacity but not the kinetics (Park et al., 2016). The details of the implementation of this dependence into the cost analysis model are described in Byers (2015).

13.4 Reference Deployment Strategy

The reference deployment strategy refers to the kelp-field like structure described first by Tamada et al. (2006) and later modified for economic improvements by Schneider and Linder (2014). In this system, shown in figure 13.3, the adsorbent polymer is braided into buoyant 60 m long strands which are attached to metal chains that act to anchor the braids to the sea floor as well as hold rows of adsorbent braids together.

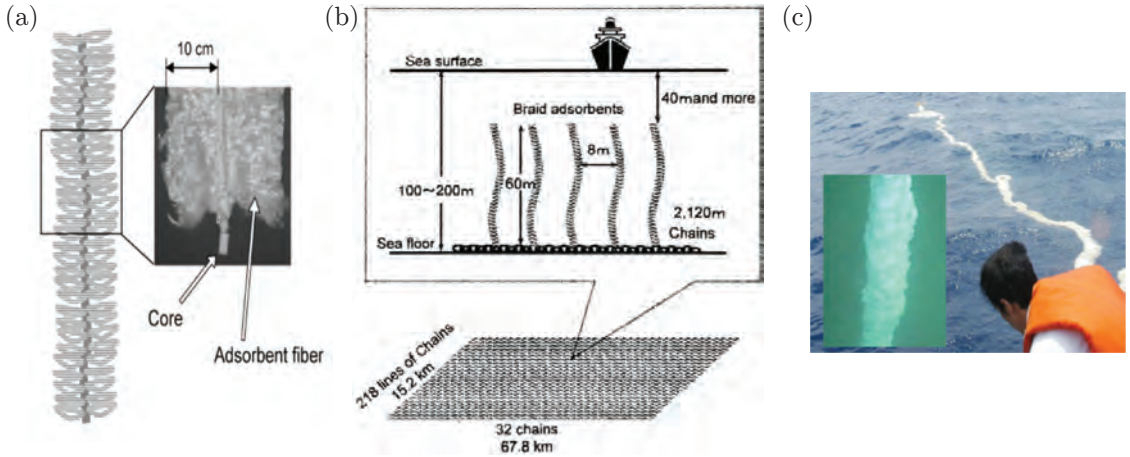

Figure 13.3: In the reference deployment strategy, the adsorbent is (a) braided into buoyant 60 m long lengths and (b) deployed across the seafloor. This strategy was (c) tested by the Japanese Atomic Energy Agency in the early 2000s (Tamada et al., 2006)

.

After sufficient seawater exposure at the end of a campaign, the adsorbent braids are winched up by work boats which then transfer the braids to a mothership that houses the chemical bath for the elution of uranium from the polymers. The adsorbents are then redeployed back to the field by the work boats. The adsorbents can be reused as many times as is economically feasible, dependent upon the degradation they suffer with each deployment and elution cycle. Although this off-shore elution system offers improvement over the original method, there are still non-trivial expenses associated with the capital and operating costs of this system. The cost of uranium recovered by this means will serve as the reference system to which SMORE will be compared.

13.5 SMORE Deployment Strategy

The design analysis tool described in chapter 10 is employed in the cost analysis of a continuous version of SMORE in which the adsorbent net is constantly moving through the water column using a set of upper and lower rollers. Table 13.1 describes the details of this system.

All support structures are considered to be made of 316 stainless steel. The capital cost of the SMORE structure was calculated primarily by the raw materials required to construct the device. Each harvester unit (i.e. each symbiotic wind turbine device) was sized to support and process the mass of adsorbent required to recover 1,200 tonnes of uranium per year (enough to supply a 5 GW nuclear reactor) from an entire wind farm consisting of 250 turbines.

The adsorbent production cost remained mostly unchanged from previous economic analyses with the kelp-filed deployment strategy. There was however a required cost to wind the adsorbent into koosh balls, fabricate the shells, and to construct the

Table 13.1: Details of continuous SMORE design used in cost analysis

Parameter	**Value**	**Notes**
System type	Stationary	
Current speed, V_{cs}	1 m/s	Reasonable for boundary currents
Bottom current speed, $V_{cs,b}$	0.01 m/s	
Depth to bottom current, D_{cb}	25 m	
Shell diameter, d_s	0.5 m	Input
Spacing between shells, L_s	0.1 m	Input
Shells per turbine, N_{st}	16340	Optimized by shell model
Ball-chains lengths per roller	10	Input
System depth, D_{sys}	120 m	Input
Platform height above SWL, H_p	10 m	Input
Rollers, N_{roller}	4	
Roller diameter, d_{roller}	2.3 m	
Roller inner diameter, $d_{roller,in}$	2.1 m	
Roller length, L_{roller}	6.6 m	
Spacing between rollers, $L_{sp,roller}$	1 m	
Platform length, L_{pt}	2.74 m	
Rail radius, r_{rail}	0.25 m	
Groove radius, r_{groove}	0.35 m	
Wheels per rail, N_{wheel}	7	Considering polyurethane wheels
Ball-chain rope diameter, d_r	0.016 m	
Ball-chain top tension, T_{top}	18620 N	
Ball-chain bottom tension, T_{bot}	17911 N	
Ball-chain max displacement, y_{max}	1.94 m	
Chemical agitation power, P_{ag}	12 kW	
Chemical heating power, P_{heat}	159.42 kW	
Chemical pumping power, P_{pump}	4.47 kW	
Roller motorizing power, P_{roller}	92 kW	
Total power required, P_{total}	546 kW	

overall adsorbent nets suitable for deployment with this system.

The method of calculating elution and purification costs also remains mostly unchanged from previous analyses. While the elution of uranium off the adsorbent takes place at sea on the turbine, the necessary purification process was still assumed to take place on land. Therefore, the labor and facility costs for adsorbent elution are reduced. For this cost comparison, a bicarbonate elution process was considered and all costs incurred after the bicarbonate elution are calculated in the exact same way as in previous economic estimates (Schneider and Sachde, 2013; Byers, 2015; Byers et al., 2016).

Table 13.2: Input data used for cost-analysis

Parameter	**Best Case Value**	**Worst Case Value**
Adsorbent	AF1	
Temperature (°C)	20	
Degree of Grafting (%)	250	
Alkaline Solution	NaOH	
Biofouling (% loss in uptake)	0	30
Degradation (% loss per re-use)	5	Worst Case

Table 13.3: Optimized deployment parameters leading to the minimum achievable uranium production cost.

	Reference			**SMORE**		
	Cost ($/kgU)	Uses	Campaign	Cost ($/kgU)	Uses	Campaign
Worst Case	$870	10	15 days	$593	20	10 days
Best Case	$430	13	45 days	$313	20	50 days

13.6 Results

The parameters described in section 13.3 give a range of possibilities for the adsorbent's performance in open ocean conditions and hence the uranium production cost. The rate of adsorbent degradation and the affect of marine biofouling are used to characterize the best and worst case scenarios. Both of these uncertainties lead to a range of uranium production costs and are believed to represent the best and worst case scenarios, for the current technology. All performance scenarios were subjected to an optimization algorithm (Schneider and Sachde, 2013) used to find the deployment parameters, specifically length of campaign and number of adsorbent uses, that give rise to the minimum possible recovery cost. The details of the input parameters used in this cost analysis are described in table 13.2. The campaign length and number of adsorbent uses are determined using an optimization procedure (Byers, 2015) to find the lowest possible uranium production cost for the given set of inputs. The results for the cost optimization of both strategies is summarized in Table 8.2.

Figure 13.4 shows the cost range for the best and worst case scenarios of both deployment strategies as a function of number of adsorbent uses. In both the best and worst case scenarios, the SMORE deployment strategy resulted in a lower recovery cost, in part due to a higher number of optimized uses, as seen by the shape of the curves in figure 13.4. Additionally, the symbiotic scheme can sustain a longer campaign length as seen in table 13.3 since the cost of each deployment event is lower. The lower deployment capital cost favors a large field with longer soaking times as opposed to a smaller field with a higher turnover rate. This is especially evident in the case of the constant degradation rate as no penalty is suffered from longer deployments.

A cost breakdown for both deployment strategies is provided in figure 13.5 for

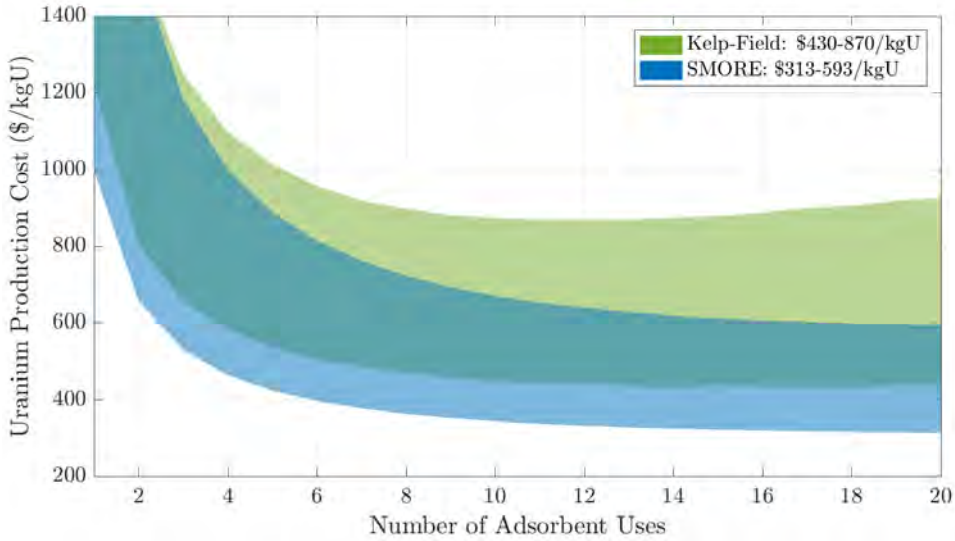

Figure 13.4: The range of costs for both deployment schemes as a function of number of adsorbent uses.

an intermediary case assuming no biofouling and the worst case, time-dependent degradation. After adsorbent production, the most significant cost contributor to the reference deployment strategy is the mooring and deployment cost; reducing this cost by means of the novel SMORE system presented here can thus have a substantial effect on the final uranium production cost. Given that for an intermediary deployment scenario the mooring and deployment comprise 37% of the production cost of uranium from seawater, SMORE could drastically reduce the estimated production cost. Additionally, significant reduction of the mooring and deployment cost which allows for a much greater number of optimized uses, further improving uranium costs.

In this intermediary case, the reference deployment resulted in a cost of $634/kg U with a 15 day campaign length and 11 adsorbent uses, while the SMORE strategy resulted in a cost of $443/kg U for a campaign length of 10 days and 20 uses. As can be seen from the figure, the majority of the cost differences between the two strategies are due to the mooring capital and operation costs of each system. Specifically, the SMORE strategy is able to reduce the mooring and deployment costs by over 43% so that they only contribute ∼30% to the overall uranium production cost.

Further examining some of the various components of the mooring capital and operating costs of both strategies, seen in figure 13.6, shows that the autonomous nature of the SMORE system results in significantly lower labor costs, which is responsible for the majority of the cost savings as compared to the reference deployment strategy. Specifically, the labor costs contribution to the mooring operating costs of the SMORE deployment are 87% less than those of the reference deployment strategy for this intermediary case.

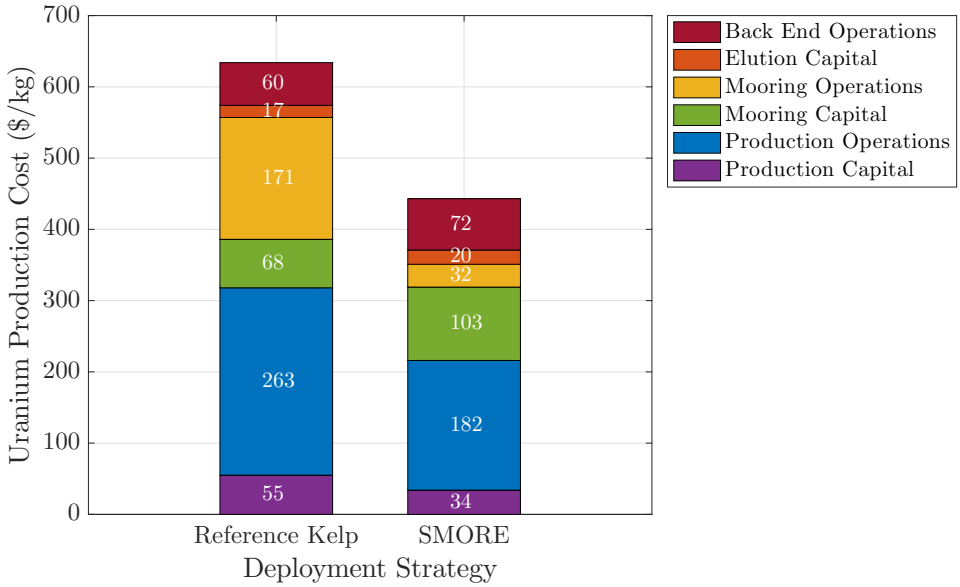

Figure 13.5: Breakdown of cost components contributing to the total cost of each deployment scheme for an intermediary case assuming no biofouling and worst case, time-dependent degradation.

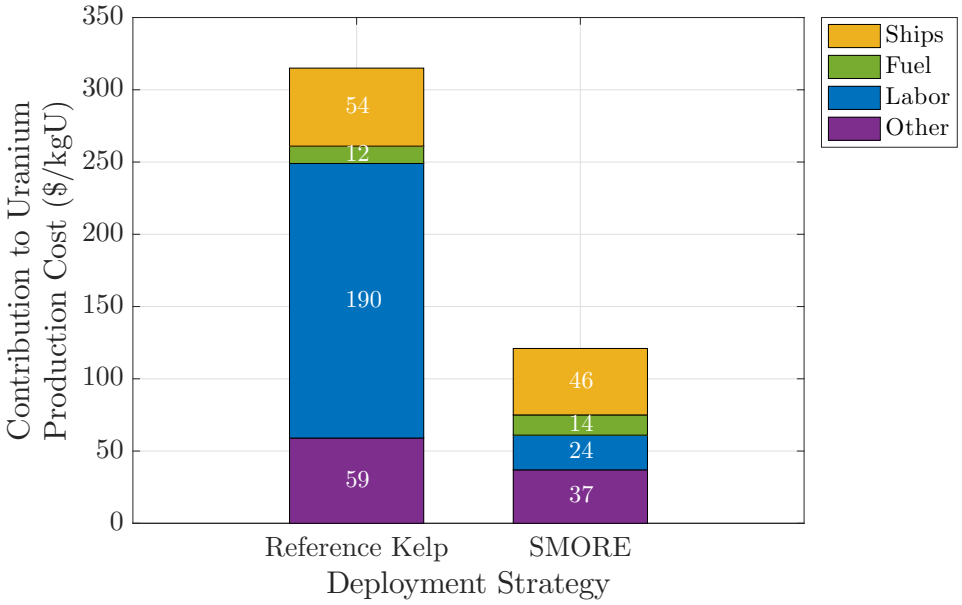

Figure 13.6: Some cost components contributing to the mooring capital and operating costs for each deployment strategy. The category labeled "Other" includes other operating consumables and contingencies.

13.7 Conclusion

This cost-analysis broke down the costs of recovering uranium from seawater into three major processes: (1) adsorbent production, (2) mooring and deployment, and (3)

elution and regeneration. As can be seen from this study, the mooring and deployment costs can be drastically reduced by coupling the recovery of uranium from seawater with offshore wind power generation. This is especially impactful if the best case scenario regarding adsorbent performance can be realized, meaning oceanic biofouling can be mitigated to realize negligible effects on uptake and adsorbent degradation rate can be restored to previously observed levels.

Specifically, the SMORE deployment strategy has the potential to decrease the uranium production cost by drastically decreasing the mooring and deployment costs. In the design studied here, for an intermediary case considering no biofouling and time dependent degradation, the SMORE strategy achieves an 87% reduction in the labor costs associated with the deployment, directly translating to a 43% reduction in the mooring and deployment costs and an overall cost reduction of 30% in the production cost of uranium from seawater.

Of the major processes, the next largest cost driver that remains is the adsorbent production cost. In SMORE strategy, this process now accounts for over 48% of the uranium production cost. These costs can be reduced by either increasing the adsorbent capacity (and therefore reducing the amount of adsorbent required for a deployment), reducing the affect of biofouling on the adsorbent (and thereby increasing the time the adsorbent can be used for), decreasing the degradation of the adsorbent after each elution cycle (thus allowing for increased reuse of the adsorbent), or reducing the overall cost of adsorbent production. As shown figure 13.7, which examines the cost components related to the adsorbent production for this intermediary case, the major cost drivers of the adsorbent production include the material costs (namely hydroxylamine HCl which is required for the irradiation-induced grafting process of the amidoxime ligand onto the radical sites on the polyethylene backbone), electricity costs, and maintenance.

Although this cost analysis accounted for the effect of biofouling reducing the uptake of uranium by the adsorbent, it does not consider how this biofouling will affect other steps in the uranium extraction process. For instance, growth on the adsorbents may increase the amount of chemicals required for the elution and regeneration processes per tonne of adsorbent, thereby increasing the cost. Additionally, because the chemical processing will be done autonomously at sea, there may also be other marine debris that entire the chemical tanks during elution and regeneration which may increase the amount of chemicals needed for these processes even more. A future cost analysis of a symbiotic system to harvest uranium from seawater should account for these additional chemical requirements.

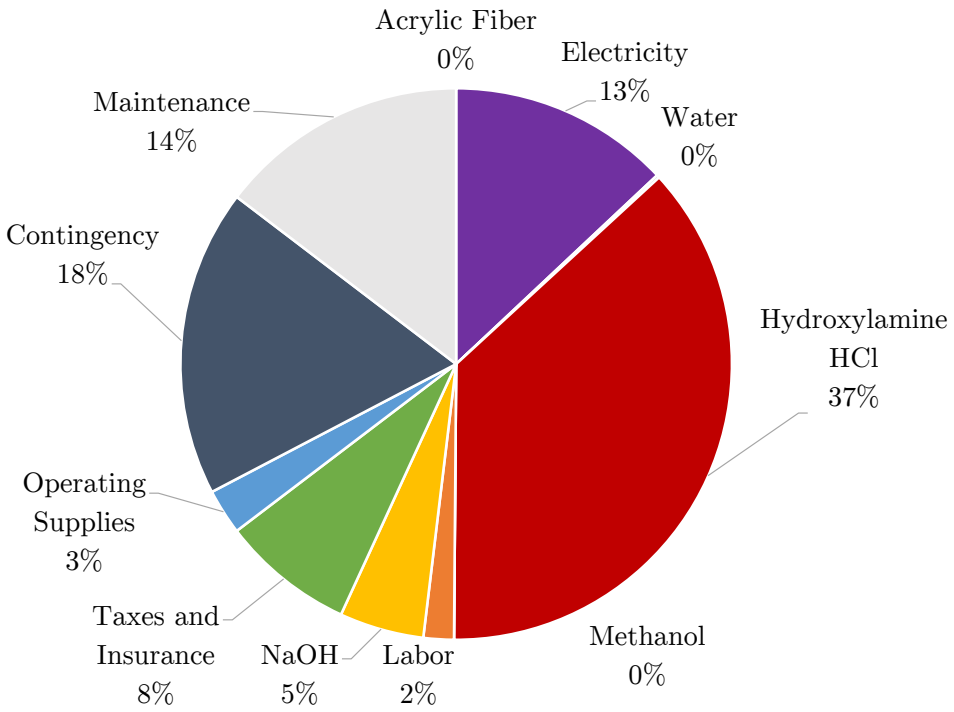

Figure 13.7: Breakdown of adsorbent production costs.

Acknowledgements

This work was supported by the U.S. Department of Energy Office of Nuclear Energy under Contracts No. DE-NE0008268, DE-NE000731, and DE-NE0000745 and by the National Academies Keck Futures Initiative. This work was also supported in part by the MIT Energy Initiative, the Naval Engineering Education Center for support under Grant No. 3002883706. The salinity data from the Xylem EXO-2 Sonde was provided courtesy of the Buzzards Bay Coalition monitoring that is funded by a grant from the EPA.

This material is based upon work supported by the National Science Foundation Graduate Research Fellowship under Grant No. 1122374. Any opinion, findings, and conclusions or recommendations expressed in this material are those of the authors and do not necessarily reflect the views of the National Science Foundation. Thanks to Oak Ridge National Laboratory for the preparation of the adsorbent fibers for use in this study and to G. Gill and other researchers at the Pacific Northwest National Laboratory for the analysis of the fibers post-deployment.

Thank you to the staff and students of Massachusetts Maritime Academy for all their help and assistance during the ocean test of the 1/10th scaled prototype. Specifically, Tom Pham, Prof. Bill Hubbard, Bill Klimm, Thomas McEntee, Thanh Nguyen, Judson Poole, James Wall, Matthew Simms, and Jimmy Benedetto, John Edwards and Walter Yohai played an integral role in ensuring the success of this study.

Special thanks to the undergraduate researchers who have contributed to making this project a success thus far: Chukwunenye Anagbogu, Phoophie Chavez, Cyndia Cao, Justin Carrus, Cedric Delmy, Patrick Everett, Jorge Gonzalez, Jessie Hsiao, Jasmine Lennert, Bo Paulson, Costa Rivas, and Charles Vitry.

Bibliography

Cost estimating guidelines for Generation IV nuclear energy systems, Revision 4.2. The Economic Modeling Working Group Of the Generation IV International Forum, Generation IV International Forum, 2007.

T. S. Anirudhan, A. R. Tharun, S. Rijith, and P. S. Suchithra. Synthesis and characterization of a novel graft copolymer containing carboxyl groups and its application to extract uranium (VI) from aqueous media. *Journal of Applied Polymer Science*, 122(2):874–884, 2011.

M. Byers. Optimization of the passive recovery of uranium from seawater. Master's thesis, The University of Texas at Austin, 2015.

M. F. Byers and E. Schneider. Uranium from Seawater Cost Analysis: Recent Updates. 2015.

M. F. Byers and E. Schneider. Optimization of the Passive Recovery of Uranium from Seawater. *Industrial & Engineering Chemistry Research*, 55(15):43514361, 2016a.

M. F. Byers and E. Schneider. Uranium from Seawater Cost Analysis: Recent Updates. 2016b.

M. F. Byers, M. N. Haji, A. H. Slocum, and E. Schneider. A Higher Fidelity Cost Analysis of Wind and Uranium from Seawater Acquisition symBiotic Infrastructure. 2016.

S. K. Chakrabarti. *Offshore Structure Modeling*. World Scientific, Singapore, SGP, 1994.

J. H. Conway and N. J. A. Sloane. *Sphere Packings, Lattices, and Groups*. Springer-Verlag, New York, 1993.

R. V. Davies, J. Kennedy, R. W. McIroy, R. Spence, and K. M. Hill. Extraction of Uranium From Sea Water. *Nature*, 203(495):1110–1115, 1964.

D. L. Elliot, C. G. Holladay, W. R. Barchet, H. P. Foote, and W. F. Sandusky. *Wind Energy Resource Atlas of the United States*. Solar Energy Research Institute, Golden, Colorado, 1987.

J. Emsley. *Nature's Building Blocks: An A to Z Guide to the Elements*. Oxford Univ. Press, 2001.

Energy Information Administration. International Energy Outlook 2013. Technical report, U.S. Department of Energy, July 2013.

P. Gerland, A. E. Raftery, H. Ševčková, N. Li, D. Gu, T. Spoorenberg, L. Alkema, B. K. Fosdick, J. Chunn, N. Lalic, G. Bay, T. Buettner, G. K. Heilig, and J. Wilmoth. World population stabilization unlikely this century. *Science*, 2014.

G. A. Gill, L.-J. Kuo, J. R. Wood, and C. Janke. Complete Laboratory Evaluation and Issue a Report on the Impact of Temperature on Uranium Adsorption. *Department of Energy Milestone report*, (September), 2014.

G. A. Gill, L.-J. Kuo, J. Strivens, J. Wood, N. J. Schlafer, C. Tsouris, A. Ladshaw, and S. Yiacoumi. Investigations into the Effect of Current Velocity on Amidoxime-Based Polymeric Uranium Adsorbent Performance. *Department of Energy Milestone report*, (December), 2015.

G. A. Gill, L.-J. Kuo, C. J. Janke, J. Park, R. T. Jeters, G. T. Bonheyo, H-B Pan, C. Wai, T. Khangaonkar, L. Bianucci, J. R. Wood, M. G. Warner, S. Peterson, D. G. Abrecht, R. T. Mayes, C. C. Tsouris, Y. Oyola, J. E. Strivens, N. J. Schlafer, R. S. Addleman, W. Chouyyok, S. Das, J. Kim, K. Buesseler, C. Breier, and E. D'Alessandro. The Uranium from Seawater Program at the Pacific Northwest National Laboratory: Overview of Marine Testing, Adsorbent Characterization, Adsorbent Durability, Adsorbent Toxicity, and Deployment Studies. *Industrial & Engineering Chemistry Research*, (15), 2016.

H and H Tooling. Basic Tube Bending Guide.

M. N. Haji, C. Vitry, and A. H. Slocum. Decoupling the functional requirements of an adsorbent for harvesting uranium from seawater through the use of shell enclosure. *Proceedings of the 2015 American Nuclear Society Winter Meeting and Nuclear Technology Expo*, 2015.

M. N. Haji, C. Delmy, J. Gonzalez, and A. H. Slocum. Uranium extraction from seawater using adsorbent shell enclosures via a symbiotic offshore wind turbine device. *Proceedings of tje 26th International Ocean and Polar Engineering Conference*, 2016.

M. N. Haji, M. Byers, E. Schneider, and A. H. Slocum. Cost Analysis of Wind and Uranium from Seawater Acquisition symBiotic Infrastructure using Shell Enclosures. *Proceedings of the 2015 American Nuclear Society Winter Meeting and Nuclear Technology Expo*, 2017.

A. M Hamlet. Uranium extraction from seawater: Investigating the hydrodynamic behavior and performance of porous shells. Master's thesis, Massachusetts Institute of Technology, 2017.

J. Hu, H. Ma, Z. Xing, X. Liu, L. Xu, R. Li, C. Ling, M. Wang, J. Li, and G. Wu. Preparation of Amidoximated UHMWPE Fiber by Radiation Grafting and Uranium Adsorption Test. *Industrial & Engineering Chemistry Research*, (15), 2016.

Intergovernmental Panel on Climate Change. Climate Change 2007: Synthesis Report. Contribution of Working Groups I, II and III to the Fourth Assessment. *World Meteorological Organization and the United Nations Environment Programme*, 2007.

C. Janke, S. Das, and R. Mayes. Preparation of most promising braided and/or textile-based adsorbents for seawater testing. Technical report, U.S. Department of Energy, February 2014a.

C. Janke, Y. Oyola, S. Das, R. Mayes, G. Gill, L. Kuo, and J. Wood. Complete braided adsorbent for marine testing to demonstrate 3g-U/kg-adsorbent. Technical report, Oak Ridge National Laboratory, 2014b.

J. Jonkman. Definition of the Floating System for Phase IV of OC3. Technical report, U.S. Department of Energy, May 2010.

J. M. Jonkman, S. Butterfield, W. Musial, and G. Scott. Definition of a 5-MW reference wind turbine for offshore system development. Technical report, U.S. Department of Energy, February 2009.

M. Kanno. Present status of study on extraction of uranium from sea water. *Journal of Nuclear Science and Technology*, 21(1):1–9, 1984.

J. Kim, C. Tsouris, R. T. Mayes, Y. Oyola, T. Saito, C. J. Janke, S. Dai, E. Schneider, and D. Sachde. Recovery of Uranium from Seawater: A Review of Current Status and Future Research Needs. *Separation Science and Technology*, 48:367–387, 2013.

J. Kluger. *Synergistic Design of a Combined Floating Wind Turbine - Wave Energy Converter*. PhD thesis, Massachusetts Institute of Technology, 2017.

L.-J. Kuo, G. Gill, H.-B. Pan, and C. Wai. Improving Adsorbent Reusability for Extraction of Uranium from Seawater. 2015.

A. Ladshaw, L.-J. Kuo, J. Strivens, J. Wood, N. Schlafer, S. Yiacoumi, C. Tsouris, and G. Gill. Influence of Current Velocity on Uranium Adsorption from Seawater Using an Amidoxime-Based Polymer Fiber Adsorbent. *Industrial & Engineering Chemistry Research*, 56:2205–2211, 2017.

A. Lakretz, E. Z. Ron, and H. Mamane. Biofouling control in water by various uvc wavelengths and doses. *Biofouling*, 26:257–267, 2010.

C. H. Lee and J. N. Newman. *WAMIT© User Manual*. WAMIT, Inc., Chestnut Hill, MA, 2006.

H. Lindner and E. Schneider. Review of cost estimates for uranium recovery from seawater. *Energy Economics*, 49:9–22, 2015.

W. S. Moore. Sampling ^{228}Ra in the deep ocean. *Deep Sea Research and Oceanographic Abstracts*, 23:647–651, 1976.

W. S. Moore. Radium isotope measurements using germanium detectors. *Nuclear Instruments and Methods in Physics Research*, 223:407–411, 1984.

W. S. Moore, H. Astwood, and C. Lindstrom. Radium isotopes in coastal waters on the Amazon shelf. *Geochimica et Cosmochimica Acta*, 59:4285–4298, 1995.

A. Myhr, C. Bjerkseter, A. Ågotnes, and T. A. Nygaard. Levelised cost of energy for offshore floating wind turbines in a life cycle perspective. *Renewable Energy*, 66: 714–728, 2014.

J. Newman and P. Sclavounos. The computation of wave loads on large offshore structures. In *Proceedings of BOSS*, 1988.

C. Not, K. Brown, B. Ghaleb, and C. Hillaire-Marcel. Conservative behavior of uranium vs. salinity in Arctic sea ice and brine. *Mar. Chem.*, 130–131:33–39, 2012.

OECD Nuclear Energy Agency. Managing Environmental and Health Impacts of Uranium Mining. Technical report, OECD Nuclear Energy Agency and the International Atomic Energy Agency, 2014.

K. Oguma, T. Suzuki, and K. Saito. Determination of uranium in seawater by flow-injection preconcentration on dodecylamidoxime-impregnated resin and spectrophotometric detection. *Talanta*, 84(5):1209–1214, 2011.

S. A. Owens, K. O. Buesseler, and K. W. W. Sims. Re-evaluating the ^{238}U-salinity relationship in seawater: Implications for the ^{238}U-Th- 234 disequilibrium method. *Marine Chemistry*, 127(1–4):31–39, 2011.

H.-B. Pan, W. Liao, C. M. Wai, Oyola Y., C. J. Janke, G. Tian, and Rao L. Carbonate-H_2O_2 leaching for sequestering uranium from seawater. *Dalton transactions*, 43(28):10713–8, 2014.

H.-B. Pan, C. M. Wai, L.-J. Kuo, G. Gill, G. Tian, L. Rao, S. Das, R. T. Mayes, and C. J. Janke. Bicarbonate Elution of Uranium from Amidoxime-Based Polymer Adsorbents for Sequestering Uranium from Seawater. *Chemistry Select*, 2(13): 3769–3774, 2017.

C. Park. Contemporary Engineering Economics. pages 220–227, 2016.

J. Park, G. A. Gill, J. E. Strivens, L.-J. Kuo, R. Jeters, A. Avila, J. Wood, N. J. Schlafer, C. J. Janke, E. A. Miller, M. Thomas, R. S. Addleman, and G. Bonheyo. Effect Of Biofouling On The Performance Of Amidoxime-Based Polymeric Uranium Adsorbents. *Industrial & Engineering Chemistry Research*, (15), 2016.

PelaFlow Consulting. Wind turbine power output variation with steady wind speed, 2008. `http://www.wind-power-program.com/turbine_characteristics.htm`, Accessed: 2014-10-12.

M. Picard, C. Baelden, Y. Wu, L. Chang, and A. H. Slocum. Extraction of Uranium from Seawater: Design and Testing of a Symbiotic System. *Nuclear Technology*, 188(2), 2014.

A. I. Railkin. *Marine Biofouling: Colonization Processes and Defenses*. CRC Press, 2003.

R. W. Reynolds, N. A. Rayner, T. M. Smith, D. C. Stokes, and W. Wang. An improved in situ and satellite SST analysis for climate. *Journal of Climate*, 15: 1609–1625, 2002.

D. J. Sachde. Uranium Extraction from Seawater: An Assessment of Cost, Uncertainty and Policy Implications. Master's thesis, The University of Texas at Austin, 2011.

T. Saito, S. Brown, S. Chatterjee, J. Kim, C. Tsouris, R. Mayes, L.-J. Kuo, Y. Gill, G. Oyola, C. Janke, and S. Dai. Uranium recovery from seawater: development of fiber adsorbents prepared via atom-transfer radical polymerization. *Journal of Materials Chemistry A*, 2:14674–14681, 2014.

E. Schneider and H. Linder. Updates to the Estimated Cost of Uranium Recovery from Seawater. In *Proceedings of the 19th Pacific Basin Nuclear Conference*, 2014.

E. Schneider and D. Sachde. The Cost of Recovering Uranium from Seawater by a Braided Polymer Adsorbent System. *Sci. Glob. Sec.*, 21(2):134–163, 2013.

M. Schwartz, D. Heimiller, S. Haymes, and W. Musial. Assessment of Offshore Wind Energy Resources for the United States Assessment of Offshore Wind Energy Resources for the United States. Technical report, National Renewable Energy Laboratory, 2010.

K. Sekiguchi, K. Saito, S. Konishi, S. Furusaki, T. Sugo, and H. Nobukawa. Effect of seawater temperature on uranium recovery from seawater using amidoxime adsorbents. *Industrial & Engineering Chemistry Research*, 33(3):662–666, 1994.

N. Seko, A. Katakai, S. Hasegawa, M. Tamada, N. Kasai, H. Takeda, T. Sugo, and K. Saito. Aquaculture of uranium in seawater by a fabric-adsorbent submerged system. *Nuclear Technology*, 144(2):274–278, 2003.

N. Seko, A. Katakai, M. Tamada, and S. Takanobu. Fine Fibrous Amidoxime Adsorbent Synthesized by Grafting and Uranium AdsorptionElution Cyclic Test with Seawater. *Separation Science and Technology*, 39(16):3753–3767, 2004.

Alexander H. Slocum. *FUNdaMENTALS of Design*. 2008.

C. P. Sparks. *Fundamentals of Marine Riser Mechanics - Basic Principles and Simplified Analysis*. PennWell, 2007.

T. Sugo, M. Tamada, T. Seguchi, T. Shimizu, M. Uotani, and R. Kashima. Recovery System for Uranium from Seawater with Fibrous Adsorbent and Its Preliminary Cost Estimation. *Journal of the Atomic Energy Society of Japan*, 43(10):1010–1016, 2001.

M. Tamada. Current status of technology for collection of uranium from seawater. *Japan Atomic Energy Agency*, 2009.

M. Tamada, N. Seko, N. Kasai, , and T. Shimizu. Cost estimation of uranium recovery from seawater with system of braid type adsorbent. *Transactions of the Atomic Energy Society of Japan*, 5(4):358–363, 2006.

G. A. Tularam and M. Ilahee. Environmental concerns of desalinating seawater using reverse osmosis. *Journal of Environmental Monitoring*, 9(8):805–813, 2007.

Union of Concerned Scientists. Fact Sheet - Nuclear Power and Water: Quick Facts on Nuclear Power Generation and Water Use. Technical report, 2011. URL `http://www.ucsusa.org/sites/default/files/legacy/assets/documents/nuclear_power/fact-sheet-water-use.pdf`.

University of Idaho. Uranium Recovery from Seawater: A Nation-Wide Consortium for Sustainable Energy - University of Idaho. `http://uraniumfromseawater.engr.utexas.edu/partners/university-idaho`, Accessed: 2017-04-15.

R. van Reis and A. Zydney. Bioprocess membrane technology. *Journal of Membrane Science*, 297(1):16–50, 2007.

P. A. White, J. Kalff, J. B. Rasmussen, and J. M. Gasol. The effect of temperature and algal biomass on bacterial production and specific growth rate in freshwater and marine habitats. *Microbial Ecologycology*, 21:99–118, 1991.

Z. Xing, J. Hu, M. Wang, W. Zhang, S. Li, Q. Gao, and G. Wu. Properties and evaluation of amidoxime-based UHMWPE fibrous adsorbent for extraction of uranium from seawater. *Science China Chemistry*, 56(11):1504–1509, 2013.

A. Yamanaka, Y. Izumi, T. Kitagawa, T. Terada, H. Hirahata, K. Ema, H. Fujishiro, and S. Nishijima. The effect of gamma-irradiation on thermal strain of high strength polyethylene fiber at low temperature. *Journal of Applied Polymer Science*, 102: 204–209, 2006.

A. Zhang, T. Asakura, and G. Uchiyama. The adsorption mechanism of uranium (VI) from seawater on a macroporous fibrous polymeric adsorbent containing amidoxime chelating functional group. *Reactive and Functional Polymers*, 57(1):6776, 2003.

Y. N. Zhao, M. H. Wang, Z. F. Tang, and G. Z. Wu. Effect of gamma-ray irradiation on the structure and mechanical properties of UHMWPE fibers. *Polymer Materials Science & Engineering*, 26:32–35, 2010.